Advances in Polymer Science 252

Toshiji Kanaya *Editor*

# Glass Transition, Dynamics and Heterogeneity of Polymer Thin Films

Springer

# 252
# Advances in Polymer Science

For further volumes:
http://www.springer.com/series/12

## Aims and Scope

The series *Advances in Polymer Science* presents critical reviews of the present and future trends in polymer and biopolymer science. It covers all areas of research in polymer and biopolymer science including chemistry, physical chemistry, physics, material science.

The thematic volumes are addressed to scientists, whether at universities or in industry, who wish to keep abreast of the important advances in the covered topics.

*Advances in Polymer Science* enjoys a longstanding tradition and good reputation in its community. Each volume is dedicated to a current topic, and each review critically surveys one aspect of that topic, to place it within the context of the volume. The volumes typically summarize the significant developments of the last 5 to 10 years and discuss them critically, presenting selected examples, explaining and illustrating the important principles, and bringing together many important references of primary literature. On that basis, future research directions in the area can be discussed.

*Advances in Polymer Science* volumes thus are important references for polymer scientists, or scientists interested in polymer science - as an introduction to a neighboring field, or as a compilation of detailed information for the specialist.

Review articles for the individual volumes are invited by the volume editors. Single contributions can be specially commissioned.

Impact Factor in 2011: 3.890; Section “Polymer Science”: Rank 9 of 78

Toshiji Kanaya
Editor

# Glass Transition, Dynamics and Heterogeneity of Polymer Thin Films

With contributions by

Y. Fujii · K. Fukao · R. Inoue · T. Kanaya · H. Morita ·
K. Nakamura · G. Reiter · D. Tahara · A. Takahara ·
K. Tanaka · T. Terasawa

Springer

*Editor*
Toshiji Kanaya
Institute for Chemical Research
Kyoto University
Uji, Kyoto-fu 611-0011
Japan

ISSN 0065-3195 ISSN 1436-5030 (electronic)
ISBN 978-3-642-34338-4 ISBN 978-3-642-34339-1 (eBook)
DOI 10.1007/978-3-642-34339-1
Springer Heidelberg New York Dordrecht London

Library Control Congress Number: 2012950323

© Springer-Verlag Berlin Heidelberg 2013
This work is subject to copyright. All rights are reserved by the Publisher, whether the whole or part of the material is concerned, specifically the rights of translation, reprinting, reuse of illustrations, recitation, broadcasting, reproduction on microfilms or in any other physical way, and transmission or information storage and retrieval, electronic adaptation, computer software, or by similar or dissimilar methodology now known or hereafter developed. Exempted from this legal reservation are brief excerpts in connection with reviews or scholarly analysis or material supplied specifically for the purpose of being entered and executed on a computer system, for exclusive use by the purchaser of the work. Duplication of this publication or parts thereof is permitted only under the provisions of the Copyright Law of the Publisher's location, in its current version, and permission for use must always be obtained from Springer. Permissions for use may be obtained through RightsLink at the Copyright Clearance Center. Violations are liable to prosecution under the respective Copyright Law.
The use of general descriptive names, registered names, trademarks, service marks, etc. in this publication does not imply, even in the absence of a specific statement, that such names are exempt from the relevant protective laws and regulations and therefore free for general use.
While the advice and information in this book are believed to be true and accurate at the date of publication, neither the authors nor the editors nor the publisher can accept any legal responsibility for any errors or omissions that may be made. The publisher makes no warranty, express or implied, with respect to the material contained herein.

Printed on acid-free paper

Springer is part of Springer Science+Business Media (www.springer.com)

# Preface

State-of-the-art nanotechnology aims at producing functional nano-sized devices which require stable, homogeneous, and uniform polymer films in the nanometer scale. This need has been driving extensive studies of polymer thin films for more than a decade. Such films possess interesting but unusual properties such as anomalous film thickness dependence of the glass transition temperature Tg and thermal expansivity; they also display very large annealing effects and ultraslow relaxation in the molten and glass states. Unusual film thickness dependence of the glass transition temperature Tg has often been discussed in terms of quasi-multilayer structures consisting of, at least, a surface mobile layer, a middle bulk-like layer, and a bottom interface layer on a substrate, showing quasi-multilayer structures or the heterogeneous structure of polymer thin films.

In this special volume we focus our attention on recent studies of the glass transition, dynamics, and heterogeneity in polymer thin films using various experimental techniques to shed light on the present status of the research as well as future issues to be investigated. The volume includes studies on surface and interface glass transition temperatures of polymer thin films on solid substrates investigated by scanning force microscopy and fluorescence lifetime measurements, respectively, revealing the distribution of glass transition temperatures in the depth direction. Neutron scattering experiments on polymer thin films are also included in the volume, revealing the heterogeneous dynamics and the distribution of glass transition temperatures. Another topic is the effect of the preparation of polymer thin films on their properties. Residual stresses, arising from out-of-equilibrium chain conformations due to rapid solvent loss during the thin film preparation, was studied by visco-elastic dewetting of thin films. Aging dynamics of single and stacked thin polymer films is also investigated by differential scanning calorimetry and dielectric relaxation spectroscopy, showing the heterogeneous dynamics of polymer thin films.

The most important message in the volume is that the heterogeneity in polymer thin films is a key to understand their atypical properties although we still have many unsolved problems. In any case we hope that this special volume contributes to the development of polymer thin films in physics in future.

Finally, we are indebted to all people contributing to this special volume. Special thanks to Professor Akihiro Abe who gave me an opportunity to edit the volume and Ms Karin Bartsch and Dr Tobias Wassermann for continuous assistance to edit the volume.

Kyoto Toshiji Kanaya
August 2012

# Contents

**Mobility Gradient of Polystyrene in Films Supported on Solid Substrates** ........ 1
Yoshihisa Fujii, Hiroshi Morita, Atsushi Takahara, and Keiji Tanaka

**Probing Properties of Polymers in Thin Films Via Dewetting** ........ 29
Günter Reiter

**Heterogeneous and Aging Dynamics in Single and Stacked Thin Polymer Films** ........ 65
Koji Fukao, Takehide Terasawa, Kenji Nakamura, and Daisuke Tahara

**Heterogeneous Dynamics of Polymer Thin Films as Studied by Neutron Scattering** ........ 107
Rintaro Inoue and Toshiji Kanaya

**Index** ........ 141

Adv Polym Sci (2013) 252: 1–28
DOI: 10.1007/12_2012_175

# Mobility Gradient of Polystyrene in Films Supported on Solid Substrates

**Yoshihisa Fujii, Hiroshi Morita, Atsushi Takahara, and Keiji Tanaka**

**Abstract** In this review, we show the distribution of glass transition temperature ($T_g$) in monodisperse polystyrene (PS) films coated on silicon oxide layers along the direction normal to the surface. Scanning force microscopy with a lateral force mode revealed that surface $T_g$ ($T_g^s$) was lower than the corresponding bulk $T_g$ ($T_g^b$). Interestingly, the glass transition dynamics at the surface was better expressed by an Arrhenius equation than by a Vogel–Fulcher–Tamman equation. Interdiffusion experiments for PS bilayers at various temperatures, above $T_g^s$ and below $T_g^b$, enabled us to gain direct access to the mobility gradient in the surface region. $T_g$ at the solid substrate was examined by fluorescence lifetime measurements using evanescent wave excitation. The interfacial $T_g$ was higher than the corresponding $T_g^b$. The extent of the elevation was a function of the distance from the substrate and the interfacial energy. The $T_g$ both at the surface and interface was also studied by the coarse-grained molecular dynamics simulation. The results were in good accordance with the experimental results. Finally, dynamic mechanical analysis for PS in thin and ultrathin films was made. The relaxation time for the segmental motion became broader towards the faster and slower sides, due probably to the surface and interfacial mobility.

---

Y. Fujii
Department of Applied Chemistry, Kyushu University, Fukuoka 819-0395, Japan

H. Morita
Soft Matter Modeling Group, Nanosystem Research Institute, National Institute of Advanced Industrial Science and Technology, Ibaraki 305-8568, Japan

A. Takahara
Institute for Materials Chemistry and Engineering, Kyushu University, Fukuoka 819-0395, Japan

K. Tanaka (✉)
Department of Applied Chemistry, Kyushu University, Fukuoka 819-0395, Japan

International Institute for Carbon-neutral Energy Research (WPI-I2CNER), Kyushu University, Fukuoka 819-0395, Japan
e-mail: k-tanaka@cstf.kyushu-u.ac.jp

**Keywords** Coarse-grained molecular dynamics simulation • Interface • Scanning force microscopy • Surface • Thermal molecular motion • Time- and space-resolved fluorescence spectroscopy

## Contents

1 Introduction ........ 2
2 Surface ........ 4
  2.1 Two-Dimensional Modulus Mapping ........ 4
  2.2 Glass Transition ........ 5
  2.3 Mobility Gradient ........ 9
  2.4 Molecular Dynamics Simulation ........ 11
3 Substrate Interface ........ 15
  3.1 Glass Transition ........ 15
  3.2 Mobility Gradient ........ 17
  3.3 Molecular Dynamics Simulation ........ 19
4 Thin Films ........ 21
  4.1 Supported Film ........ 21
  4.2 Sandwiched Film ........ 23
5 Conclusion ........ 25
References ........ 26

## 1 Introduction

In the twenty-first century, materials have been strongly desired to be smaller and/or thinner for the construction of tiny devices. Such a trend is also the case for polymeric devices. Also, to design and construct highly functionalized memory devices, electron beam lithography has been applied to polymer materials. In this case, the linewidth is tremendously small, such as several tens of nanometer. Even in the traditional applications of coating, adhesion, lubrication, etc., polymer thin films are now being used [1]. In reality, it is not technically difficult to prepare such tiny polymeric pieces thanks to the advent of modern nanotechnology. However, once the polymer pieces become smaller than approximately 100 nm, their physical properties are altered from the corresponding bulk behaviors mainly due to "surface and interfacial effects" [2], leading to unexpected problems in products. Hence, to improve the functionality and stability of devices, the physical properties of tiny and thin polymer pieces must be precisely controlled after understanding the surface and interfacial effects.

In 1993, Reiter demonstrated anomalous dynamics of polystyrene (PS) in ultrathin films on the basis of de-wetting kinetics [3]. Ultrathin films started to break even at a temperature below the bulk glass transition temperature ($T_g^b$). Such a de-wetting behavior can be attained only by molecular motion on a relatively large scale. In addition, hole growth in the de-wet ultrathin films was much faster than that in thick films. These findings imply that the glass transition temperature ($T_g$) was lower for ultrathin films than for thick films. Then, in 1994, Keddie, Jones and

Cory, using ellipsometry, studied the temperature dependence of film thickness for PS films on Si etched with HF and found that $T_\mathrm{g}$ decreased with decreasing film thickness [4]. This study has prompted a number of additional studies [5–14]. As a result, it was found that the interaction between segments and solid substrate is one of the controlling factors for $T_\mathrm{g}$ of thin films. If an attractive interaction exists between them, the $T_\mathrm{g}$ of the thin films increases over that in the bulk because the substrate interface strongly restricts molecular motion in the films. Otherwise, the $T_\mathrm{g}$ is less than the bulk value, because of the presence of a surface layer in which molecular motion is more enhanced.

Forrest, Dutcher and coworkers have prepared free-standing PS films to study $T_\mathrm{g}$ in thin films [15, 16]. In this case, the film possesses two free surfaces instead of a combination of a free surface with the substrate interface. Their Brillouin light scattering measurements revealed that $T_\mathrm{g}$ for the free-standing thin films was lower than the $T_\mathrm{g}^\mathrm{b}$ and that the extent of the difference was much more striking for the free-standing thin films than for those supported on the substrates. This result convincingly shows that the surface and interfacial effects are crucial factors that affect the thermal properties of ultrathin polymer films. However, the aforementioned studies tried to understand the average thermal behavior in the films.

There have also been studies on how the relaxation dynamics is distributed in the film along the direction normal to the surface. Dielectric relaxation spectroscopy enables us to gain access to the segmental dynamics in thin and ultrathin polymer films. Fukao and Miyamoto revealed that the distribution of relaxation times for the $\alpha$ process in PS thin films broadened with decreasing thickness, in addition to the $T_\mathrm{g}$ depression [17]. They discussed these experimental results in terms of a three-layer model with different mobilities: liquid-like, bulk-like, and dead layers. Torkelson and coworkers systematically studied the surface and interfacial effects on the $T_\mathrm{g}$ of thin and ultrathin polymer films by temperature-dependent fluorescence spectroscopy [18]. Inserting a layer containing fluorescent probes into a desired vertical position in the film, they succeeded in collecting information about $T_\mathrm{g}$ at various depths in the film. However, a clear variability of $T_\mathrm{g}$ at the interface with a substrate was not discerned in the depth region of 12 nm from the substrate. On the basis of inelastic neutron scattering measurements, Kanaya, Inoue and coworkers claimed the existence of the dead layer with the thickness of about 5 nm [19]. They also examined the relation of thickness to $T_\mathrm{g}$ for PS films on Si substrates with a native oxide layer [20]. When the film thickness went beyond approximately 10 nm, $T_\mathrm{g}$ was invariant even with decreasing thickness. This implies that in such an ultrathin region, the interfacial effect serves as a counterbalance to the surface effect. O’Connell and McKenna examined the creep compliance functions directly from the stress and strain data at a given temperature and thickness using a micro-bubble inflation method [21]. They rationalized their results taking into account the distribution of chain mobility normal to the surface.

In this review, we show our own results of thermal molecular motion of PS at the free surface by mainly scanning force microscopy and at the substrate interface by space-resolved fluorescence spectroscopy. To do so, we also adopt coarse-grained molecular dynamics simulation to strengthen experimental results. Finally, we revisit the distribution of chain mobility along the direction normal to the surface by dynamic mechanical analysis. PS used in our experiments was synthesized by an anionic polymerization and thus its polydispersity index for all samples was lower than 1.1, or monodispersed.

## 2 Surface

### *2.1 Two-Dimensional Modulus Mapping*

First of all, it is visually evident how thermal molecular motion at the surface in PS films is active in comparison with that in the internal bulk phase. To show this, modulus mapping at the surface was made as a function of temperature using scanning viscoelasticity microscopy (SVM) [22]. At first, a PS film with a number-average molecular weight ($M_n$) of $1 \times 10^6$ was in part scratched by a blade so that the silicon substrate was exposed to the air. Figure 1a shows a topographic image of the partly scratched PS film [23]. The height difference between the unscratched and valley regions was approximately 100 nm and was in good accord with the film thickness evaluated by ellipsometry. Hence, it is clear that the higher and lower regions in the image correspond to the PS and silicon wafer surfaces, respectively. Figure 1b shows two-dimensional mapping of surface modulus in the film at room temperature, which was simultaneously obtained with the topographic image [23]. Brighter and darker areas correspond to higher and lower modulus regions, respectively. Since the PS and silicon moduli at room temperature are $3 \sim 4$ and 280 GPa, respectively, it is reasonable to claim that the PS surface was observed as the lower modulus region in the SVM image. To gain access to the absolute value of surface modulus by SVM, it is necessary to evaluate how a tip contacts with the surface [24]. This has been experimentally carried out at a given temperature. However, the temperature varies in this experiment, and this leads to technical difficulties in examining the temperature dependence of tip contact manner with the surface. Hence, the apparent surface modulus is here expressed in arbitrary unit.

Figure 2 shows the SVM images for the PS film collected at various temperatures from 200 to 400 K [23]. The surface modulus of the silicon substrate should be invariant with respect to temperature in the employed range, meaning that the contrast enhancement between the PS and Si surfaces with temperature reflects that the modulus of the PS surface starts to decrease. In the case of a lower temperature, the image contrast was trivial, as shown in the top row of Fig. 2. On the other hand, as the temperature went beyond 330 or 340 K, the contrast between the PS and Si surfaces became remarkable with increasing temperature. This makes it clear that the PS surface reached a glass–rubber transition state at around these temperatures. Here, it should be recalled that the $T_g^b$ of the PS by differential scanning calorimetry (DSC) was 378 K. Therefore, it can be claimed that surface glass transition temperature ($T_g^s$) in the PS film is definitely lower than the corresponding $T_g^b$.

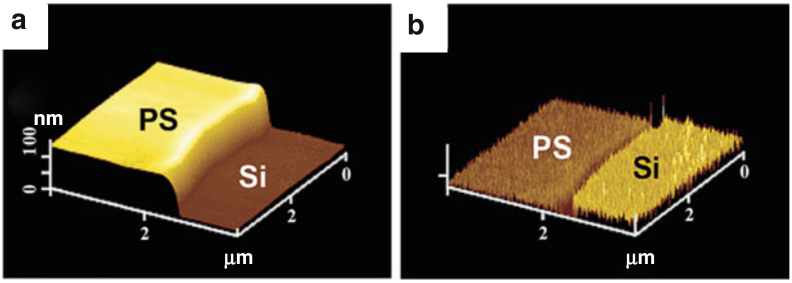

**Fig. 1** PS film in part scratched by a blade: (**a**) surface morphology by AFM and (**b**) modulus mapping by SVM

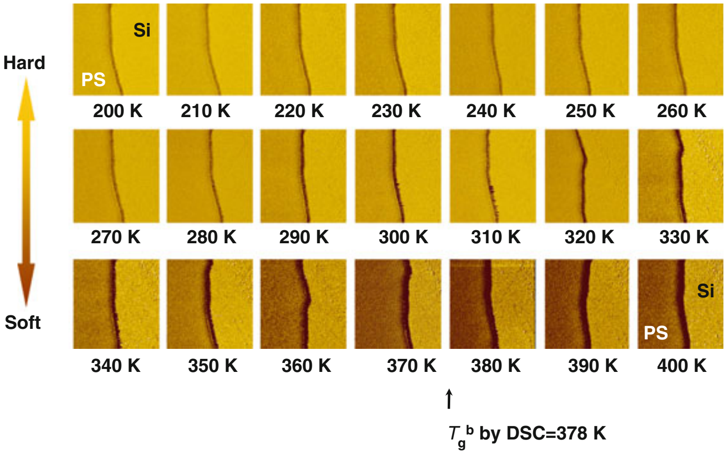

**Fig. 2** SVM images of the film shown in Fig. 1 at various temperatures. The left- and right-hand side regions in each image correspond to PS and Si surfaces, respectively

## 2.2 *Glass Transition*

In this section, glass transition behavior at the surface in the PS films is discussed. Our experimental technique to probe this was lateral force microscopy (LFM) in addition to SVM. The details of why LFM can reveal such behavior are described elsewhere [24, 25]. In short, the central part of the idea is that lateral force, namely frictional force, is essentially related to energy dissipation. That is, lateral force is somehow proportional to loss modulus at the surface.

Figure 3 shows the lateral force versus temperature curves for the PS films with $M_n$ of $4.9 \times 10^3$ (4.9k) and 140k at a fixed scanning rate ($v$) of 1 µm s$^{-1}$ [26]. The thickness of the films was approximately 200 nm, which was sufficient to avoid the thinning effect on $T_g$ [27]. The ordinate is normalized by the peak value of lateral

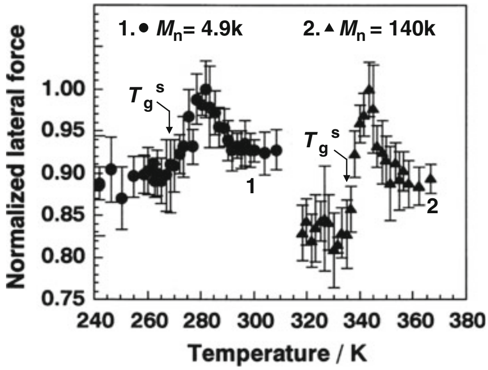

**Fig. 3** Temperature dependence of lateral force curves at a given scanning rate. The curves for PS samples with $M_n$ of 4.9k and 140k at the scanning rate of 1 μm s$^{-1}$ are displayed. The $T_g^b$ values measured by DSC were 348 and 376 K, respectively

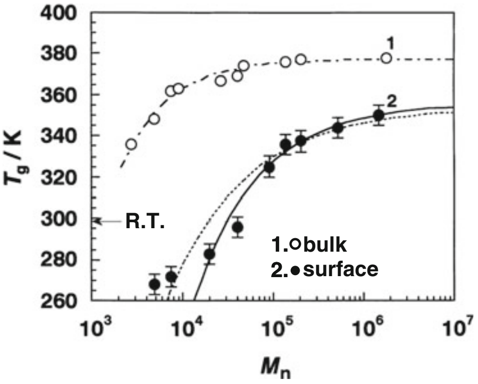

**Fig. 4** Molecular weight dependences of $T_g^b$ and $T_g^s$ of the monodisperse PS, which were determined by DSC and LFM, respectively. The *arrow* beside the ordinate shows the room temperature. The *dotted curve 2* traces the $T_g^s$ variations with $M_n$ as deduced by Mayes' scaling theory. The *dashed curve* 1 is drawn on the basis of the empirical equation established by Fox and Flory. The *solid curve* is drawn in the context of the power law analysis

force to show how the lateral force varies with temperature in the vicinity of a transition region. The lateral force-temperature curves shown in Fig. 3 reveal that each surface transition temperature for the PS films with $M_n$ of 4.9k and 140k is much lower than their $T_g^b$ of 348 and 376 K, respectively, as measured by DSC. This enhanced mobility at the surface has been in part explained in terms of the surface localization of chain end groups [24, 28–33], which might induce an extra free volume in the surface region. An onset temperature on the lateral force-temperature curve, that is, the temperature at which lateral force starts to increase, can be empirically defined as $T_g^s$.

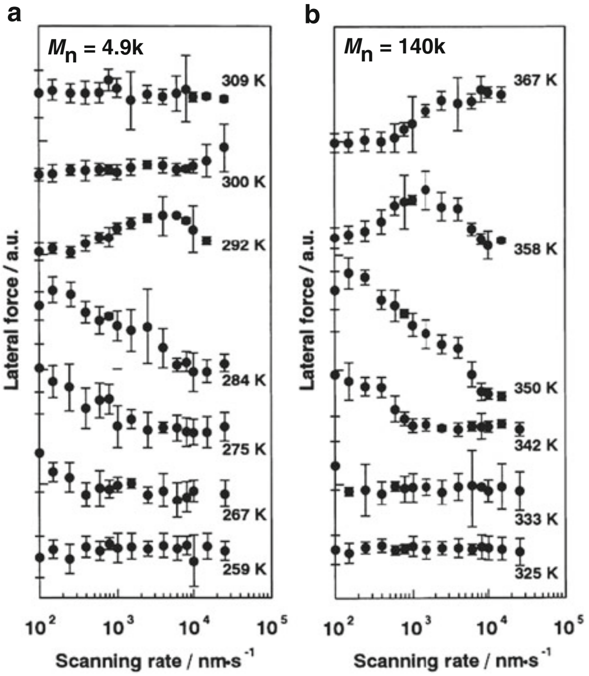

**Fig. 5** Scanning rate dependence of the lateral force at various temperatures for the monodisperse PS films with $M_n$ of (**a**) 4.9k and (**b**) 140k

Figure 4 shows $T_g^s$, obtained as a function of $M_n$, and $T_g^b$ as determined by DSC [26]. The arrow beside the ordinate denotes our room temperature. $T_g^s$ exhibited a stronger $M_n$ dependence than $T_g^b$. Even at the ultrahigh $M_n$ of 1,450k, at which the chain end effect should be ignored, the $T_g^s$ was definitely lower than the $T_g^b$. The $T_g^s$ value was dependent on chain end chemistry at a given $M_n$ (not shown) [34]. The extent of the $T_g$ depression at the surface was more striking for PS terminated with hydrophobic groups. Thus, although there is no doubt that the chain end segregation is one of factors determining the $T_g$ depression at the surface, the effect cannot perfectly account for the enhanced mobility at the surface. Besides, the film surface was already in a glass–rubber transition or rubbery state at room temperature in the case of $M_n$ smaller than approximately 40k. These results are in good accord with our parallel experiment using another technique, SVM [34].

Next, we will discuss whether the time–temperature superposition still holds at the surface. Figure 5 shows the relationships between scanning rate and lateral force on the PS films with $M_n$ of 4.9k and 140k at different temperatures [26]. In both PS films, the lateral force was independent of the scanning rate at lower temperatures such as 259 and 325 K, as shown at the bottom of Fig. 5. It should be noted that the lateral force is invariant across two decades in the scanning rate if the surface is in a glassy state. Figure 5 shows that both surfaces with $M_n$ values of 4.9k and 140k are

**Fig. 6** Master curves of the scanning rate–lateral force relationship for the PS films with $M_n$ of 4.9k and 140k drawn from the each curve in Fig. 5. Reference temperatures of 267 and 333 K were used for the PS films with $M_n$ of 4.9k and 140k, respectively

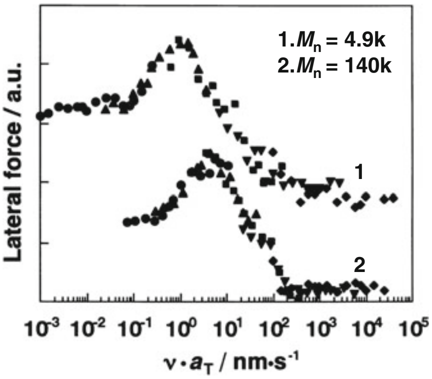

in the glassy state up to about 259 and 325 K. These are in good accord with the results presented earlier that $T_g^s$ with $M_n$ values of 4.9k and 140k are 267 and 335 K, as shown in Fig. 4. When the measurement was carried out at higher temperatures, e.g., from 267 to 275 K and from 333 to 342 K for the PS films with $M_n$ of 4.9k and 140k, respectively, the lateral force increased with decreasing scanning rate, especially at the lower scanning rates. Further, the lift-off point on the lateral force–scanning rate curve was shifted to the higher scanning rates. As the PS film was heated, a peak was clearly observed on the lateral force–scanning rate curve. The peak appeared in the temperature ranges of 284–292 K and 350–367 K for the samples of 4.9k and 140k, respectively. At temperatures higher than 300 and 367 K for the samples of 4.9k and 140k, the lateral force decreased with decreasing scanning rate. Eventually, the lateral force recovered the invariance with respect to the scanning rate, and this is shown at the top of Fig. 5a. Thus, the overall profiles reflect a successive change in the surface molecular motion from the glassy state to the rubbery state via the transition with increasing temperature. Because the performance of the piezoscanner was not stable at a temperature higher than 373 K, the LFM measurement for the PS with $M_n$ of 140k was truncated at 367 K. The shape of each curve in Fig. 5 suggests that the master curves for the lateral force–scanning rate relation might be obtained by the horizontal and vertical shifts. Since the error bar was not necessarily small, only the horizontal shift ($a_T$) was quantitatively evaluated.

Figure 6 shows the master curves for the PS films with $M_n$ of 4.9k and 140k drawn by horizontal and vertical shifts of each curve shown in Fig. 5 at the reference temperatures of 267 and 333 K, respectively [26]. The master curves obtained from the dependence of lateral force on the scanning rate were very similar to the lateral force–temperature curves, as shown in Fig. 3. Hence, it seems plausible as a general concept that the scanning rate dependence of the lateral force exhibits a peak in a glass–rubber transition. Also, it is clear that the time-temperature superposition principle, which is characteristic of bulk viscoelastic materials [35], can be applied to the surface relaxation process as well. Assuming that $a_T$ has a functional form of Arrhenius type [36, 37], the apparent activation energy for the $\alpha_a$-relaxation process, $\Delta H^{\ddagger}$, is given by:

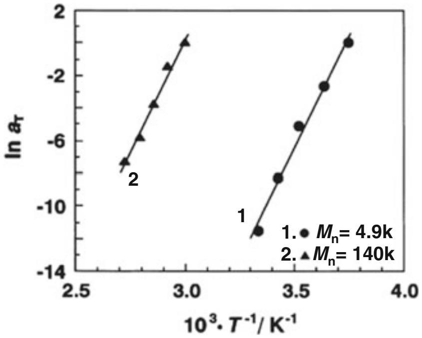

**Fig. 7** Semilogarithmic plots of shift factor, $a_T$, versus reciprocal absolute temperature for the PS films with $M_n$ of 4.9k and 140k

$$\ln a_T = \frac{\Delta H^{\ddagger}}{R}\left(\frac{1}{T}\right) \tag{1}$$

where $R$ is the gas constant and $T$ is the measurement temperature. Figure 7 shows the relationship between ln $a_T$ and the reciprocal absolute temperature for the PS films with $M_n$ of 4.9k and 140k, the so-called Arrhenius plots [26]. The activation energy for the surface $\alpha_a$-relaxation process calculated from each slope in Fig. 7 was 230 ± 10 kJ mol$^{-1}$, independent of $M_n$ for the PS. This value was much smaller than reported values for bulk PS sample, which ranged from 360 to 880 kJ mol$^{-1}$ [38, 39]. This implies that the cooperativity for the segmental motion at the surface was intensively reduced in comparison with that in the interior bulk region. Once this can be accepted, it is plausible that the thermal molecular motion at the PS surface was enhanced by not only the surface localization of chain end groups but also by the reduced cooperativity.

## 2.3 Mobility Gradient

So far, it has been clear that chain mobility at the surface is much more enhanced than that in the interior region. A question that should be addressed is how deep is the region in which the mobility is enhanced. The presence of a mobility gradient in the surface region of PS is discussed with reference to the results of interdiffusion experiments using bilayer films of PS and deuterated PS (dPS), which were prepared by attaching two original surfaces together, at various temperatures.

Figure 8 shows the time evolution of interfacial thickness for the PS/dPS bilayer as a function of temperature [40]. The $M_n$ of both PS and dPS was fixed at 29k. The interfacial characterization was made by dynamic secondary ion mass spectroscopy (DSIMS). In the case of annealing at 400, 393, and 380 K (i.e., above the $T_g^b$ of 376 K), the interfacial thickness proportionally increased to a half power of the annealing time. This is in good accordance with the context of Fickian diffusion. By contrast, a unique interfacial evolution was observed at 370 K (i.e., between $T_g^s$ and $T_g^b$). At first, the bilayer interface monotonically thickened with increasing time,

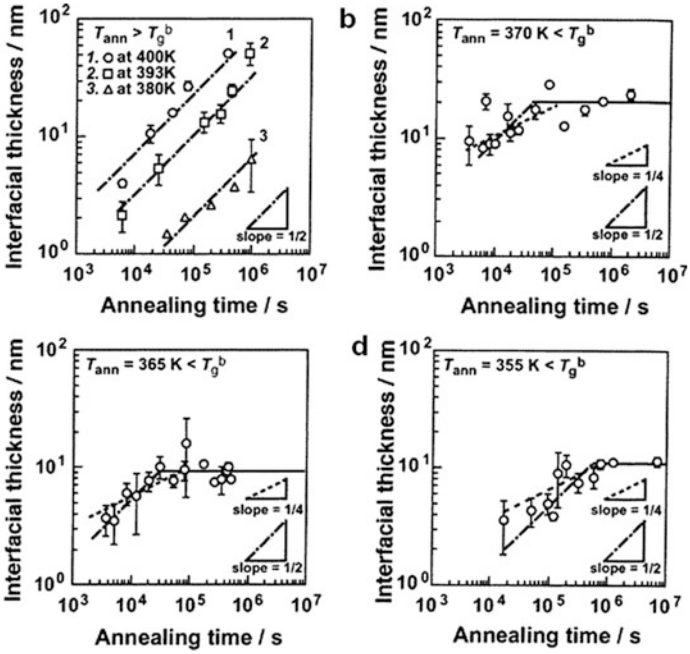

**Fig. 8** Double-logarithmic plots of the relation between interfacial thickness and annealing time for hPS/dPS bilayer annealed at various temperatures: (**a**) 400, 393, and 380 K, i.e., above both $T_g^b$ and $T_g^s$; (**b**) 370 K; (**c**) 365 K; and (**d**) 355 K. In (**b**)–(**d**) the temperatures are below $T_g^b$ and above $T_g^s$. The *dashed* and *dotted lines* are drawn in the context of Fickian and segmental diffusions, respectively

although the exponent of time could not be determined because of the data scattering. When the time proceeded to $10^5$ s, however, the interfacial thickness remained constant at 20 ± 5.6 nm. Here, it should be noted that the bilayer interface was prepared by attaching two original surfaces of hydrogenated PS (hPS) and dPS together. Thus, the data mean that chains went across the "mobile" interface and then reached the "dead" bulk region in terms of diffusivity. In other words, half of the constant interfacial thickness evolved after a sufficiently long time would correspond to the surface layer, in which the mobility is enhanced in comparison with the internal bulk phase.

The annealing temperature dependence of such a surface mobile layer will now be discussed. At 370 K, the thickness of the surface mobile layer was 10 ± 2.8 nm. It should be of interest to compare the thickness with the chain dimension. Twice the radius of gyration ($2R_g$) of an unperturbed PS with $M_n$ of 29k is calculated to be 9.3 nm. This value is comparable to the surface layer thickness. At 365 and 355 K, the interfacial thicknesses similarly increased with time at first and then became invariant with respect to the annealing time, as shown in Fig. 8c, d. The evolved interfacial thickness at 365 and 355 K were 9.6 ± 2.5 and 11.4 ± 0.9 nm, respectively. Half of these values, namely surface mobile layer thicknesses, are much

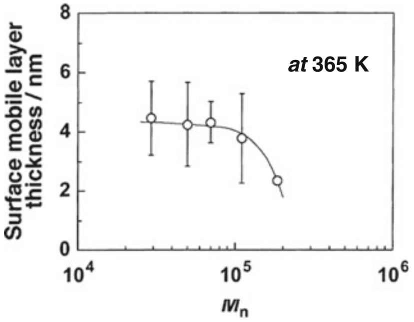

**Fig. 9** Molecular weight dependence of surface layer thickness at 365 K

smaller than the unperturbed chain dimension, implying that segmental diffusion dominates the interfacial broadening of the PS/dPS bilayers at 365 and 355 K rather than center-of-mass diffusion.

Figure 9 shows the molecular weight dependence of surface mobile layer thickness at 365 K [40]. This temperature was well below $T_g^b$ for all samples. Once it was confirmed that each bilayer interface was no longer evolving, the annealing treatment for the PS/dPS bilayers was stopped. The surface layer thickness was apparently insensitive to $M_n$ up to 110k and then started to decrease with increasing $M_n$. Because the thickness was not scaled by $M_n^{1/2}$, it is clear that the thickness of the surface mobile layer is independent of the chain dimension; the thickness was not apparently related to the $T_g$ difference between surface and bulk. Then, a question to clarified is why such a molecular weight dependence occurred as shown in Fig. 9. We again recall the chain end effect as a factor responsible for the enhanced surface mobility. Figure 10 illustrates a plausible cartoon of mobility gradients in the surface region [40]. At the depth range of a few nanometers from the surface, $T_g$ should be strongly dependent on $M_n$ because the concentration of segregated chain ends is dependent on $M_n$. Once the depth goes far beyond the segregation layer of chain ends, there is no reason why the mobility gradient in the surface region depends on $M_n$. This might be the reason for the results shown in Fig. 9.

## 2.4 Molecular Dynamics Simulation

On the basis of our results using scanning force microscopy such as SVM and LFM, we claim that the mobility at the surface of PS films is not the same as that in the bulk. However, in such measurements, a probe tip made of silicon or silicon nitride makes contact with the surface to be measured. This may induce some artifacts in the results. If an effect of tip contact on the surface dynamics cannot be negligible, our conclusion must be reconsidered. Thus, $T_g^s$ is here discussed on the basis of coarse-grained molecular dynamics simulation using a bead-spring model of Grest

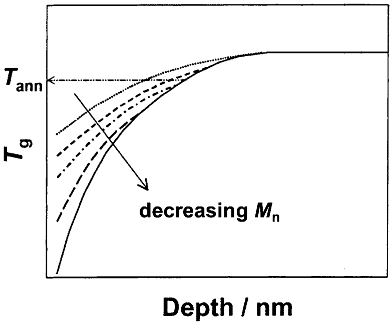

**Fig. 10** Possible model for depth dependence of $T_g$ as a function of $M_n$, showing the mobility gradient in the surface region. Within the depth region in which chain ends are segregated, the mobility gradient should be strongly dependent on $M_n$. This would be not the case far beyond the segregated surface layer of chain ends

and Kremer [41]. The polymer consists of $N$ beads connected by the following potential $U^{B}(r)$:

$$U^{B}(r) = U^{FENE}(r) + U^{LJ}(r) \tag{2}$$

where $r$ is the distance between the beads. $U^{FENE}(r)$ and $U^{LJ}(r)$ are given by:

$$U^{FENE}(r) = -(1/2)kR_0^2 \cdot \ln(1 - (r/R_0)^2), \quad (r \le R) \tag{3}$$

$$U^{FENE}(r) = \infty, \quad (r<R) \tag{4}$$

$$U^{LJ}(r) = 4\epsilon[\{(\sigma/r)^{12} - (\sigma/r)^{6}\} - \{(\sigma/r^{cut})^{12} - (\sigma/r^{cut})^{6}\}], \quad (\sigma \le r^{cut}) \tag{5}$$

$$U^{LJ}(r) = 0, \quad (r>r^{cut}) \tag{6}$$

where $k$ is the spring constant, $R_0$ is the maximum extension of the spring, $\epsilon$ is the unit of the energy, and $\sigma$ is the unit of length. The nonbonding interaction between the polymer segments separated by the distance $r$ is also given by the Lennard–Jones potential $U^{LJ}(r)$.

The time evolution of beads at position $r_n$ is calculated by the Langevin equation as follows:

$$m(\mathrm{d}^2r_n/\mathrm{d}t^2) = -(\partial U/\partial r_n) - \Gamma(\mathrm{d}r_n/\mathrm{d}t) + \mathbf{W}_n(t) \tag{7}$$

where $m$ is the mass of beads, $U$ is the total potential energy of the system, $\Gamma$ is the friction constant, and $\mathbf{W}_n(t)$ is a Gaussian white noise, which is generated according to the following equation:

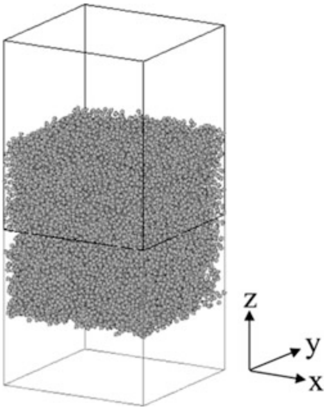

**Fig. 11** Model of polymer film used in the present work. The system consists of 100 chains each consisting of 100 beads. The size of the simulation box is $32\sigma \times 32\sigma \times 32\sigma$

$$\langle \mathbf{W}_n(t)\mathbf{W}_m(t')\rangle = 2k_\mathrm{B}Tm\Gamma\delta_{nm}I\delta(t-t') \tag{8}$$

We used the following parameter set: $k = 30.0\epsilon/\sigma^2$, $R_0 = 3.0\sigma$, $r^\mathrm{cut} = 2.0\sigma$, and $\Gamma = 0.5\tau^{-1}$, where $\tau$ is the unit of time given by $\sigma(m/\epsilon)^{1/2}$. These parameters are the same as those of Grest and Kremer except for $r^\mathrm{cut}$. The interval of one time step is $0.01\tau$. The unit of temperature is $T_0 = k_\mathrm{B}/\epsilon$.

Figure 11 shows an example of the configuration for the simulation [42]. The figure shows the actual simulation box twice because the staggered reflective boundary condition is used: the chain in the bottom box is a mirror image of that in the top box with half-periodicity shifted. The thickness of the film is about $30\sigma$, which is sufficiently larger than the root-mean-square of the polymer in the bulk region even for the largest polymer of $N = 200$. To study the segmental mobility near the surface, the film was divided into layers normal to the $z$ axis and the mean-square displacement of the segment in each layer calculated in a time interval $t$. The thickness of the layer is $\sigma$, and a segment $n$ is regarded to be in the layer $l$ for the time interval between $t'$ and $t' + t$ if the average $z$ coordinate $[z_n(t') + z_n(t' + t)]/2$ is between $\sigma_l$ and $\sigma_{(l+1)}$. The mean-square displacement of the segment in the layer $l$ is defined as follows:

$$\varphi_l(t) = \frac{\sum\limits_{t'} \sum\limits_{n\,\mathrm{in\,layer}\,l} [r_n(t'+t) - r_n(t')]^2}{\sum\limits_{t'} \sum\limits_{n\,\mathrm{in\,layer}\,l} 1} \tag{9}$$

It must be mentioned that $\phi_l(t)$ becomes inappropriate for characterizing the surface mobility if $t$ is taken to be very large: for large $t$, the diffusion of segments blurs the layer dependence of $\phi_l(t)$. For small $t$, however, $\phi_l(t)$ is a convenient quantity for characterizing the surface mobility.

Figure 12 shows $\phi_l(t^*)$ as a function of $z = \sigma l$ for various temperatures [42]. It is seen that the segmental mobility near the surface, $z = 13\sigma - 15\sigma$, differs

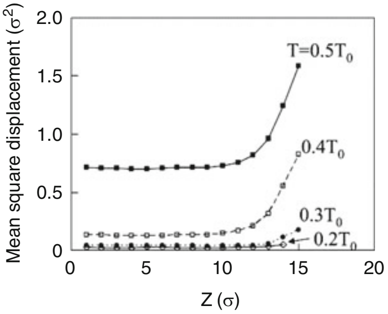

**Fig. 12** Mean-square displacement of a polymer segment in a time interval $t^*$ is plotted against the mean $z$ position of the segment for various temperatures ($N = 100$). The average is taken for each layer of thickness $1\sigma$

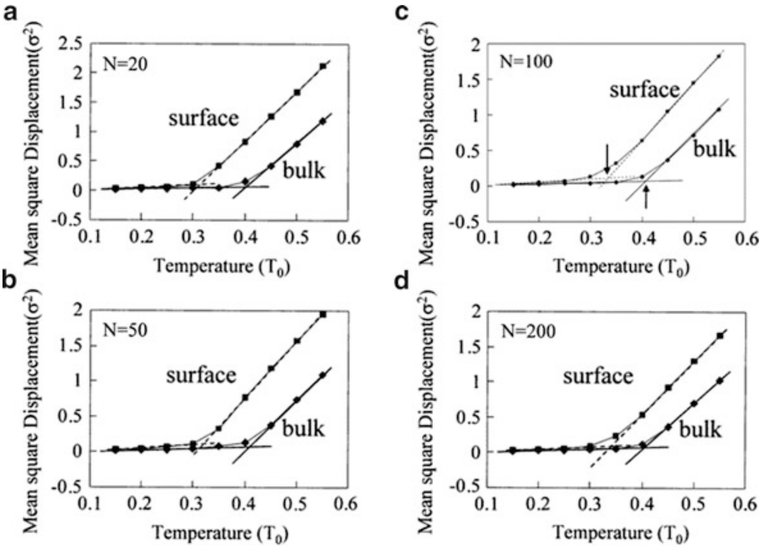

**Fig. 13** Mean-square displacements of a polymer segment are plotted against the temperature for the case of $N = 20$ (**a**), 50 (**b**), 100 (**c**), and 200 (**d**)

significantly from that in the inner region, and that this surface region is limited to the thickness of about $3\sigma$, which is about the same as that determined by the density profile. We will next describe analysis of the segmental mobility for the first three layers near the surface.

Figure 13 shows the mean-square displacement at the surface and in the bulk plotted against temperature for chains of $N = 20$, 50, 100, and 200 [42]. It is seen that the mean-square displacement starts to increase sharply at a certain temperature, which can be associated with $T_g$. The characteristic temperature can be

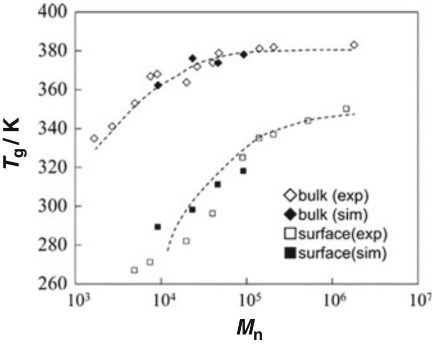

**Fig. 14** Glass transition temperatures are plotted against the molecular weight. *Filled symbols* indicate the results of molecular dynamics simulation, and *open symbols* indicate the results of the SFM experiment [26]

obtained by the intersection of the two lines characterizing the behavior at low and high temperatures. In all cases, the transition temperatures are clearly obtained.

Figure 14 shows the comparison between the experimental $T_g^s$ by scanning force microscopy and that obtained by this simulation [42]. The agreement between the experiment and simulation looks to be very good. This indicates that the change of the $T_g$ near the surface is well represented by the simulation. That is, it can be claimed that the effect of tip contact on $T_g^s$ is trivial, if any. In conclusion, the chain mobility in the surface region is enhanced in comparison with that in the interior region, and the extent of the enhancement becomes more significant with proximity to the outermost surface.

# 3 Substrate Interface

## *3.1 Glass Transition*

In this section, thermal molecular motion at the interface with solid substrates is discussed. It is needless to say that the issue is of pivotal importance for inherent scientific interest because motion at the interface seems to be totally different from that at the polymer surface. Also, the interface between polymers and inorganic materials is crucial in designing and constructing highly functionalized nanocomposites [43–45], which are now used for biomaterials [46, 47], sensors [48, 49], power sources [50, 51], etc., in addition to their popular and traditional use as structural materials [43–45, 52, 53].

We have developed a direct and noninvasive method to determine $T_g$ of polymers at the interface with solid substrates [54, 55]. The strategy is to use fluorescence lifetime measurements using evanescent wave excitation. Figure 15a shows PS-NBD, i.e., PS containing the dye 6-[*N*-(7-nitrobenz-2-oxa-1,3-diazol-4-yl)amino]hexanoic acid (NBD) [55]. The NBD fraction of PS was sufficiently low to avoid self-quenching of the dye. The NBD dye was excited with the second-harmonic generation of a mode-locked titanium:sapphire laser equipped with a

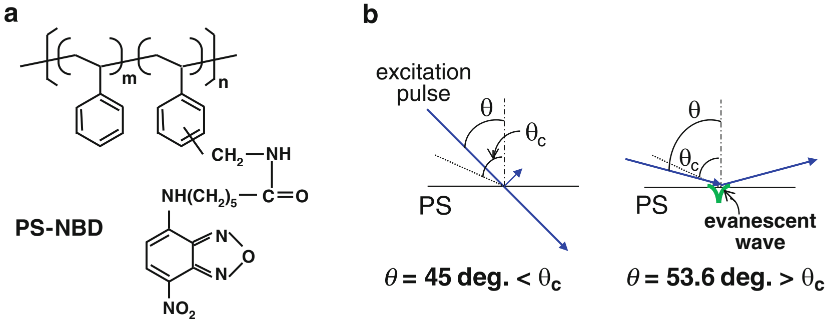

**Fig. 15** (**a**) Chemical structure for PS-NBD. (**b**) Scheme for the measurement at $\theta$ =45° and 53.6°, being respectively smaller and larger than the critical angle of $\theta_c$

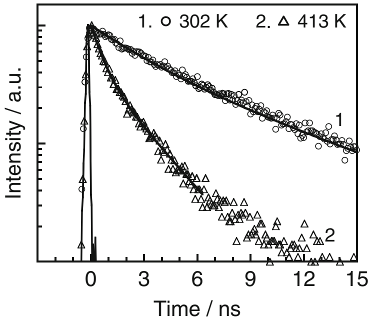

**Fig. 16** Fluorescence decay curves from NBD tagged to PS with $M_n$ of 53.4k in a film at 302 and 413 K

pulse selector and a harmonic generator. A streakscope was used to detect the time-resolved fluorescence from excited NBD molecules. Figure 15b shows the principle of the measurement. An excitation pulse was irradiated on the film from the substrate side via a prism at various incident angles. When the incident angle ($\theta$) is larger than the critical angle ($\theta_c$), the excitation pulse is totally reflected at the interface between the PS and the substrate. In this case, an evanescent wave, where the electric field exponentially decays along the direction normal to the interface, is generated at the PS interface. Information near the substrate interface was extracted on the basis of this evanescent wave excitation.

Figure 16 shows the time ($t$) dependence of the fluorescence intensity ($I$) from a PS film labeled with NBD dyes observed at 302 and 413 K [55]. The decay curves were fitted by the following double-exponential equation with two time constants, $\tau_{\text{fast}}$ and $\tau_{\text{slow}}$:

$$I = I_0\{(1-x)\exp(-t/\tau_{\text{fast}}) + x\exp(-t/\tau_{\text{slow}})\} \tag{10}$$

**Fig. 17** Temperature dependence of the lifetime for NBD tagged to PS with $M_n$ of 53.4k in a film. Lifetimes are normalized by the value obtained at room temperature

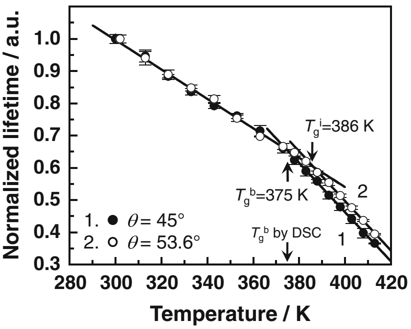

where $I_0$ and $x$ are the fluorescence intensity right after the excitation and the fraction of the slow component, respectively. While $\tau_{slow}$ was 7.45 ± 0.11 ns at 302 K, it decreased to 2.69 ± 0.01 ns at 413 K. This is simply because the fractional amount of non-radiative pathways to the ground state for excited species increased with temperature.

Next, lifetime measurements for NBD tagged to PS with $M_n$ of 53.4k in the film on the S-LAH79 substrate, which was a glass with a higher refractive index, were made as a function of temperature. The $\theta_c$ value for this system can be simply calculated to be 51.3° by Snell's law. Figure 17 shows the temperature dependence of the fluorescence decay time constants at $\theta = 45°$ and 53.6° [55]. In the case of $\theta = 45°$, the excitation pulse went through the internal bulk phase of the film, meaning that the data reflect bulk information. The lifetime decreased with increasing temperature, and the slope was changed at 375 K, as shown by the filled circles in Fig. 17. As the measurement temperature increases beyond the temperature at which molecular motion releases, the slope of the temperature–lifetime relation should change because the dynamic environment surrounding the dye molecules changes at that temperature [18, 54]. Actually, the inflection point related to the slope change coincided with the $T_g^b$ for the matrix PS of 375 K found by DSC. Thus, it is reasonable to claim that the fluorescence lifetime measurement using NBD probes tagged to a polymer allows us to determine the $T_g$ of the matrix polymer.

When the $\theta$ value was higher than $\theta_c$, the incident pulse was totally reflected at the interface between the PS and S-LAH79 substrate. That is, the NBD dye molecules near the interface were selectively excited by the evanescent wave. Hence, the data set obtained at $\theta = 53.6°$ reflects the interfacial molecular motion. The inflection temperature, which can be assigned to the interfacial $T_g$ ($T_g^i$) at $\theta = 53.6°$, was 386 K, and was discernibly higher than the $T_g^b$. This is direct evidence for depressed mobility at the interface.

## 3.2 Mobility Gradient

The analytical depth of the above-mentioned technique is discussed in this section. The penetration depth ($d_p$) of the evanescent wave is given by [56]:

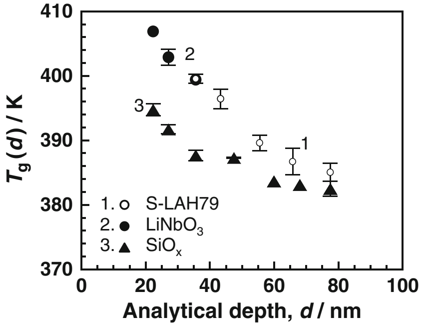

**Fig. 18** Analytical depth dependence of $T_g$ for PS with $M_n$ of 53.4k at interfaces with various substrates

$$d_p = \lambda_0(\sin^2\theta - \sin^2\theta_c)^{-1/2}/2\pi n \tag{11}$$

where $\lambda_0$ is the wavelength of the excitation light. In fact, the relation between the depth and the electric field intensity ($I_{ev}$) is much more important for the interfacial selectivity than the $d_p$ value [56]:

$$I_{ev} = I_{ev,o}\exp(-2\zeta/d_p) \tag{12}$$

Here, $\zeta$ is the depth from the interface. The analytical depth ($d$) is defined as the position at which $I_{ev}$ becomes $I_{ev,o}/e$, namely, the value of $I_{ev}$ corresponding to ($d_p$/2). The minimum $d$ value attained in our experiment was 22.4 nm for the interface between LiNbO$_3$, which was also a material with a higher refractive index, and PS at $\theta = 74°$. This value appears to be larger than the depth range in which the mobility gradient exists. However, taking into account the fact that the electric field intensity of the evanescent light is the strongest at the interface and exponentially decays with increasing depth, it is likely that the results obtained by the method proposed in this study mostly reflect the chain mobility near the interface with the solid substrate.

Equations show that the $d$ value can be regulated by changing the angle $\theta$ of the excitation pulse and/or the refractive index $n$ of the inorganic substrate. The $d$ value decreases with increasing $\theta$. In addition, two different substrates were used: an optical glass (S-LAH79) with an $n$ of 2.05 and LiNbO$_3$ with an $n$ of 2.30. To attain a smaller $d$ value, the $n$ value should be larger. However, it must be kept in mind that an alteration of the substrate causes a change in the interaction between PS and substrate. Figure 18 shows the relation between the analytical depth and $T_g$ for PS with $M_n$ of 53.4k on S-LAH79 and LiNbO$_3$. As a general trend, the $T_g$ value increased with decreasing analytical depth. Interestingly, the curves for PS on S-LAH79 and LiNbO$_3$ are superimposed. To investigate this, the surface free energy for both substrates was examined by contact angle measurement with water and diiodomethane as probe liquids [57]. The numbers so obtained for S-LAH79 and LiNbO$_3$ were 38.1 and 38.3 mJ m$^{-2}$. These values can be regarded as the same within the experimental accuracy. Thus, it seems most likely that the surfaces of S-LAH79 and LiNbO$_3$ are chemically the same, probably due to the antireflective surface coating, and hence the interaction between PS and the substrate is the same in the two cases.

According to Maxwell's equation for electromagnetic waves [58, 59], the analytical depth $d$ is not changed even when the surface of a medium with a higher refractive index is coated with a layer, provided that the thickness of the layer is less than the analytical depth. On the other hand, the chemical interaction between a polymer and the substrate should be strongly altered due to the presence of the layer. Accordingly, both S-LAH79 and $LiNbO_3$ coated with a thin $SiO_x$ layer with a thickness of at most 10 nm were used as substrates. Here, the combination of PS with $SiO_x$ is regarded as a model system for a PS film on a silicon wafer. In this case, the $d$ value was controlled by the refractive indices of PS and the substrate in addition to the incident angle of the excitation pulse. The $T_g$ value for PS on S-LAH79 and $LiNbO_3$ coated with a thin $SiO_x$ layer increased with decreasing analytical depth, as marked by the filled triangles in Fig. 18. Although the variation was similar for both S-LAH79 and $LiNbO_3$ substrates, marked by open and filled circles in Fig. 18, the extent was clearly depressed. The surface free energy of S-LAH79 and $LiNbO_3$ was approximately 38 mJ $m^{-2}$, comparable to that of PS, 40.6 mJ $m^{-2}$. On the other hand, the value for the $SiO_x$ layer was measured to be 61.2 mJ $m^{-2}$, indicating an unfavorable interaction between PS and $SiO_x$. This may cause a reduction in the amount of restriction of segmental motion at that interface. Then, a question that arises is why $T_g$ must increase at the substrate interface without an attractive interaction. For the moment, we suggest that the interface, which can be regarded as a hard wall, acts as an obstacle to the movement of polymer chains. As far the chain mobility at the outer most interface, we also studied the chain conformation of the PS, at a quartz substrate interface by sum-frequency generation (SFG) spectroscopy [60]. The chain conformation at the interface with the neutral substrate was not altered even at temperatures in excess of the corresponding bulk $T_g$. This also implies that polymer chains at the substrate interface are not much relaxed under the usual annealing condition determined from the polymer dynamics in the bulk.

### *3.3 Molecular Dynamics Simulation*

The space- and time-resolved fluorescence spectroscopy clearly revealed that there exists a mobility gradient proximal to the substrate interface. However, it was not possible to gain access to mobility information in the depth shallower than 20 nm by this method. This again motivated us to estimate $T_g$ as a function of the distance from the interface on the basis of coarse-grained molecular dynamics simulation (details are given in Sect. 2.4). Figure 19 shows the mean-square displacement at surface, bulk, and interface plotted against temperature for 170 chains [55]. One chain consists of 100 segments, which is larger than the critical number of segments that will initiate entanglements (i.e., 35). The mean-

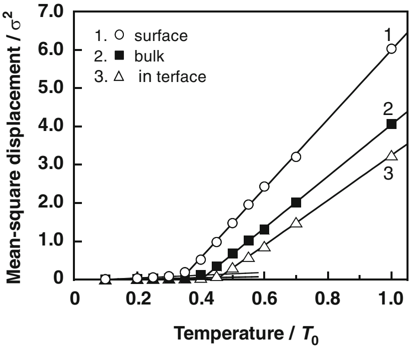

**Fig. 19** Temperature dependence of mean-square displacement in three regions: surface, bulk, and interface. The data in each region (surface, bulk, and interface) is averaged over values in three layers of the simulation model, or $3\sigma$

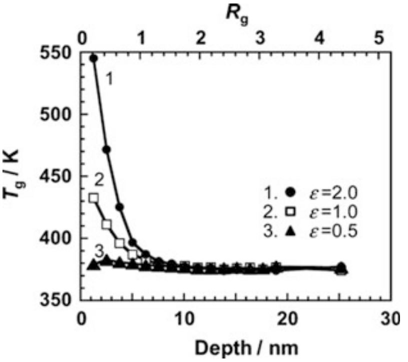

**Fig. 20** Depth dependence of $T_g$ for PS obtained by coarse-grained molecular dynamics simulation. The 0 depth is at the substrate interface, and the value is in a real space. The *upper abscissa* is expressed by the chain dimension using radius of gyration ($R_g$) for an unperturbed polymer chain. The ε value corresponds to Lennard–Jones energy between segments and substrate wall

square displacement started to increase sharply at a threshold temperature here defined as $T_g$, which was obtained from the intersection of the two lines characterizing the behavior at low and high temperatures. The $T_g$ values at the surface, in the bulk, and at the substrate interface were claimed to be $0.35T_0$, $0.41T_0$, and $0.46T_0$, respectively.

Figure 20 shows the relation of $T_g$ to depth from the interface. The $T_g$ increased closer to the interface [55]. This trend became striking with increasing interaction between segments and substrate, namely, with an increase in the parameter ε. Interestingly, the depth region in which $T_g$ was elevated was on the order of the radius of gyration of an unperturbed chain. On the other hand, in the case of the smallest ε ($\varepsilon = 0.5$), a clear elevation of $T_g$ at the substrate interface was not

**Fig. 21** Temperature dependence of the loss modulus $E''$ for PS1.46M thin and ultrathin films coated on PI substrates. The data for a control PI are also shown

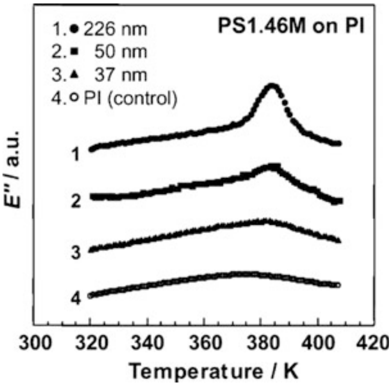

observed. These results indicate the extent to which $T_g$ increases at the substrate interface is strongly dependent on the surface free energy of the substrate, and are in good accord with the experimental results.

# 4 Thin Films

## 4.1 *Supported Film*

Finally, dynamic mechanical analysis (DMA) for PS in thin and ultrathin films is discussed. Studies over the past 15 years have shown that the $T_g$ of nanometer thick polymer films can vary significantly with the film thickness ($h$) when $h$ falls below 50 nm [61–65]. Although the $T_g$ has been found to both increase [5, 66, 67] and decrease [4, 10, 63, 68, 69] with decreasing $h$, the latter has drawn vastly more attention because of the significantly bigger size of the effect.

A Rheovibron DDV-01FP (A&D, Tokyo, Japan) tester has been used for DMA. In general, DMA has been accepted as a powerful method for studying the relaxation behavior of bulk samples. However, previous to these experiments, no one knew whether the technique was sensitive enough to be used with thin and ultrathin polymer films. To answer this question, a dynamic viscoelastic measurement for thin PS films supported on substrates was conducted.

Figure 21 shows the temperature dependence of the loss modulus ($E''$) for PS films of various thicknesses on polyimide (PI), together with the data for a control PI substrate. For reasons of space, only the data at the frequency of 11 Hz are presented. In the case of the 226 nm film, an $\alpha_a$ absorption peak corresponding to the segmental motion was observed on the temperature–$E''$ curve at around 380 K. The peak temperature was dependent on the frequency (not shown), meaning that the peak was assignable to not artifacts but to a relaxation process. This result is in good accordance with the corresponding bulk data.

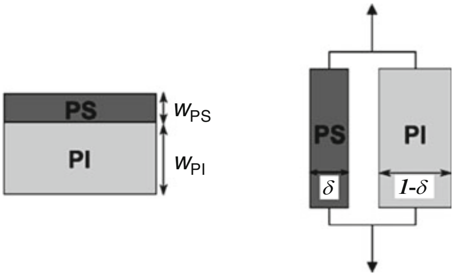

**Fig. 22** Schematic representation of Takayanagi's parallel model for PS on PI. See text for details

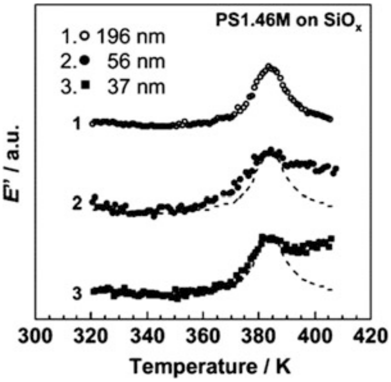

**Fig. 23** Temperature dependence of $E''$ for PS1.46M thin and ultrathin films on SiO$_x$ substrates

Because the volume ratio of the PS phase to that of the total system, the intensity of the $\alpha_a$ relaxation peak for the PS decreased as the films became thinner. However, a mechanical model analysis was able to be applied to the raw data to extract the contribution from the PS phase.

Figure 22 illustrates Takayanagi's parallel model, in which the dynamic strain is everywhere constant [70]. Here, $w$ is the film thickness in nanometers and $\delta$ is the volume fraction of PS. On the basis of this model, $E''$ can be formulated for a PS film coated on PI ($E''_{\text{all}}$) by:

$$E''_{\text{PS}} = \{(w_{\text{PI}} + w_{\text{PS}})E''_{\text{all}} - w_{\text{PI}}E''_{\text{PI}}\}/w_{\text{PS}} \tag{13}$$

Figure 23 shows the temperature dependence of background-subtracted $E''$ as a function of thickness for PS films of $1.46 \times 10^6$ $M_n$ (PS1.46M) on the SiO$_x$ substrate. The values of $E''$ for the ultrathin films were again arbitrarily rescaled to have the same peak height as that for the 200 nm thick films. The $\alpha_a$ absorption peak was clearly observed, even for the ultrathin films with thicknesses of 56 and 37 nm. The temperature absorption curve for the 196 nm film on the SiO$_x$ was in good accordance with that for the 226 nm film on the PI, a result suggesting that the interfacial effect on the $\alpha_a$ relaxation process is negligible in this thickness region. More precisely, even if the surface and interfacial effects on molecular motion exist, they are not detectable for this thickness range. On the other hand, for the thinner films, the shape of the $\alpha_a$ absorption peak depended on which substrate was used. An obvious difference was observed between the ultrathin films on the $SiO_x$ and PI substrates on the higher temperature side of the peak. For the ultrathin films on the PI, $E''$ monotonically decreased with increasing temperature, as shown in Fig. 21. In contrast, in the case of the ultrathin films on the $SiO_x$ substrates, $E''$ slightly decreased, and then remained almost constant, or increased again after the peak, as shown in Fig. 23. This result implies that the fractional amount of slower relaxation times in the ultrathin films on the $SiO_x$ is larger than that in the corresponding films on the PI. Thus, it seems most likely that the chains that are in contact with the $SiO_x$ layer are less mobile than those next to the PI. For the ultrathin films on the PI, the peak broadening on the lower temperature side became more marked with decreasing thickness. Postulating that the surface segmental motion might be more detectable with decreasing thickness due to the larger surface-to-volume ratio, this result seems reasonable. However, we observed a unique thickness dependence of the broadening for the ultrathin films on the $SiO_x$. In the case of the 56 nm thick film, we noted the peak broadening on the lower temperature side, but on the other hand, we did not observe it for the thinner, 37 nm thick film. These findings may indicate that the molecular motion in the surface region is inhibited by a restriction from the interface, if the interfacial effect is strong.

## 4.2 Sandwiched Film

According to the above-mentioned results, it is expected that the restriction from the interface should be striking for the ultrathin PS films sandwiched between the $SiO_x$ layers. Therefore, the segmental motion in PS films sandwiched between $SiO_x$ layers, in which the top layer was prepared by a vacuum-deposition procedure, is discussed next.

Figure 24 shows the temperature dependence of background-subtracted $E''$ as a function of thickness for the PS1.46M films between the $SiO_x$ layers. Even in the case of the 211 nm film, an additional shoulder on the higher temperature side of the $\alpha_a$ relaxation peak was observed. As the film thinned, the high-temperature shoulder evolved and eventually became a clear peak. Since the presence of the additional peak for the 37 nm film sandwiched between the $SiO_x$ layers depended on the frequency employed, it is clear that the peak derived from a relaxation process. In addition, in the case of the sandwiched films, the relaxation peak did not broaden on the lower temperature side, even though the films became thinner. This result can be easily understood by taking into account the film geometry. In other words, the free surface disappeared under the capping $SiO_x$ layer, and the interfacial region with the $SiO_x$ layer doubled. On the basis of the results mentioned above, we suggest that

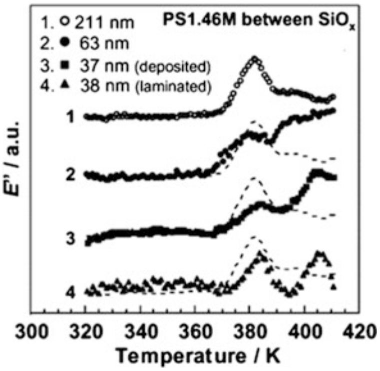

**Fig. 24** Temperature dependence of $E''$ for PS1.46M thin and ultrathin films sandwiched between SiO$_x$ layers

the main and additional peaks observed at the lower and higher temperature regions should be assigned respectively to the $\alpha_a$ relaxation processes in the internal phase and the interfacial layer.

However, there is a possibility that the sandwiched films were thermally damaged by the vacuum-deposition procedure [71], although such a damage was not visible in the microscopic observations. Hence, to investigate this likelihood, we prepared a PS1.46M ultrathin film sandwiched with SiO$_x$ layers by laminating two PS films on SiO$_x$ layers. In this case, the film should not have suffered any thermal damage. The result for the sandwiched film prepared by the lamination is also shown in Fig. 24 and clearly shows the additional peak in the higher temperature region. Although the intensity of the additional peak was different in the two sandwiched films prepared by different methods, their temperature regions seemed to be similar. Since the additional peak was observed only for the ultrathin PS film sandwiched with SiO$_x$ layers, it is conceivable that the peak on the higher temperature side arose from an interfacial relaxation process and was not an experimental artifact.

Figure 25 shows the temperature dependence of relaxation time ($\tau_\alpha$) for the $\alpha_a$ relaxation processes in the internal and interfacial regions of the ultrathin PS1.46M film sandwiched between the SiO$_x$ layers. Since it was hard to distinguish the temperature–$\tau_\alpha$ relations between the vacuum deposited and laminated films, each data point was averaged over six independent measurements including both vacuum deposited and laminated films. The average thickness was about 40 nm. For comparison, the dashed curve in Fig. 25 denotes the bulk data obtained by the Vogel–Fulcher equation [72, 73]:

$$\tau_\alpha = \tau_0 \exp\{B/(T - T_v)\} \tag{14}$$

Here, $T_v$ is the so-called Vogel temperature, at which the viscosity diverges to infinity. The parameter $\tau_0$ is the characteristic time related to molecular vibration and $B$ is the activation temperature. Even in the case of the internal phase, the

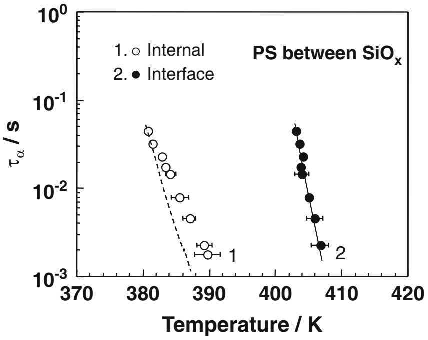

**Fig. 25** Temperature dependence of $\tau_\alpha$ for $\alpha_a$ relaxation processes in internal and interfacial regions of the PS1.46M ultrathin films sandwiched between SiO$_x$ layers. The average thickness is about 40 nm. The *dashed curve* denotes the prediction of the Vogel−Fulcher equation using bulk parameters, whereas the *solid curve* is the best fit by Vogel−Fulcher equation for the interfacial $\alpha_a$ process

temperature dependence of $\tau_\alpha$ slightly deviated from the bulk data. This discrepancy might be due to an effect of chain confinement, which appeared in the high molecular weight PS ultrathin films. However, Fig. 25 shows that the temperature relation in the interfacial layer was definitely different from that in the internal region. Since the interfacial $\alpha_a$ relaxation process seems to be independent of the internal relaxation process, the data set from the interfacial regions was fitted by the Vogel–Fulcher equation with a single Vogel temperature, as shown by the solid curve in Fig. 25. The $T_v$ so obtained was 369 ± 4 K. Now, $T_g$ is generally accepted to equal ($T_v$ + 50) K. So, even for this simplified case, the value of $T_g$ in the interfacial layer should be 419 ± 4 K, a temperature higher than the $T_g^b$ value of 378 K. This number is still averaged over a region with proximity to the substrate interface. Hence, the plausibility of this quantitative estimation for the interfacial $T_g$ value merits further discussion. However, it is evident that the segmental mobility at the interface with the SiO$_x$ layer is depressed in comparison with that for the bulk. This is in excellent accord with conclusions drawn from the previous section.

## 5 Conclusion

Thermal molecular motion of PS at surfaces and interfaces in films was presented in this review. We clearly show that chain mobility at the surface region is more mobile than in the interior bulk phase and that chain mobility at the interfacial region is less than in the interior phase. This means that there is a mobility gradient in polymer films along the direction normal to the surface. This gradient can be experimentally detected if the ratio of the surface and interfacial areas to the total volume increases, namely in ultrathin films.

**Acknowledgments** We deeply thank Professor Emeritus Tisato Kajiyama, Professor Emeritus Toshihiko Nagamura, Professor Daisuke Kawaguchi, Dr. Kei-ichi Akabori, and Dr. Yohei Tateishi for their fruitful discussion. This research was partly supported by Grant-in-Aid for Scientific Research (B) (No. 24350061), and for Science Research in a Priority Area "Soft Matter Physics" (No. 21015022) from the Ministry of Education, Culture, Sports, Science and Technology, Japan.

## References

1. Stamm M (2008) Polymer surfaces and interfaces: characterization, modification and applications. Springer, Berlin
2. Karim A, Kumar S (2000) Polymer surfaces, interfaces and thin films. World Scientific, Singapore
3. Reiter G (1993) Europhys Lett 26:579
4. Keddie JL, Jones RAL, Cory RA (1994) Europhys Lett 27:59
5. Wallace WE, van Zanten JH, Wu WL (1995) Phys Rev E 52:R3329
6. DeMaggio GB, Frieze WE, Gidley DW, Zhu M, Hristov HA, Yee AF (1997) Phys Rev Lett 78:1524
7. Prucker O, Christian S, Bock H, Ruhe J, Frank CW, Knoll W (1998) Macromol Chem Phys 199:1435
8. Fryer DS, Nealey PF, de Pablo JJ (2000) Macromolecules 33:6439
9. See YK, Cha J, Chang T, Ree M (2000) Langmuir 16:2351
10. Kim JH, Jang J, Zin WC (2000) Langmuir 16:4064
11. Tsui OKC, Zhang HF (2001) Macromolecules 34:9139
12. Kim JH, Jang J, Zin WC (2001) Langmuir 17:2703
13. Kawana S, Jones RAL (2001) Phys Rev E 63:021501
14. Xie F, Zhang HF, Lee FK, Du B, Tsui OKC, Yokoe Y, Tanaka K, Takahara A, Kajiyama T, He T (2002) Macromolecules 35:1491
15. Forrest JA, Dalnoki-Veress K, Stevens JR, Dutcher JR (1996) Phys Rev Lett 77:2002
16. Forrest JA, Dalnoki-Veress K, Dutcher JR (1997) Phys Rev E 56:5705
17. Fukao K, Miyamoto Y (2000) Phys Rev E 61:1743
18. Ellison CJ, Torkelson JM (2003) Nat Mater 2:695
19. Inoue R, Kanaya T, Nishida K, Tsukushi I, Shibata K (2005) Phys Rev Lett 95:056102
20. Miyazaki T, Nishida K, Kanaya T (2004) Phys Rev E 69:061803
21. O'Connell PA, McKenna GB (2005) Science 307:1760
22. Kajiyama T, Tanaka K, Ohki I, Ge SR, Yoon JS, Takahara A (1994) Macromolecules 27:7932
23. Tanaka K, Hashimoto K, Takahara A, Kajiyama T (2003) Langmuir 19:6573
24. Kajiyama T, Tanaka K, Takahara A (1997) Macromolecules 30:280
25. Hammerschmidt JA, Gladfelter WL, Haugstad G (1999) Macromolecules 32:3360
26. Tanaka K, Takahara A, Kajiyama T (2000) Macromolecules 33:7588
27. Akabori K, Tanaka K, Kajiyama T, Takahara A (2003) Macromolecules 36:4937
28. Mayes AM (1994) Macromolecules 27:3114
29. Tanaka K, Taura A, Ge SR, Takahara A, Kajiyama T (1996) Macromolecules 29:3040
30. Tanaka K, Takahara A, Kajiyama T (1997) Macromolecules 30:6626
31. Kajiyama T, Tanaka K, Satomi N, Takahara A (1998) Macromolecules 31:5150
32. Tanaka K, Jiang X, Nakamura K, Takahara A, Kajiyama T, Ishizone T, Hirao A, Nakahama S (1998) Macromolecules 31:5148
33. Satomi N, Takahara A, Kajiyama T (1999) Macromolecules 32:4474
34. Kajiyama T, Satomi N, Yokoe Y, Kawaguchi D, Tanaka K, Takahara A (2000) Macromol Symp 159:35
35. Ferry JD (1980) Viscoelastic properties of polymers, 3rd edn. Wiley, New York

36. Bueche F (1955) J Appl Phys 26:738
37. Takayanagi M (1965) In: Lee EH, Copley AL (eds) Proceedings of the 4th international congress on rheology, part 1, Brown University, Providence, 26–30 August 1963. Butterworth, London, pp 161–187
38. McCrum NG, Read BE, Williams G (1967) Anelastic and dielectric effects in polymeric solids. Dover, New York
39. Santangelo PG, Roland CM (1998) Macromolecules 31:4581
40. Kawaguchi D, Tanaka K, Kajiyama T, Takahara A, Tasaki S (2003) Macromolecules 36:1235
41. Kremer K, Grest GS (1990) J Chem Phys 92:5057
42. Morita H, Tanaka K, Kajiyama T, Nishi T, Doi M (2006) Macromolecules 39:6233
43. Krishnamoorti R, Vaia RA (eds) (2001) Polymer nanocomposites: synthesis, characterization, and modeling. In: ACS Symposium Series, vol 804. American Chemical Society, Washington
44. Ray SS, Bousmina M (2006) Polymer nanocomposites and their applications. American Scientific, Stevenson Ranch
45. Mai YW, Yu ZZ (2006) Polymer nanocomposites. CRC, Boca Raton
46. Shchipunov YA, Karpenko TY (2004) Langmuir 20:3882
47. Bordes P, Pollet E, Bourbigot S, Averous L (2008) Macromol Chem Phys 209:1473
48. Godovsky DY (2000) Adv Polym Sci 153:163
49. Tao SY, Yin JX, Li GT (2008) J Mater Chem 18:4872
50. Harmer MA, Farneth WE, Sun Q (1996) J Am Chem Soc 118:7708
51. Hasani-Sadrabadi MM, Emami SH, Moaddel H (2008) J Power Sources 183:551
52. Kim GM, Lee DH, Hoffmann B, Kressler J, Stoppelmann G (2001) Polymer 42:1095
53. Tien YI, Wei KH (2001) Macromolecules 34:9045
54. Tanaka K, Tsuchimura Y, Akabori K, Ito F, Nagamura T (2006) Appl Phys Lett 89:061916
55. Tanaka K, Tateishi Y, Okada Y, Nagamura T, Doi M, Morita H (2009) J Phys Chem B 113:4571
56. Matsuoka H (2001) Macromol Rapid Commun 22:51
57. Owens DK, Wendt RC (1969) J Appl Polym Sci 13:1741
58. Knoll W (1998) Annu Rev Phys Chem 49:569
59. Ekgasit S, Thammacharoen C, Knoll W (2004) Anal Chem 76:561
60. Tsuruta H, Fujii Y, Kai N, Kataoka H, Ishizone T, Doi M, Morita H, Tanaka K (2012) Macromolecules 45:4643.
61. Alcoutlabi M, McKenna GB (2005) J Phys Condens Matter 17:R461
62. Baschnagel J, Varnik F (2005) J Phys Condens Matter 17:R851
63. Forrest JA, Dalnoki-Veress K (2001) Adv Coll Interf Sci 94:167
64. Roth CB, Dutcher JR (2005) J Electroanal Chem 584:13
65. Tsui OKC, Russel TP (2008) Polymer thin films. Series in soft condensed matter. World Scientific, Singapore
66. Keddie JL, Jones RAL, Cory RA (1994) Faraday Discuss 98:219
67. van Zanten JH, Wallace WE, Wu WL (1996) Phys Rev E 53:R2053
68. Reiter G (1994) Macromolecules 27:3046
69. Tsui OKC, Russell TP, Hawker C (2001) Macromolecules 34:5535
70. Takayanagi M, Imada K, Kajiyama T (1967) J Polym Sci C 15:263
71. Yan S (2003) Macromolecules 36:339
72. Vogel H (1921) Phys Z 22:645
73. Fulcher GS (1925) J Am Ceram Soc 77:3701

Adv Polym Sci (2013) 252: 29–64
DOI: 10.1007/12_2012_174

# Probing Properties of Polymers in Thin Films Via Dewetting

**Günter Reiter**

**Abstract** In our quest to make functional devices smaller, the thickness of polymer films has reached values even smaller than the diameter of the unperturbed molecule. Many experimental studies have been devoted to the determination of the behavior of such thin films as a function of film thickness and temperature. However, despite enormous efforts over the last few decades, our understanding of the origin of some puzzling properties of such thin films is still not satisfactory and several peculiar observations remain rather mysterious. In this context, we explore the consequences of film preparation, i.e., the transition from a dilute polymer solution to the glassy state, with respect to the properties of polymers in thin films. This transition is likely to result in residual stresses arising from out-of-equilibrium chain conformations due to rapid solvent loss. Consequently, depending on thermal history and ageing time, such films exhibit significant changes even in the glassy state, which we can quantify by performing detailed studies of visco-elastic dewetting of thin polystyrene films on solid substrates. We explore relaxation times, residual stresses, and temporal changes to the stability of non-equilibrated thin films as they progress toward stable equilibrium behaviors. We present some tentative ideas on the relation between the observed atypical mechanical and relaxational behavior and the metastable states introduced by sample preparation.

**Keywords** Aging · Dewetting · Film preparation · Glass transition · Relaxation times · Residual stress · Thin polymer films

---

G. Reiter (✉)
Physikalisches Institut, Fakultät für Physik und Mathematik, Albert-Ludwigs-Universität Freiburg, Hermann-Herder-Strasse 3, 79104 Freiburg, Germany
e-mail: guenter.reiter@physik.uni-freiburg.de

## Contents

1 Introduction and Historical Remarks on Thin Polymer Films .............................. 30
2 Dewetting: Theoretical Considerations .................................................... 32
3 Dewetting Experiments Using a Newtonian Fluid ........................................ 38
4 Dewetting Experiments Using a Visco-Elastic Fluid: Polystyrene Films Slightly Above the Glass Transition Temperature ................................................. 43
5 Conclusions ...................................................................................... 59
References ........................................................................................... 60

## 1 Introduction and Historical Remarks on Thin Polymer Films

A large number of studies on thin polymer films revealed that various physical properties exhibited characteristics strongly deviating from their bulk behavior, with major implications for most technological applications based on such nanoscopic films. Diverse measurements have shown anomalous irreversible and reversible density changes after annealing below the bulk glass transition temperature ($T_g$) [1–9], unexpected instabilities of these films [1, 10–13], unusual ageing [14–21], deviations in mobility [22–28], deformed chain conformations [29–32], dewetting processes independent of molecular weight and much faster than suggested by bulk visco-elasticity [17–49], clear indications for residual stresses within these spin-coated thin polymer films [17, 39–54], a thickness-dependent but also history-dependent $T_g$ [55–85], and fast relaxation processes [17, 43, 48, 52–54]. A lowered softening temperature and decreased interfacial diffusion (employing the same samples) are examples of seemingly contradictory polymer dynamics in thin films. The cause of these deviations is a matter of ongoing debate [86–97].

Despite an extensive number of publications, it is becoming increasingly obvious that a clear understanding of thin polymer film properties has not yet been reached [87, 88, 91, 94–97]. The origin of (some of) these puzzling properties of thin polymer films is still not satisfactorily understood. At present, we are still missing a consistent understanding of the influence of film preparation and confinement on chain conformations. It is not yet clear how the visco-elastic behavior of thin polymer films is affected by the resulting chain conformations, in particular on approaching $T_g$. It is disputable whether or not the transition from a mostly dilute solution to a dry glassy state introduces a “conformational state” with its “own” properties [4, 94].

In the typical case of film preparation from solution, the solvent evaporates rapidly (within seconds) with a concomitant increase in polymer concentration until the film solidifies while there is still a significant amount of solvent present in the film. It is not certain whether the initially highly separated molecules in solution have enough time to interpenetrate sufficiently in order to establish an equilibrium state of entangled polymers. It is plausible that films prepared this way contain molecules having frozen-in conformations far from equilibrium, with a reduced degree of inter-chain overlap [43, 48]. Thus, one may ask if film preparation and the resulting non-equilibrium conformations of the polymers have an influence on measurements of visco-elastic properties, film stability, $T_g$, diffusion coefficient, etc. Sample preparation might also represent a possible cause for the anomalous behavior in glassy thin polymer films. In particular, fast evaporation of the solvent during the widely used process of spin-coating [98–101] could potentially produce samples that are far from equilibrium.

In trying to answer these questions it is certainly instructive to examine previous fundamental experimental works in which such thin films have been employed. In particular, we have to mention studies on polymer interdiffusion in which thin polymer films were used for testing theoretical concepts of polymer physics [102–106]. Spin-coating was typically used to prepare the films because this process presents an easy way of obtaining smooth film of precisely controllable thickness, even in the nanometer range. This is an essential criterion for investigating, for example, polymer diffusion across an interface between two films. While these experiments successfully supported the model of chain reptation [102–106], they also indicated some deviations that hinted, for example, at the enrichment of chain ends at surfaces [104, 106].

The possibility of being able to change easily and controllably the film thickness by varying the concentration of the solution used for spin-coating opened up a whole field of research on questions related to the chain-like nature of these macromolecules. In particular, at that time it was unclear (and partially still is!) if polymer properties like viscosity, chain conformation (as expressed for example by the radius of gyration), chain orientation, and interdiffusion rate, or mechanical properties and $T_g$ change once the thickness of the film decreases below the diameter of Gaussian polymer coils in bulk samples [1].

Unexpectedly, several of these experiments turned out to be “failures” in the sense that the films were not stable and were “destroyed” in the course of annealing above the glass transition temperature of the bulk system ($T_{g,bulk}$), and even below $T_{g,bulk}$ the films were unstable [1]. Stability, however, was required in order to allow for chain diffusion. Thin polymer films were often characterized by reflectometry techniques [1, 3, 102–106]. In the context of unstable films, reflectometry indicated a severe “roughening” of the films during annealing [1]. Consequently, it was necessary to investigate the origin of instabilities and to identify the relevant parameters in order to obtain stable films that do not roughen in time.

Two simple aspects helped to gain some insight into the origin of the roughening process. First, use of polished silicon wafers of high reflectance allowed detection of the homogeneity of the films by detecting the uniformity of the interference color. Second, inspection of thin films by optical microscopy made it clear that the instability of the film was related to a retraction of the film from the substrate, i.e., the film dewetted the substrate [107]. While it was soon found that dewetting could easily be avoided by using different substrates or by applying various cleaning procedures for the substrates, the dewetting phenomenon itself attracted significant attention [107–120]. It turned out that polymers are convenient fluids for dewetting studies because their negligible vapor pressure (polymers are nonvolatile) ensured mass conservation and their typically rather high viscosity assured that the dewetting process was slow enough to allow simple, time-resolved measurements. Moreover, the possibility of tuning the film thickness in the nanometer range enabled testing of the influence of short- and long-range intermolecular forces on film stability and dewetting dynamics [121–131]. In addition, as the process is highly sensitive to changes in interfacial properties and the properties of the dewetting fluid, dewetting can also be considered as a kind of rheological tool for the investigation of thin film properties [42, 43, 46].

The phenomenon of dewetting, i.e., the retraction of a fluid from a surface it was forced to cover, is frequently observed in our everyday life and is of central importance in many technological applications as well as in a variety of physical and biological systems [108, 132]. The wettability of a surface by a liquid is to a large extent characterized by interfacial tensions and thus by the contact angle. However, it is difficult to investigate kinetic effects like friction (energy dissipation) at an interface by contact angle measurements alone. The necessary velocity-dependent information is provided by spreading or dewetting experiments. Dewetting experiments are attractive because of their simplicity, sensitivity, and rapidity. Dewetting allows linking of static and kinetic molecular and interfacial properties (and variants of these properties) with macroscopically observable parameters like dewetting velocity and shape of the rim.

Despite its simplicity with respect to experimental observation, dewetting turned out to be extremely sensitive to even tiniest changes in the system under investigation. Thus, dewetting has proven to be a highly successful and time-efficient tool for obtaining time-resolved information on a molecular scale, allowing determination of interfacial properties and their changes in real time and in situ. Thus, dewetting experiments can provide information about relaxation and ageing processes of polymers in the film.

## 2 Dewetting: Theoretical Considerations

In general, if a substrate has a lower surface tension than a fluid, this fluid will not form a stable film when deposited onto such a substrate. Consequently, such an unstable fluid film will retract from this substrate by a dewetting process [108–111]. This process is the result of driving forces that try to remove the fluid and of dissipative processes that reflect the resistance of the fluid to its removal.

Here, we try to provide a elementary view on dewetting that nonetheless covers all essential features relevant in the context of thin polymer films. Thus, we neglect gravity (because the mass of the film is extremely small) and inertia (because we investigate cases where the dewetting velocity is comparatively small). We first concentrate on the simple case of a Newtonian fluid on a smooth and solid substrate. Accordingly, we assume that the fluid is completely characterized by its viscosity, i.e., we initially exclude visco-elastic, shear thinning or thickening, and temporal effects. Moreover, we assume that the substrate is inert and does not generate hysteretic behavior, i.e., we exclude contact line pinning and chemical reactions at the substrate.

The displacement of the three-phase contact line, where the fluid film meets the substrate and the surrounding medium (in most cases this is air), is governed by the balance of driving and resisting forces. For a Newtonian fluid, capillarity represents the main driving force for dewetting. It is related to an imbalance between the three interfacial tensions [$\gamma_L$ (liquid–air), $\gamma_{LS}$ (liquid–substrate), and $\gamma_S$ (substrate–air)] that meet at the contact line and are responsible for a dynamic contact angle $\theta_{dyn}$. In contrast, when all interfacial tensions are balanced we obtain the equilibrium contact angle $\theta_{equ}$ (which represents the absolute minimum in free energy of the system) and the contact line will be at rest [133]. Dewetting is thus driven by a capillary force (uncompensated Young force, $F_{Young}$) that arises from the difference between $\theta_{dyn}$ and $\theta_{equ}$. In fact, on ideal surfaces, whenever the contact angle deviates from $\theta_{equ}$ the contact line will show the tendency to move in order to try to (re-)establish equilibrium. In general, the stronger $\theta_{dyn}$ deviates from $\theta_{equ}$, the faster will be the movement of the contact line. Thus, for $\theta_{dyn} \neq \theta_{equ}$, a net force $F_{Young}$ (per unit length of the contact line) pushes the contact line:

$$F_{Young} = -\gamma_S + \gamma_{LS} + \gamma_L \cdot \cos\,\theta_{dyn}. \tag{1}$$

Using the relation for the equilibrium contact angle, $\gamma_S = \gamma_{LS} + \gamma_L \cdot \cos\,\theta_{equ}$, we obtain $F_{Young} = \gamma_L(\cos\,\theta_{dyn} - \cos\,\theta_{equ})$.

For small contact angles, the cos term can be approximated by the first term of its series expansion, i.e., $\cos\,\theta \approx 1 - (1/2)\theta^2$. This then leads to:

$$F_{Young} = (1/2) \cdot \gamma_L(\theta_{equ}^2 - \theta_{dyn}^2). \tag{2}$$

Removing the fluid from the substrate involves the relative movement of molecules past each other. This gives rise to viscous dissipation within the fluid. The motion of fluid molecules at the substrate causes frictional losses. Furthermore, depending on fluid–substrate interactions and properties of substrate and fluid, these frictional losses may be localized in a region close to the contact line (no slip boundary condition). For strong cohesion of the fluid, as is the case for entangled polymers, one may encounter slippage of the fluid on top of the substrate and thus frictional losses originate from the whole region moving (slipping) past the substrate. As a general feature, it is important to note that interfacial friction is responsible for the formation of a rim, i.e., the accumulation of the removed fluid in a region close to the contact line. Without such friction or in cases where interfacial friction is small compared to viscous dissipation within the fluid, the removed fluid will be distributed within the remaining surrounding film, causing an increase in mean film thickness but no formation of a rim.

The no-slip condition at the substrate reflects the fact that liquid molecules at a solid substrate experience (significant) interactions responsible for adhesion. In contrast to liquid molecules in contact with other liquid molecules, they do not move easily on this substrate. As a consequence, the velocity of these molecules is approximately zero (hence, no-slip boundary condition). However, applying this boundary condition strictly would not allow for any displacement of a liquid on a

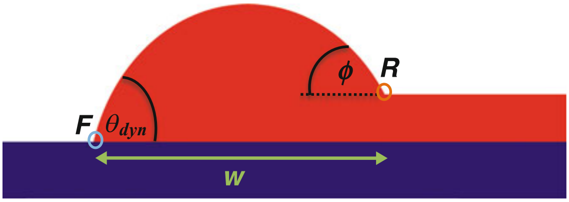

**Fig. 1** Rim formation in the course of dewetting of a thin liquid film. At the front position $F$ of the rim, the contact angle assumes its dynamic value $\theta_{\text{dyn}}$ and at the rear position $R$ it takes the value $\phi$. The width of the rim is given by $w$

solid substrate. Thus, to account for the experimental fact that contact lines can and do move, various approximations, partially based on molecular mechanisms, have been proposed (see e.g. [134]). In general, a cut-off length, typically as small as the size of the molecules, has to be introduced [132, 135].

For small contact angles, the flow pattern close to the contact line (the wedge region) can be approximated by the so-called lubrication approximation, which compares the flow in the wedge with flow in a thin film. The velocity of fluid molecules is only determined by their distance vertical to the substrate; the molecules move preferentially in the direction parallel to the substrate and less in the direction away from the substrate.

If the viscous forces are significantly smaller than the surface tension (as expressed by a capillary number $Ca$ much less than 1: $Ca = U{\cdot}\eta/\gamma_L$, with $U$ being the velocity of the contact line and $\eta$ the viscosity of the liquid), the shape of a liquid drop can be reasonably well approximated by a spherical cap. Laplace pressure $P_{\text{L}}$ (where $P_{\text{L}} = 2{\cdot}\gamma_{\text{L}}{\cdot}K$ and the curvature $K = 1/R$ for a spherical cap of radius $R$ and thus $P_{\text{L}} = 2{\cdot}\gamma_{\text{L}}/R$) will be able to assure the same curvature everywhere (with the possible exception of the region very close to the contact line, where long-range molecular interactions, e.g., van der Waals forces, may become important).

The liquid removed from the dried region (e.g., a hole in the fluid film) is collected in a ridge (the "rim") (see Fig. 1). The shape of this rim may be described approximately as a portion of a cylinder that is characterized by two contact angles $\theta_{\text{dyn}}$ and $\phi$ (see Fig. 1).

In the case of a no-slip boundary condition, the movement of the contact line (position $F$) with dewetting velocity $U$ results from a balance between driving force and viscous dissipation in the wedge close to the moving contact line. Integration over the whole moving part of the fluid from its lowest thickness at the contact line having a minimum thickness of $h_{\text{min}}$ to its thickest part with the maximum thickness of $h_{\text{max}}$ yields the total viscous force $F_{\text{visc}}$ per unit length of the contact line during dewetting [132, 134]:

$$F_{\text{visc}} = 3\eta/\theta_{\text{dyn}} \cdot U \cdot \ln(h_{\text{max}}/h_{\text{min}}), \tag{3}$$

$$F_{\text{Young}} = (1/2) \cdot \gamma_{\text{L}}(\theta^2_{\text{dyn}} - \theta^2_{\text{equ}}) = 3\eta/\theta_{\text{dyn}} \cdot U \cdot \ln(h_{\text{max}}/h_{\text{min}}) = F_{\text{visc}}. \tag{4}$$

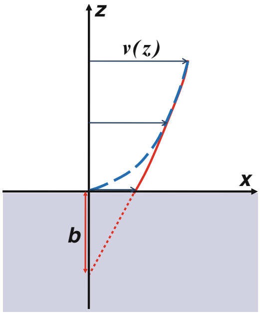

**Fig. 2** Velocity profile of liquid flow within a thin film (lubrication approximation). For the no-slip boundary condition (*dashed line*), the velocity at the substrate ($z = 0$) is zero. In the case of slippage (*solid line*), the liquid velocity is not zero at the substrate surface and only extrapolates to zero at a distance $b$ (slippage length) within the substrate

For dewetted distances much larger than the width of the rim, both ends of the rim (denoted by $F$ and $R$ in Fig. 1) move at approximately the same velocity. Moreover, at the position $R$ the equilibrium value of the contact angle is zero (rim in contact with the film of the same liquid) and thus yields:

$$(1/2) \cdot \gamma_L \cdot \theta_{\text{dyn}}^2 = 3\eta/\theta_{\text{dyn}} \cdot U \cdot \ln(h_{\max}/h_{\min}). \tag{5}$$

Here, $h_{\max}$ and $h_{\min}$ are evaluated at the position $R$.

Assuming that the Laplace pressure is the same everywhere within the rim (i.e., the same curvature is assumed to exist everywhere in the rim) requires that $\theta_{\text{dyn}} \approx \phi$. For thin films in the nanometer range and a size of the rim in the range of micrometers, the logarithmic factors at positions $R$ and $F$ are similar. Consequently, a highly useful relation is obtained between dynamic and equilibrium contact angles for the case of viscous dewetting (with $\theta_{\text{dyn}} \approx \phi$): [136]:

$$\gamma_L(\theta_{\text{dyn}}^2 - \theta_{\text{equ}}^2) \cdot \theta_{\text{dyn}} = \gamma_L \phi^3, \tag{6}$$

$$\theta_{\text{dyn}} = \theta_{\text{equ}}/\sqrt{2}. \tag{7}$$

This yields a constant dewetting velocity $U$ of:

$$U \sim \gamma_L/\eta \cdot \theta_{\text{equ}}^3 \sim U^* \cdot \theta_{\text{equ}}^3. \tag{8}$$

Basically the same procedure can be applied to the case where the liquid is slipping on the substrate by introducing an extrapolation length (slippage length) $b$ within the substrate (see Fig. 2) where the flow velocity would be zero, i.e., the non-slip boundary would be reached at a virtual interface inside the solid. Thus, one expects $h_{\min} \approx b$ [132]. Slippage is particularly relevant in the case of entangled

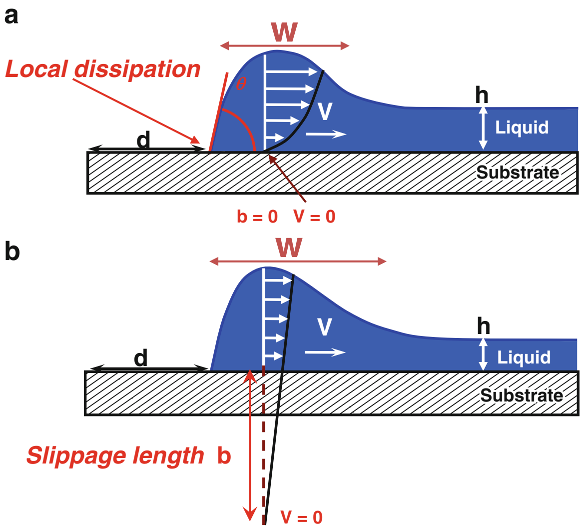

**Fig. 3** Late stages of dewetting of a Newtonian fluid on a substrate with (**a**) non-slip and (**b**) slip boundary conditions; *V* velocity, *W* width of rim, *h* film thickness, *d* dewetted distance

polymer melts spreading or dewetting on a smooth surface [137–153]. A large number of experimental studies on slippage have been recently reviewed [154, 155].

In the case of slippage, the frictional dissipation $F_{\text{diss}}$ (force per unit surface) at the interface between the liquid on the substrate is characterized by a friction coefficient $\zeta$, and is proportional to the velocity $V_{\text{slip}}$ with which the whole rim of width $w$ is moving past the substrate: $F_{\text{diss}} = \zeta{\cdot}V_{\text{slip}}$. As has been shown by de Gennes, $\zeta$ is given by the ratio of fluid viscosity over slippage length, i.e., $\zeta = \eta/b$ [42, 46, 108]. The theoretical prediction for the length $b$ in the steady-state flow of a polymer melt is $a \cdot (N^3/N_e^2)$, where $a$ is the monomer size, $N$ is the polymerization index, and $N_e$ the number of segments between entanglements [132, 137]. For a slippage length $b$ larger than the film thickness $h_0$, the velocity of the dewetting fluid does not vary significantly in the direction normal to the substrate. Thus, the fluid roughly flows like a plug. In such a case, energy is dissipated almost exclusively at the liquid–substrate interface where the highest velocity gradient exists. Schematic views on the differences of the no-slip or slip boundary condition in the context of dewetting are given in Fig. 3. Thus, the frictional loss within the rim (force per unit length of the contact line) is:

$$F_{\text{int}} \sim \zeta \cdot V_{\text{slip}} \cdot w \sim \eta/b \cdot V_{\text{slip}} \cdot w. \tag{9}$$

Consequently, for the opening of a hole of radius $r$ in a film of thickness $h_0$, force balance $[(1/2) \cdot \gamma_{\text{L}} \cdot \theta_{\text{dyn}}^2 = \eta/b \cdot V_{\text{slip}} \cdot w]$ and mass conservation $(r^2 h_0 \sim 2rw^2\theta_{\text{dyn}})$ lead to $(V_{\text{slip}} = \mathrm{d}r/\mathrm{d}t)$:

$$\mathrm{d}r/\mathrm{d}t \cdot (r \cdot h_0)^{1/2} \sim (\gamma_{\text{L}}/\eta) \cdot b \cdot \theta_{\text{dyn}}^2 \tag{9a}$$

or

$$r^{3/2} \sim (\gamma_L/\eta)\theta_{\mathrm{dyn}}^2(b/h_0^{1/2})t \tag{9b}$$

and thus the dewetting velocity decreases in time $V_{\mathrm{slip}} \sim t^{-1/3}$.

Seminal work has been performed by Brochard-Wyart and colleagues [110–113, 144, 145] on dewetting of thin polymer films with thicknesses smaller than the slip length $b$ (high-slip regime). Assuming a Newtonian fluid, they have determined a characteristic length $\Delta_0 = (h_0 \cdot b)^{1/2} = (h_0 \cdot \eta/\zeta)^{1/2}$, which is related to the transition between an initially viscous dissipation-dominated regime due to fluid flow in a flat film (the amount of fluid in motion is small and fluid motion at the interface concerns only a small distance less than $\Delta_0$ away from the contact line) and a subsequent regime where dissipation due to friction at the film–substrate interface controls the dewetting velocity [42, 46, 145]. Consequently, one obtains three stages of hole opening [110–113, 144, 145].

For small holes ($R < \Delta_0$), viscous dissipation within the film due to radial and ortho-radial deformations dominate. This leads to an exponential growth of the hole, a consequence of a continuously increasing length of the three-phase contact line, i.e., the perimeter of the hole. During this regime, no rim is formed. For $R > \Delta_0$ interfacial friction dominates. At this later stage, the relative increase in hole perimeter is small and so the increase in driving force is smaller than the increase in frictional force. Thus, a rim of width $\Delta_0$ starts to build up.

For dewetting from a straight edge (edge geometry), no initial exponential growth regime exists because the length of the three phase contact line always stays constant. Therefore, right from the onset of dewetting a rim of width $\Delta_0$ builds up, accompanied by an initially constant dewetting velocity $V$. Once the rim is fully developed ("mature") at $R \sim b$, the dewetting velocity starts to decrease ($V \sim t^{-1/3}$) because now the width of the rim (and thus interfacial friction) increases with time [42, 46, 145].

During the regime of building up of a rim, the driving capillary force at the contact line, expressed by the spreading parameter $|S|$, is balanced by the viscous normal stress $\sigma$ integrated over the total height $H$ of the film at the front of the rim moving a dewetted distance $d(t)$:

$$|S| = -\sigma d(t)H \tag{10}$$

Rim build-up occurs at times $t$ shorter than the relaxation time of the fluid in the film: $t < \tau = h_0 \cdot \eta/|S|$ [42, 46, 145].

Far away from the dewetting region, the fluid velocity decays to zero. At short times [i.e., at the onset of dewetting and rim build-up, when $h(x,t)$ is still close to $h_0$] these equations yield the velocity profile within the film as [42, 46]:

$$v(x,t) = V_0 \exp[-(x-d)/\sqrt{2\Delta_0}]. \tag{11}$$

It should be noted that a constant dewetting velocity for Newtonian liquids can only be observed as long as the assumption of a non-slip boundary conditions is satisfied, i.e., most dissipation takes place in the liquid wedge close to the contact line. Consequently, dissipation is independent of the actual size of the rim and will not change in the course of dewetting. However, in the case of slippage, a significant velocity gradient exists at the film substrate interface over the whole width of the rim. In this case, interfacial friction occurs over the whole moving interface, which is proportional to the width of the moving rim. Accordingly, as the size of the rim increases in course of dewetting, dissipation increases also. The driving capillary force, however, is constant and, consequently, the dewetting velocity decreases with time.

We will present a few examples, which demonstrate that the balance of forces enables us to extract in a highly quantitative manner detailed information on molecular and interfacial properties of thin polymer films from relatively simple dewetting experiments.

## 3 Dewetting Experiments Using a Newtonian Fluid

As dewetting reflects the balance of driving forces and energy dissipation, and thus is the consequence of intrinsic properties controlled by molecular interactions, this kinetic process is at all stages self-adjusting to any variations in experimental conditions, in particular at the solid–fluid interface. Thus, in following the displacement of a contact line in time we are able to determine velocity-dependent (kinetic) molecular interfacial properties at a polymer–polymer interface, such as friction (energy dissipation). As an example to demonstrate the capacity of such experiments, we use these kinetic aspects of dewetting in real time to investigate the properties of a polymer melt slipping on a layer of chemically identical molecules, end-grafted to a silicon substrate (i.e., a polymer brush). The entropy difference between grafted and free polymers results in autophobic behavior of the brush [146, 147, 156–161].

We are interested in the following questions: How does a polymer move or flow on its own monolayer, or more generally, how do macromolecules slide past each other? What are the consequences of the autophobic behavior between grafted and free polymers for dewetting? What is the value of the friction coefficient at such polymer–polymer interfaces? After a brief description of our experimental conditions, we present the experimental results, which are discussed in light of the theory described above. Finally, we show what we can learn about molecular parameters controlling interfacial properties.

Polydimethylsiloxane (PDMS) films represent a well-investigated example of dewetting of a Newtonian fluid. Here, we present experimental results on the dewetting behavior of thin films on smooth non-wettable silicon substrates that were coated with a layer of end-grafted PDMS molecules (a polymer brush) [146–149], because at high grafting densities an autophobic behavior was generated [146, 147], i.e., the free molecules dewetted the grafted layer.

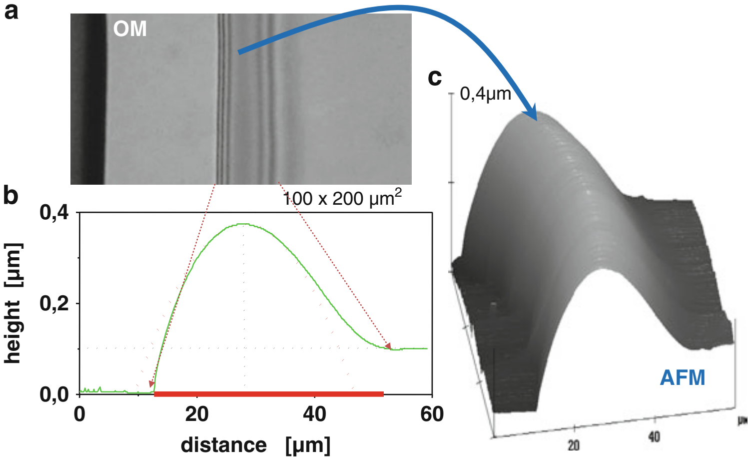

**Fig. 4** (**a**) Optical micrograph (top view) of dewetting. (**b**) Cross-section and (**c**) 3D view of the shape of the rim as measured by AFM

The thickness $h_0$ of the PDMS films on top of the PDMS brush, as measured by ellipsometry, was varied in the range of 30–150 nm. All films were obtained by spin-coating dilute heptane solutions directly onto the coated substrates. As indicated in Fig. 4, isothermal dewetting of the thin polymer films, i.e., the retraction of a contact line, was followed in real time ($t$) by optical microscopy. The morphology of the rim was also investigated by atomic force microscopy (AFM). More details on sample preparation and dewetting measurements can be found in [146, 147].

An example of systematic analysis of an autophobic dewetting experiment is given in Fig. 5. It should be emphasized that it is possible to simultaneously measure the dewetted distance ($d$) and the width ($w$) of the rim by tracking the front ($F$) and rear ($R$) positions of the dewetting rim in time. As can be seen in Fig. 5, both $d$ and $w$ did not increase linearly in time, i.e., the dewetting velocity decreased in the course of dewetting. Fitting the data points for $d(t)$ to a power-law gave an exponent of $0.65 \pm 0.05$, which is consistent with the theoretically expected [112, 139] value of 2/3 for slippage of the liquid on the substrate [see Eq. (9) and the related transformations]. A constant dewetting velocity, on the other hand, would have indicated a non-slipping behavior. The slowing down of the dewetting process with time is thus a distinct feature that indicates slippage.

In addition to this temporal evolution of the dewetting velocity, slippage also invokes a characteristic dependence on film thickness. In the non-slip case, the dewetting velocity is independent of film thickness, but the rim width, for a given dewetted distance, is larger for thicker films. Thus, interfacial friction increases with film thickness and dewetting proceeds more slowly in thicker film. This is shown in Fig. 6.

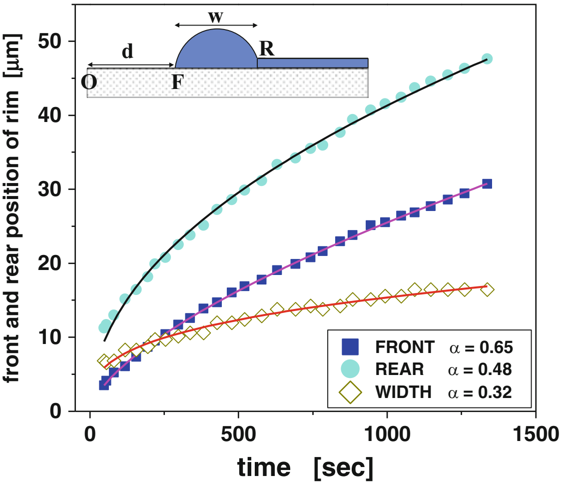

**Fig. 5** Typical result for dewetting of a PDMS film (92 nm, $M_w = 308$ kg/mol) on top of a densely grafted brush of end-functionalized PDMS molecules (6.3 nm, $M_w = 8.8$ kg/mol). The temperature was 50°C. Dewetted distance $d$ and the width $w$ of the rim are represented in the *inset*. The *lines* are best fits of $y = A(t - t_o)^\alpha$ to the data, where $y$ stands for $d$ or $w$. $A$ is a constant prefactor, and $t_0$ is a time offset. $\alpha$ was found to be 0.65 for $d$ and 0.32 for $w$ [146, 147]

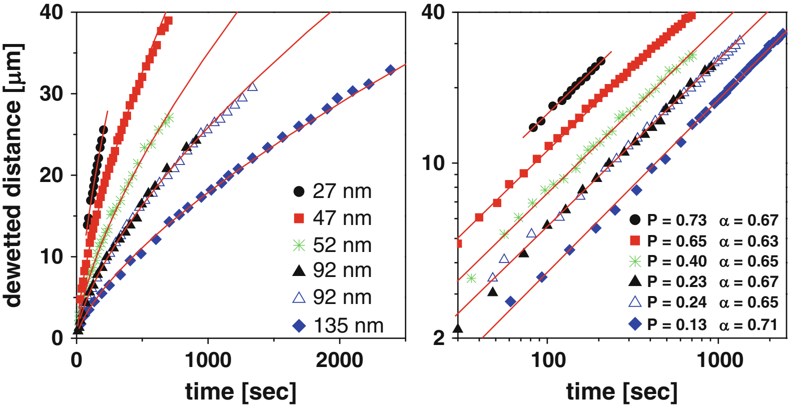

**Fig. 6** Typical result for dewetting of a PDMS film [$M_w = 308$ kg/mol, $\eta(25°C) = 1{,}000$ Pa s] on top of a densely grafted layer of end-functionalized PDMS molecules (6.3 nm, $M_w = 8.8$ kg/mol) for different thicknesses, as indicated. *Left*: linear scale clearly shows the decrease in dewetting velocity with film thickness. *Right*: logarithmic scale demonstrates that all samples follow the same power law. The *solid lines* are best fits to the data using the equation $d \sim P(t - t_o)^\alpha$. As indicated, we obtained $\alpha = 0.65 \pm 0.05$ for all measurements at low temperatures (here, 50°C). The prefactors $P$, which depend on parameters like contact angle and slippage length, decreased with film thickness. Note that two independent measurements using the same sample gave the same results (*solid* and *open triangles*). Note further that films of similar thickness (47 and 52 nm) showed rather different prefactors $P$

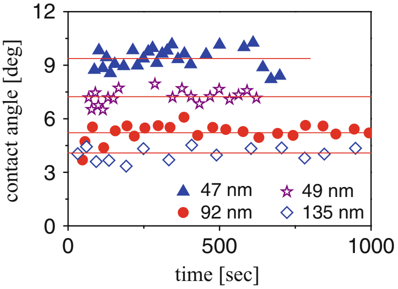

**Fig. 7** Examples showing the temporal evolution of contact angle in the course of dewetting, as derived from mass conservation for the system described in Fig. 6 (for the film thicknesses indicated)

Based on mass conservation, measuring $d$ and $w$ for nonvolatile liquids like polymers as a function of time $t$ allows determination of the value of the contact angle $\theta$ and even tracking of it in time and determination of possible variations of $\theta$ in time, without any fitting. For slipping films we get:

$$\theta(t) = d(t)h(t)/C \cdot w^2(t) \tag{12}$$

The constant $C$, accounting for the shape of the rim, has been found [112] to be 0.1 for slipping films. Typical results for autophobic dewetting of PDMS films are shown in Fig. 7. The values of $\theta$ differed between samples but were found to be constant in time, confirming the stability and homogeneity of the investigated dewetting system in the course of the experiments.

Similarly, we also can obtain the value of the slippage length $b$ and its temporal evolution:

$$b(t_\mathrm{i}) = 3\eta \cdot V(t_\mathrm{i})w(t_\mathrm{i})/(\gamma_\mathrm{L}\theta^2(t_\mathrm{i})). \tag{13}$$

Note that this approach for measuring the contact angle and slippage length (see Fig. 8) also allows detection of changes in the adsorbed or grafted PDMS layer during the experiment (see [147]).

Interestingly, these results indicate that for the slow dewetting velocities of these experiments, $b$ neither depended on dewetting velocity nor on film thickness. According to theory [see [112] and Eq. (9)], the viscous force $F_\mathrm{V}$ increases with $w$. Taking into account the balance of forces ($F_\mathrm{D} = F_\mathrm{V}$) and knowing that in the course of the dewetting experiments described in Figs. 5 and 6 the driving force characterized by $\theta$ (see Fig. 7) is constant, we anticipate that the dewetting velocity $V$ decreases with the increase in $w$. This is indeed confirmed in Fig. 9, which proves that dissipation increases linearly with $w$. Such a relation between $V$ and $w$ implies that the whole rim slips.

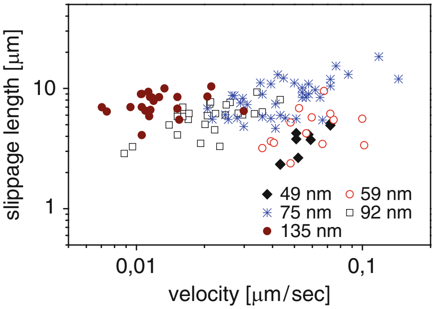

**Fig. 8** Slippage length as determined from Eq. (13) as a function of dewetting velocity on double-logarithmic scales

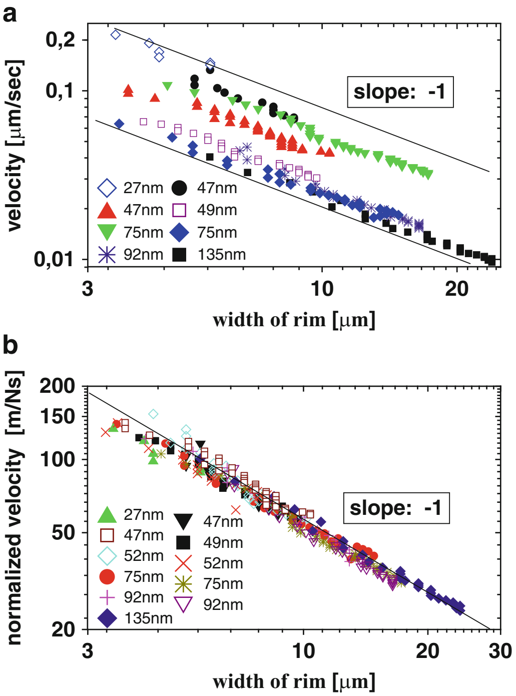

**Fig. 9** (**a**) Dewetting velocity and (**b**) normalized velocity [multiplied by $b/(\gamma_L \cdot \theta^2)$] as a function of the width of the rim for various film thicknesses, as indicated

Moreover, when normalizing the velocity by the capillary driving force (proportional to $\theta^2$) and the slippage length $b$ (giving a parameter in units of meter per Newton second) allowed us to obtain a master curve (Fig. 9b) as expected from Eq. (9). We note that both $\theta$ and $b$ were found to be constant in time (see Figs. 7 and 8). We did not observe any systematic dependence of $\theta$ and $b$ on film thickness $h_0$. This corroborates that the theoretical description of our observations takes all relevant parameters into account.

Besides viscosity $\eta$, the slippage length $b$ mainly reflects the interfacial friction coefficient $\zeta$ (per area of one monomer): $b = \eta/\zeta$ [137]. Thus, for the observed values of $b \sim 10$ μm and the viscosity of the dewetting PDMS film ($\eta = 1{,}000$ Pa s we can deduce a value of $\zeta \sim 10^8$ Pa s/m. Comparing this value to the monomeric friction coefficient [141] $\zeta_0 = 3.7 \times 10^7$ Pa s/m indicates that only a few monomers at the interface contributed to friction ($\zeta \sim 3\zeta_0$). This implies that the free polymers penetrated only little into the layer of densely grafted, chemically identical polymers. In conclusion, this example shows that dewetting experiments are capable of relating friction at the brush–melt interface to the degree of interpenetration between grafted and free polymer chains.

## 4 Dewetting Experiments Using a Visco-Elastic Fluid: Polystyrene Films Slightly Above the Glass Transition Temperature

It is important to realize that in systems where a film is forced onto a substrate that it does not want to wet, the capillary force acts independently of the state of the liquid. Thus, even if the liquid is vitrified, a force is pushing the glassy film. Dewetting, however, may be stopped, at least on experimentally accessible time scales, because this acting force may be too weak to push a vitreous solid or a highly visco-elastic material. We will present some results, again obtained by using optical microscopy or AFM, showing how the dewetting process is affected by the visco-elastic properties of the film. In other words, we want to show what kind of information dewetting studies can provide about the rheological properties of thin polymer films.

It is well known that capillary forces resulting from intermolecular interactions are capable of retracting a purely liquid film from a solid surface [110]. It is, however, less frequent that one encounters a similar dewetting phenomenon for highly visco-elastic films where, on the time scale of the experiment, the material cannot flow like a liquid. Experiments on thin polystyrene (PS) films at temperatures not too far above $T_g$ fall into this category. [107, 114–120] Under such conditions, the polymer can by no means be treated as a Newtonian liquid. Thus, interpretation of dewetting results has to also account for the highly elastic properties of the polymer film. However, it is not clear a priori if capillary forces alone, which are of the order of 10 mN/m, are strong enough to provoke dewetting in highly elastic films.

The elasticity of the film also affects characteristic features of dewetting like the shape of the rim or the temporal evolution of the hole diameter. In addition, in the course of time, the behavior of the PS film will switch from highly elastic at short

**Fig. 10** Sample geometry indicating a PS film (glass transition around 105°C) on an adsorbed or grafted liquid-like PDMS layer supported by a silicon substrate

times to purely viscous at long times, which also becomes evident in the dewetting parameters and their temporal evolution. Thus, in order to shed some light onto the phenomenon of dewetting of highly elastic films, we followed the process of hole growth in PS films in detail, starting from the very early stages. To accentuate the possible influence of driving forces, and to reduce simultaneously the resistance resulting from interfacial friction, we chose highly non-wettable substrates, as achieved by using PDMS-coated Si wafers (Fig. 10). This PDMS coating "screened" all heterogeneities of the solid substrates and thus represented an ideally homogeneous surface of low surface energy and low interfacial friction for the moving PS film.

First, we investigated dewetting of PS films thinner than 20 nm using AFM at room temperature after annealing the samples ex situ in a closed hot stage purged with nitrogen. Only for thicker films, where holes became visible under an optical microscope, were real time investigations performed in situ.

In analogy to previous results [107, 114–120], all PS films on such substrates turned out to be metastable and ruptured upon annealing at elevated temperatures. The number density of holes increased rapidly with decreasing film thickness [107]. We concentrated on the shape of these holes and its evolution with time at temperatures above about 103°C. Complementary experiments indicated, however, that hole formation was also possible at lower temperatures [162]. As discussed previously [4, 17], hole formation may also reflect the relaxation of internal tensions induced during sample preparation and caused by confining the polymers to films thinner than the size of the unperturbed coil.

Figure 11 presents typical AFM results for the early stages of hole formation obtained from the thinnest films investigated. Due to the many holes of similar size formed within the small area detected by AFM, these films allowed us to conclude that most holes were formed within a narrow time interval at the very beginning. At such early stages, the material displaced from the dewetted areas was not collected in visible rims around these areas but was distributed evenly within the whole film in between the holes. Thus, imposing mass conservation, the film thickness between the holes had to increase. A comparison between the thicknesses before annealing as measured by ellipsometry and the depth of the holes measured by AFM is shown in Fig. 12.

For these two films from PS of very different molecular weights (125 kg/mol and 3,900 kg/mol) we found approximately the same dewetting behavior. This demonstrates that at these early stages the viscosity of the polymer, which varied

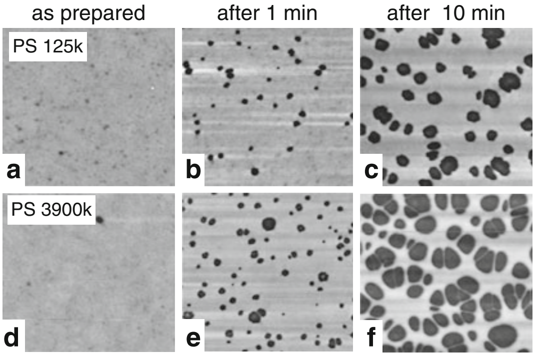

**Fig. 11** Typical atomic force micrographs showing the consequences of annealing thin PS films on PDMS-coated Si wafers at a temperature close to the glass transition of PS. Rimless holes of some 100 nm in diameter are formed. Two different molecular weights are compared. *First row*: 16 nm PS with $M_w$ of 125 kg/mol, *second row*: 13 nm PS with $M_w$ of 3,900 kg/mol. (**a**, **d**) show the as-prepared samples. (**b**, **e**) and (**c**, **f**) were measured after annealing for 1 and 10 min at 105°C, respectively. The size of the images is 3 μm × 3 μm

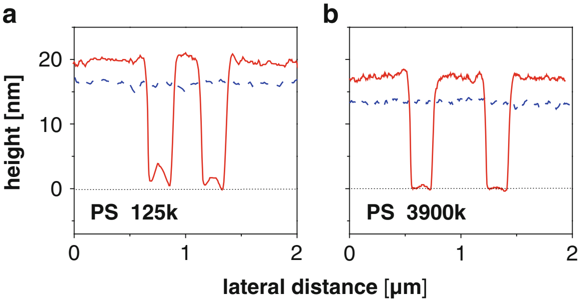

**Fig. 12** (**a**, **b**) Cross-sections of the PS films shown in Fig. 11: *dashed line* as-prepared, *solid line* after annealing for 10 min at 105°C

by several orders of magnitude, did not play a determining role in the rate of hole growth. This result seems to indicate that the plateau shear modulus of PS, which does not depend significantly on chain length, may be the essential control parameter for the growth rate.

Figure 13 shows a quantitative comparison of our results for the early stages for hole growth. Almost all tiny holes (with a diameter $D$ of about 70 nm) were formed after annealing for only 1 min. This implies an average opening velocity ($\mathrm{d}D/\mathrm{d}t$) of these holes of about 70 nm/min and an average shear rate $\mathrm{d}\gamma/\mathrm{d}t = 1/D \cdot \mathrm{d}D/\mathrm{d}t$ of about 0.7 $\mathrm{min}^{-1}$. Comparing $\mathrm{d}\gamma/\mathrm{d}t$ with the reptation time ($\tau_{\mathrm{rep}}$) of PS close to $T_g$ (for the conditions of the experiments shown in Fig. 11, $\tau_{\mathrm{rep}}$ is much larger than one year [104]) demonstrates that on the time scale of the experiments we cannot expect

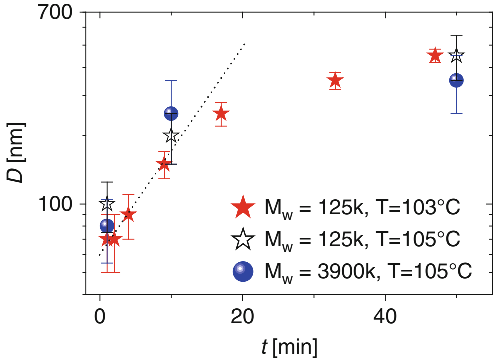

**Fig. 13** Hole diameter $D$ as a function of annealing time $t$ for PS films of Fig. 11 annealed at 103°C and 105°C. Note that the molecular weight does not seem to have an influence on the growth rate. The *dotted line* represents an exponential fit to the early stages, yielding $D$ (nm) = **67** (nm) exp[$t$/12.6 (min)]

viscous flow of the polymer. This makes it clear that the capillary driving force cannot be balanced by viscous dissipation only. Other resisting forces have to be invoked. Potential candidates are elastic or plastic deformation of the quasi-solid PS film and friction at the PS–PDMS interface.

As the annealing time increased, $D$ became progressively larger. The data shown in Fig. 13 allowed the growth of the hole diameter at the earliest stages to be fitted to an exponential function, similar to the theoretical expectation [144], for the onset of hole growth when no rim is formed. However, the many holes per unit area started to coalesce as their diameters became larger than about 200 nm, which had an influence on the growth rates. Complementary measurements on thicker films, which contained fewer holes per unit area [107], showed that this initial (most likely) exponential growth regime passed over to a slower behavior at hole diameters below 1 μm, coinciding with the appearance of a rim.

During the subsequent stages of visco-elastic dewetting, a rim developed and its shape changed significantly over time. Initially, the energy supplied by the driving forces was mainly dissipated within the volume of the film in the vicinity of the hole (via deformations in the radial and ortho-radial). The removed material (related to the dewetted distance $d$) was redistributed within the film over a certain distance $\Delta_0$, which is characterized by film thickness $h_0$ and frictional properties [42, 46, 144]:

$$d \ll \Delta_0 \sim (h_0\eta/\zeta)^{1/2} \tag{14}$$

with $\zeta$ being the friction coefficient at the interface and $\eta$ the viscosity of the film. Under such conditions, no rim was formed next to the circular dewetted zone.

However, as the radius of the hole becomes larger than $\Delta_0$, this contribution to dissipation becomes smaller compared to friction at the substrate–film interface. As a consequence of such friction, the velocity is damped over the distance $\Delta_0$ within

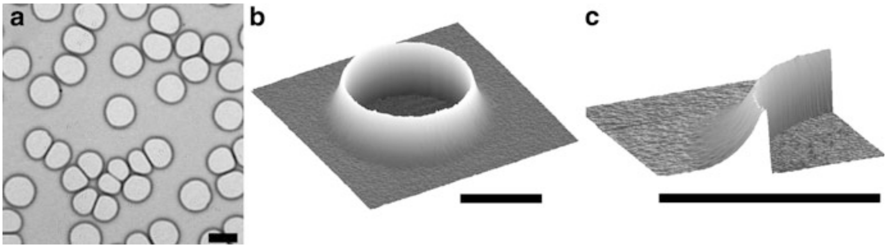

**Fig. 14** Typical examples of holes and the corresponding rim formed in a 24-nm thick PS film. This film is thick enough for holes to be separated by several micrometers on average. (**a**) Optical micrograph after annealing for 80 min at 120°C. AFM images (**b**) and (**c**) focus on the asymmetric shape of the rim. Scale bars: 5 μm

the film. This damping results in the appearance of a highly asymmetric rim (Fig. 14), with a steep side reaching a height $H$ next to the three-phase contact line and an approximately exponential decay on the other side, with a decay length $\varDelta_0$ [17, 42, 44].

The highly asymmetric shape of the rim suggests that the polymer does not flow like a liquid. For a viscous fluid we would expect that equilibration of the Laplace pressure (which is proportional to curvature) within the rim is fast, i.e., fast with respect to the shortest possible experimental time scale. This would lead to a more symmetric shape. In our experiments, the asymmetric shape of the rim represents a characteristic feature of dewetting of high molecular weight visco-elastic fluids at temperatures close to $T_g$ [17, 37, 38, 41–48]. Typical examples showing the evolution of the shape of the rim are given in Fig. 15.

The change in shape of the rim with time can be followed by taking cross-sections through holes after different annealing times (Fig. 16). At the very beginning of hole formation (for hole diameters less than about 1 μm), no rim could be detected (see the smallest hole diameter in Fig. 16). As the holes became larger, the build-up of the highly asymmetric rim could be followed. Interestingly, the maximum height of the rim increased almost linearly with time.

The decay on the rear side can be fitted to an exponential function $y = A \exp[(x - x_0)/\varDelta_0] + y_0$ with amplitude $A$ and offsets $x_0$ and $y_0$. As expected by theory [42, 44, 46, 47], the characteristic decay length $\varDelta_0$ did not vary with annealing time. Fits to the profiles shown in Fig. 16 all resulted in $\varDelta_0 \sim 0.5$ μm. We note, however, that $\varDelta_0$ could vary between 0.3 μm and several micrometers for samples with slightly varying thicknesses of the PDMS coating. The hole opening velocity was faster for larger $\varDelta_0$.

As in dewetting experiments with simple (Newtonian) fluids, one can also measure the width $w$ of the rim. To do this, the exponential decay is truncated when the height of the rim (measured from the substrate level) has decayed to a value about 1.1 $h_0$. Then, according to theory [42, 44, 46, 47], $w = \sqrt{2}\,\varDelta_0 \ln(10t/\tau)$, with $\tau$ being a characteristic relaxation time of the polymer. As can be seen in

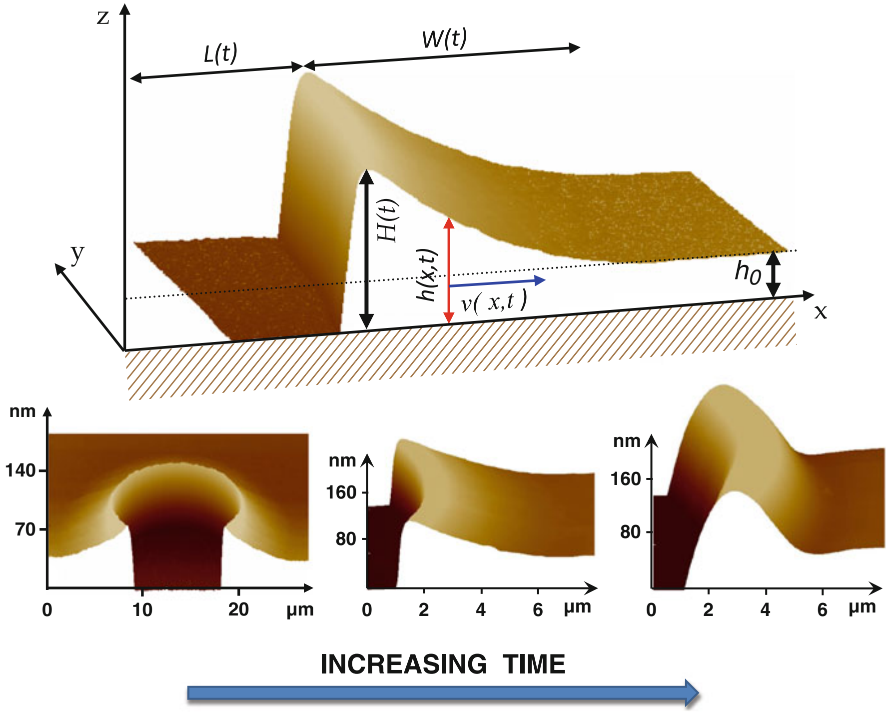

**Fig. 15** *Top*: 3D view (measured by AFM) of a typical hole obtained by dewetting a PS film on a PDMS-coated substrate at temperatures close to the glass transition of PS. $h(x,t)$ is the profile of the film, $h_0$ is the initial height of the film, $H(t)$ is the height of the front, $L(t)$ is the dewetted distance, $W(t)$ is the width of the rim, and $v(x,t)$ is the velocity of the film. *Bottom*: typical 3D cross-sections showing the asymmetric shape of the rim at early stages and comparatively low temperatures (*left*) and the more symmetric shape at late stages or at high temperatures (*right*)

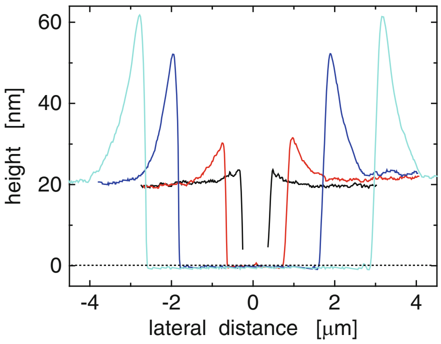

**Fig. 16** Cross-sections through holes and surrounding rims of highly asymmetric shape formed in a 20-nm thick PS film after annealing for 1, 5, 40, and 80 min at 120°C

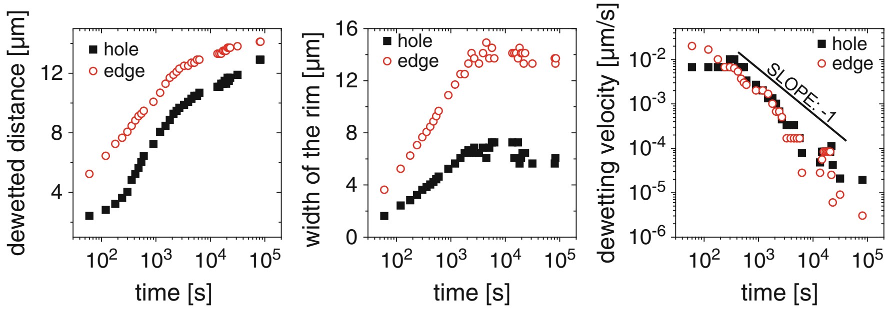

**Fig. 17** Results of a typical dewetting experiment for high molecular weight PS film. A 55-nm thick film ($M_w$ = 4,840 kg/mol) was dewetted at 130°C on a silicon wafer coated with an adsorbed PDMS layer ($M_w$ = 139 kg/mol). The growth of a nucleated hole is compared to dewetting from a straight edge, established by breaking the silicon wafer into two parts

Fig. 17, during the early stages of rim build-up, both the dewetted distance, $d$, and the width of the rim, $w$, increased in a logarithmic fashion in time, up to a time $\tau_w$ when $w$ reached a maximum ($w_{max}$). At times larger than $\tau_w$, the width of the rim either remained constant or decreased. $\tau_w$ can also be related to a transition of the highly asymmetric rims to more symmetric ones. During this early stage of rim build-up and even at times larger than $\tau_w$, the dewetting velocity $V$ decreased continuously according to a power law, $V \sim t^{-1}$. We note that, besides differences at very short times, the opening of a hole and the retraction from a straight line like the edge of the sample yielded similar dewetting kinetics (see Fig. 17).

We want to emphasize that a logarithmic time dependence of $d$ and $w$, and the corresponding $t^{-1}$ decrease of $V$, are not expected for a Newtonian liquid [42]. Moreover, our results cover times shorter than the longest relaxation time in equilibrated bulk samples (i.e., the reptation time). Thus, the visco-elastic properties of PS certainly affect our dewetting experiments. Thus, a detailed theoretical model has been developed that takes into account residual stresses, interfacial friction (i.e., slippage), and visco-elasticity [42, 44, 46].

In Fig. 18, we show the results of dewetting experiments performed at different temperatures and for two polymers of different lengths. $w$ always increased approximately logarithmically in time until it reached a maximum value at $\tau_w$. In equilibrated bulk samples, the existence of entanglements implies that the longest relaxation times (i.e., the reptation time $\tau_{rep}$) strongly depends on molecular weight, $M_w$ according to a power law, $\tau_{rep} \sim M_w^{3.4}$ [163, 164]. Moreover, the temperature dependence of the relaxation time follows a non-Arrhenius behavior when approaching $T_g$. The thermal evolution of relaxation times is usually described by the Vogel–Tamman–Fulcher (VTF) relation [163, 164], $\tau = \tau_0 \exp[B/(T - T_0)]$, with the material-dependent characteristic temperature $B = 1{,}170$ K and $T_0 = 343$ K for bulk PS [163, 164]. Interestingly, for the longer polymer, $\tau_w$ was drastically shorter than $\tau_{rep}$.

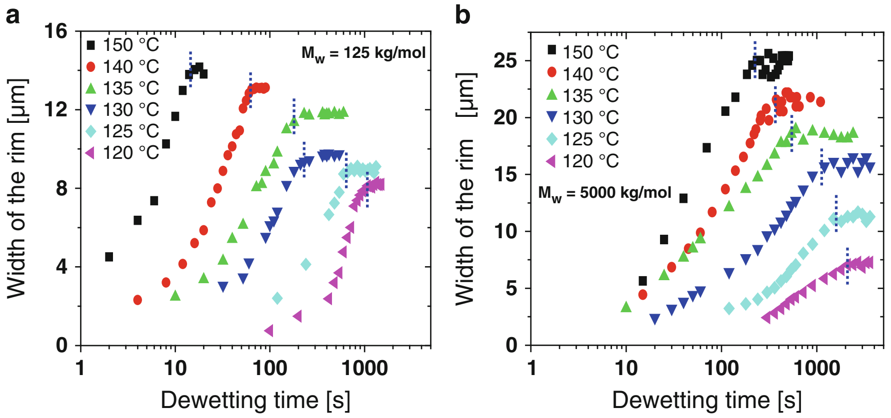

**Fig. 18** Temporal evolution of the width $w$ of the rim of holes growing in thin PS films of (**a**) $M_w = 125$ kDa and (**b**) $M_w = 5{,}000$ kDa as a function of dewetting time at various temperatures, as indicated. Relaxation time $\tau_w$ is determined by the time when the width of the rim reaches its maximum, as indicated by the *dotted lines*

In Fig. 19, we present a comparison of the values of $\tau_w$ for polymers of different chain lengths as a function of temperature. The shorter chains approximately followed a VTF behavior [163, 164] with the values of $\tau_w$ and $\tau_{rep}$ being almost identical at high temperatures. However, the longer polymers showed significant deviations from such behavior. At the lowest temperatures, we did not observe any influence of molecular weight. The values of $\tau_w$ were almost identical for all polymers studied. At higher temperatures $\tau_w$ varied only slightly with temperature, much less than expected from a VTF behavior. In addition, all values of $\tau_w$ were several orders of magnitude lower than $\tau_{rep}$ of these long chain polymers in the bulk.

The evolution of $\tau_w$ with molecular weight showed striking deviations from bulk behavior. For high molecular weights, we observed that the relaxation time $\tau_w$, as determined from a $w_{max}$ versus time plots, became almost independent of the chain length (Fig. 20).

For low $M_w$, this relaxation was clearly related to the reptation time, $\tau_{rep}$, suggesting that this relaxation process is dominated by the mobility of whole chains. In contrast, for high $M_w$ above about 300 kDa, very large deviations with respect to bulk reptation times were observed, suggesting that the corresponding relaxation process only requires the motion of a part of such long chains. For the longest chains studied, we found $\tau_w \ll \tau_{rep}$ by several orders of magnitude. The most striking feature is that almost the same value of $\tau_w$ was obtained for polymers of very different lengths.

Above results clearly demonstrate that dewetting can be considered as a “nano-rheology” experiment that gives insight into the structure and properties of out-of-equilibrium PS thin films. We may thus consider dewetting as a rheological “probe” for the study of the visco-elastic properties of nanoscopic polymer films.

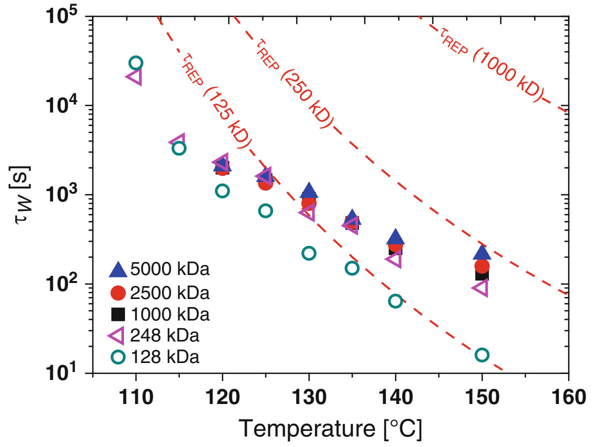

**Fig. 19** Evolution of the relaxation time $\tau_w$ (deduced from the position where the width of the rim reached a maximum value) as a function of dewetting temperature for PS of different molecular weights. Evolution of bulk reptation times is indicated by *dashed lines*. The film thickness was set at 40 nm

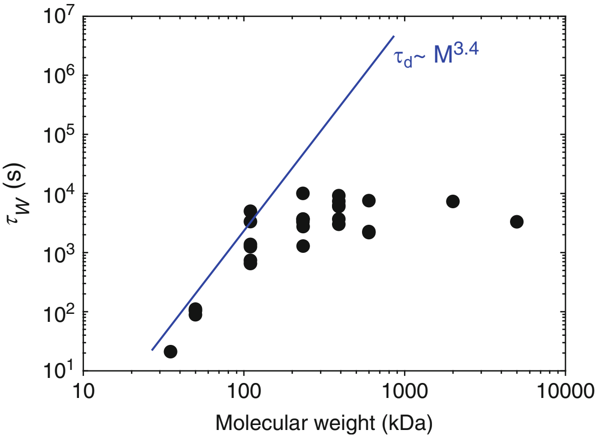

**Fig. 20** Evolution of the relaxation time $\tau_w$ (deduced from the width of the rim and the dewetting dynamics) as a function of molecular weight together with the evolution of bulk reptation times. $\tau_d$ is the reptation time representing the longest relaxation time of a polymer of molecular weight M. The film thickness was set at 100 nm

We tentatively interpret $\tau_w$ as the time needed to relax chain conformations, which were trapped in strongly out-of-equilibrium states. These conformations were generated by rapid solvent evaporation in the course of film preparation [17, 37–48] because the chains were rather diluted in solution and did not have sufficient time to establish the equilibrium state during the process of spin-coating.

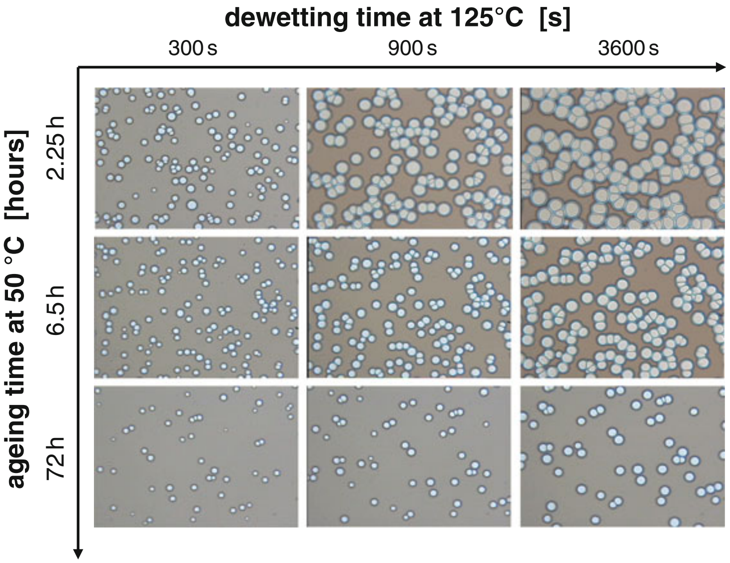

**Fig. 21** Influence of ageing PS films at 50°C on the probability of film rupture when annealing (and consequently dewetting) at 125°C. Clearly, the number of holes and the diameter at a given time of dewetting decrease with ageing time. The size of the images is 310 μm × 210 μm

We anticipate that the entanglement density in the dry spin-coated films is lower than in an equilibrated bulk system. Such a departure from equilibrium most likely generates residual stresses. As one consequence, we tentatively attribute the observed hole nucleation, which initiated the dewetting process of holes, to the presence of such residual stresses within the film [165]. In this way, rupture can be related to the spin-coating process used to prepare thin polymer films.

One may ask if these residual stresses are (partially) relaxing even in the glassy state of the film. Thus, we varied systematically the duration for which such films were stored below $T_g$. As a first phenomenon, we focused on the process of film rupture. In a second stage, we also studied the early stages of the dewetting dynamics. In Fig. 21, we present some typical results for PS films of high molecular weight polymers aged at 50°C for various times. As can be seen already from these micrographs, these two independent processes of rupture and dewetting proved equally and in parallel the significance of residual stresses and indicated that these stresses relaxed upon aging. The older the films were, the fewer holes were formed and the slower was the dewetting process.

The presence of residual stresses in polymer thin films can thus be considered as an explanation for the rupture mechanism via heterogeneous nucleation. We have found that the probability for film rupture, defined as the maximum number $N_{\text{max}}$ of circular holes per unit area formed in a film of given thickness, also depended on ageing time, the time the film was stored at temperatures below $T_g$ [17]. It should be noted that ageing of the films started at the time of the solvent quench during

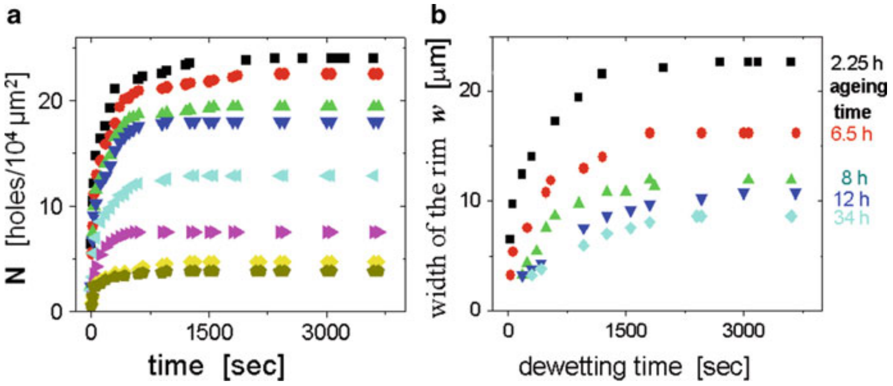

**Fig. 22** Influence of ageing on the probability of film rupture, expressed via the number of holes per unit area ($N$). (**a**) $N$ as a function of time at 125°C for PS films ($h_0 = 40$ nm, $M_w = 4{,}840$ kg/mol) after being aged at 50°C for increasing times (from *top* to *bottom*: 2.25, 6.5, 8, 12, 34, 72, 108, and 134 h). The maximum value $N_{max}$ (per $10^4$ $\mu m^2$) for each sample is reached within about 100 s. (**b**) Temporal evolution of the width $w$ of the rim of holes growing in these films after various ageing times at 50°C, as indicated. The maximum value $w_{max}$ was reached after about 2,000 s and clearly decreased with ageing time

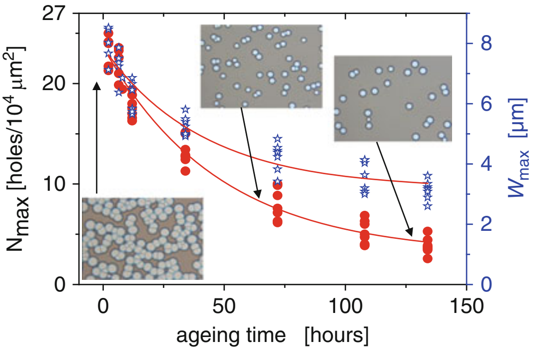

**Fig. 23** Systematic study of $N_{max}$ (*circles*) and $w_{max}$ (*stars*) for the same type of films as in Fig. 22, stored at 50°C for various times. The *insets* show some typical corresponding optical micrographs (310 µm × 230 µm). The *solid lines* represent the fit to an exponential function. The exponential behavior of $N_{max}$ is comparable to the exponential decrease in the maximum width of the rim ($w_{max}$) with aging time

spin-coating. As can be seen in Figs. 21, 22, and 23, a drastic reduction in hole density was observed after storing the films at 50°C for increasingly longer times.

The maximum number of holes ($N_{max}$) as a function of ageing time (Fig. 23) can be described by an exponential decay with ageing time $t_{ageing}$, such that $N_{max}(t_{ageing}) = N_{max}(\infty) + N_{max}(0) \cdot \exp[-t_{ageing}/\kappa(N_{max})]$, with a limiting value $N_{max}(\infty) = 3 \pm 1$ and a characteristic decay-time $\kappa(N_{max}) = 47 \pm 6$ h, implying that almost no holes will be formed after ageing the films for extended periods ($t_{\text{ageing}} \gg \kappa$). Some holes, however, may be nucleated by defects like dust particles.

Analogous to the initial rupture probability of the films (see Fig. 21), physical ageing at temperatures below $T_g$ also drastically influenced the dewetting dynamics [17]. Figure 22b shows that the maximum width of the rim, $w_{\max}$, and the dewetting velocity (not shown) decreased significantly when the films were aged. Measurable ageing effects could be achieved even at room temperature [17], i.e., 75°C below $T_g$. For example, after storing films for 42 days at room temperature, $w_{\max}$ decreased by a factor of 2. Systematic studies on the temporal evolution of $w_{\max}$ for films stored at 50°C (Fig. 22) showed an exponential decay of $w_{\max}$ with ageing time $t_{\text{ageing}}$, such that $w_{\max}(t_{\text{ageing}}) = w_{\max}(\infty) + w_{\max}(0)\cdot\exp[-t_{\text{ageing}}/\kappa(w_{\max})]$, exhibiting a characteristic decay time $\kappa(w_{\max}) = 41 \pm 7$ h, very close to the decay time observed for hole nucleation probability.

The large decrease in dewetting velocity observed during ageing at temperatures well below $T_g$ of PS can be interpreted by considering either a decrease in residual stress or a modification (in the course of ageing) of the PS–PDMS interface, and thus of the friction properties. Theoretically, the contribution of residual stresses to the dewetting dynamics is equivalent to an additional driving force, in parallel to the capillary forces. This additional force will decrease during dewetting. Relaxation of residual stresses during physical ageing also causes a reduction in the driving force. Residual stresses $\sigma$ lead to an increase of the initial dewetting velocity by a factor $(1 + h_0\sigma/|S|)$, with $S$ being the spreading factor given by $S = \gamma_{\text{sv}} - \gamma_{\text{sl}} - \gamma_{\text{lv}} \sim 10^{-2}$ N/m$^2$, where $\gamma_{\text{sv}}$, $\gamma_{\text{sl}}$, and $\gamma_{\text{lv}}$ are the solid–vapor, solid–liquid, and liquid–vapor surface energies, respectively [42].

Based on the assumption that the relaxation of the rim shape can be directly related to the relaxation of the residual stress [42, 44, 46], we conclude that a significant fraction of residual stress could be relaxed via limited motions of parts of the polymer chain. It should, however, be noted that even after $\tau_w$, the conformations of long chains probably still remain out-of-equilibrium, i.e., part of the residual stresses may relax without fully equilibrating the polymers.

The dewetting dynamics of such visco-elastic thin films can be described by a Jeffrey rheological model considering $G$ the elastic modulus (mainly due to chain entanglements), $\eta_0$ a short time viscosity and $\eta_1$ the melt viscosity [42–47, 164]. The relaxation times of the fluid are given by $\tau_{0,1} = \eta_{0,1}/G$ (the longest relaxation time, $\tau_1$ can be compared to the reptation time of the chains). The time response of such a fluid can thus be divided into three regimes. At short or long times ($t < \tau_0$ or $t > \tau_1$), the liquid behaves like a simple Newtonian liquid with small ($\eta_0$) or large ($\eta_1$) viscosity, respectively. For the intermediate regime, however, the liquid behaves like an elastic solid of modulus $G$. At times longer than the reptation time, the polymer chains started to flow as a viscous fluid of high viscosity and thus the dewetting velocity decreases as described by the classical power law related to viscous dewetting on slippery substrates, $V \sim t^{-1/3}$ [112, 144].

In the case of dewetting of purely elastic films, the height of the rim can only reach a well-defined maximum height $H_{\max}$. Assuming that only capillary stress ($S/h_0$) is acting at the contact line, we obtain: $H_{\max} - h_0 \sim S/G$. Mass conservation

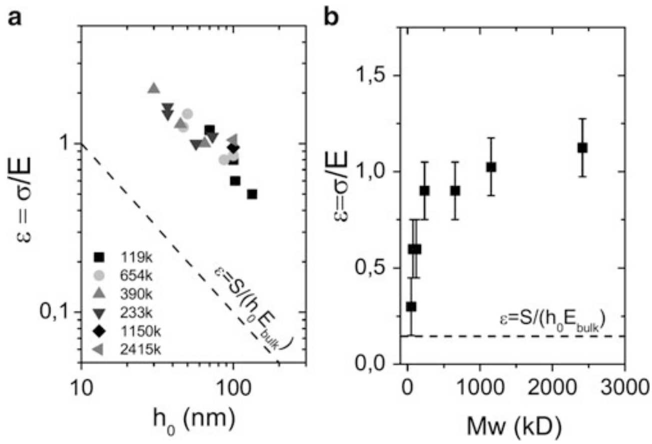

**Fig. 24** Evolution of the strain, $\varepsilon = (H - h_0)/h_0$, determined from the plateau value of a plot of the height increase $(H - h_0)$ versus the width of the rim $(w)$, with (**a**) film thickness ($M_w$ as indicated) and (**b**) molecular weight ($h_0 \sim 100$ nm). The *dashed line* in both graphs corresponds to the strain that would be expected for equilibrated PS films: $\varepsilon = S/(h_0\, E_{bulk})$ (adapted from [25])

imposes an augmentation of the rim width during the dewetting process: $d{\cdot}h_0 \sim w{\cdot}(H_{max} - h_0)$ [17, 43, 45], which finally yields the relations $H_{max} - h_0 \sim d/w{\cdot}h_0$ and $w = d{\cdot}h_0{\cdot}G/|S|$. Thus, the rim height can be determined from the rim width, $w$, and the dewetted distance, $d$, by considering the mass conservation.

For the time regime $\tau_0 > t > \tau_{rep}$, we expect a drastic influence of elasticity on rim formation. The strain, $\varepsilon$, can be easily deduced from the width of the rim, $w$, and the dewetted distance, $d$. We obtain: $\varepsilon = (H - h_0)/h_0 \sim 2d/w$. This relation between $d$, $w$, and $H$, and thus $\varepsilon$, was confirmed by AFM [43]. As shown in [43], the rim height first increases continuously with the rim width up to its maximum value, in agreement with the theoretical model proposed by Vilmin and Raphaël [42].

In the above presented experiments, the deformation of the elastic polymer (for times much shorter than the reptation time, a polymer behaves essentially like an elastic body) is given by the relation $\varepsilon = \sigma/E = (\sigma_{cap} + \sigma_{res})/E$. The strain, $\varepsilon$, is thus determined by the capillary stress at the edge of the film ($\sigma_{cap} = S/h_0$), the residual stress, $\sigma_{res}$, and the elastic modulus, $E$. For a PS film with equilibrated, fully entangled chain conformations ($G \sim 1$ MPa) and without residual stress, $\varepsilon$ is determined only by the capillary stress and is consequently very small, $\varepsilon \sim S/(h_0 E) \sim 0.1$, which is almost negligible in comparison with the high strains observed in the experiments represented in Fig. 24.

Several points need to be emphasized. High strains were observed even for film thicknesses much larger than the unperturbed dimension of the chains represented by the end-to-end distance of the polymer coils ($R_{ee}$). Thus, chain confinement can be ruled out as the cause for high values of $\varepsilon$.

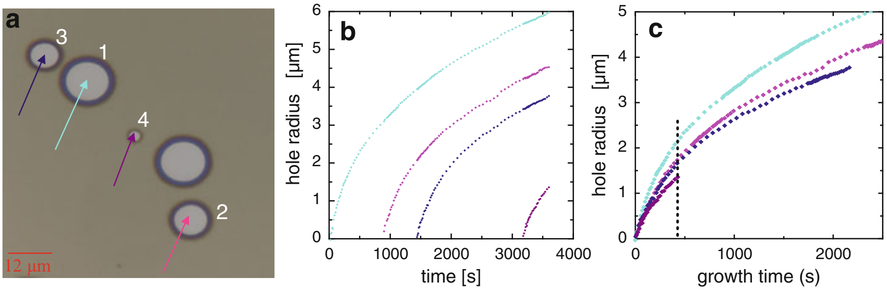

**Fig. 25** Growth of typical dewetting holes in a 45-nm thick PS film was followed by optical microscopy. (**a**) The four holes marked *1–4* were nucleated after an incubation time of 20, 900, 1,440, and 3,180 s, respectively, after the film was brought to 125°C. (**b**) The radius of each hole (*1–4* are shown from *top* to *bottom*, respectively) is plotted as a function of the time the film was incubated at 125°C. (**c**) The ordinate is rescaled to the time that each hole had grown since it was nucleated, rather than the time elapsed since the film reached 125°C

As $\varepsilon$ is given by the ratio $\sigma/E$, the explanation of high values of $\varepsilon$ may be linked to both large residual stresses and/or small elastic modulus. Both consequences leading to high values of $\varepsilon$ can be related to the preparation of the films by spin-coating.

The above experiments clearly point out that residual stresses can be introduced by rapid solvent loss during spin-coating, most likely caused by out-of-equilibrium chain conformations [42–46]. Consequently, the dewetting behavior reflects visco-elastic properties deviating from bulk [46]. However, at present, it is not clear how such chain conformations depend on the properties of the solution and on the solution-to-glass transition. Neither is it clear how the resulting mechanical and relaxation properties depend on the preparation stage. Thus, based on the well-supported hypothesis that film preparation introduces non-equilibrium chain conformations, we now focus on the influence of properties of the solution used for spin-casting by varying the solution temperature [48]. By increasing the temperature of the solution, we varied the radius of gyration from proportional to $N^{1/2}$ for a near-$\Theta$ solution to $N^{0.588}$ for good solvent conditions ($N$ is the number of monomers per chain). To this end, we used *trans*-decalin (TD) which is a solvent for PS and has a $\Theta$-temperature of about 21°C. The degree of swelling of PS chains in the solution could be varied over a considerable range [166]. For the long chain polymer used ($M_w = 4{,}060$ kDa), the coil radius changes by about 40% when changing the temperature from 21°C to 55°C. We first study the dewetting dynamics for a 45-nm thick PS film prepared at 23°C. When brought to $T = 125°\text{C} > T_g$, the holes nucleated after various incubation times (see Fig. 25). Such a gradual nucleation of holes allowed direct comparison of holes having experienced different thermal history. Holes that nucleated at later times exhibited a slower opening rate.

A comparison of the hole radius (measured at a constant growth time of 430 s) indicates an exponential relaxation (see Fig. 26), yielding a decay time of about 30 min for the hole-opening driving force.

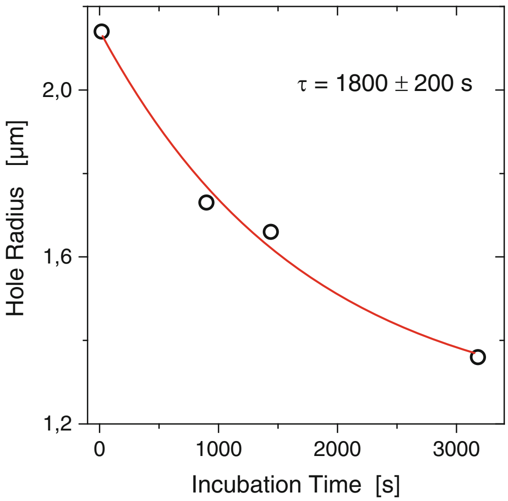

**Fig. 26** Hole radius after a growth time of 430 s (*vertical dotted line* in Fig. 25c) as a function of incubation time. $\tau$ decay time

This dependence of hole radius on incubation time clearly demonstrates relaxation processes within the film even in the course of dewetting. Note that the differences in hole opening behavior were observed in a single sample and almost simultaneously.

The relaxation process may lead either to a decrease in residual stress or an increase in elastic properties, or both, with incubation time. However, independent of the actual interpretation, these results support the hypothesis that the chains in the films, which were initially out of equilibrium, tend to equilibrate during annealing. As shown above, this relaxation process was documented by dewetting. Interestingly, relaxations were much faster than according to bulk reptation at 125°C for the high molecular weight PS used here ($\tau_{\mathrm{rep}} \sim 2 \times 10^8$ s) [43, 104, 163, 164].

In a second series of experiments, films spin-cast from TD at 25°C were aged at room temperature for various times before being heated to 125°C for dewetting measurements. Only holes nucleated immediately upon reaching 125°C were considered. Figure 27 displays characteristic results for the hole-opening kinetics for films with increasing aging time. The hole radii of these six samples at three fixed hole-opening times show an exponential decay, defining an almost identical characteristic relaxation time of the film of 43 ± 9 h. Note that a comparison between samples aged in ambient atmosphere and in vacuum showed no difference in dewetting behavior, excluding an effect of residual solvent in the film.

Additional samples made from solutions of varying solvent quality, i.e., films that were spin-cast from TD at different temperatures, were also aged at room temperature and analyzed in terms of their hole radius or dewetting velocity as a function of dewetting time. Varying the temperature of the spin-coating solution has a substantial effect on the room temperature relaxation process of these films spun from TD solutions (see Fig. 28), corresponding to a change in relaxation times

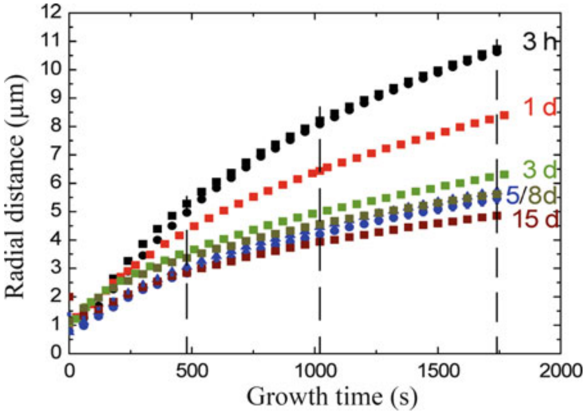

**Fig. 27** Growth of dewetting holes nucleated immediately upon heating to 125°C in films cast from TD at 25°C that had been aged at room temperature for the times indicated. Holes exhibit decreasing growth velocities with increasing ageing time. Hole radii taken at three constant times (480, 1,020 and 1,740 s, indicated by the vertical *dashed lines*) follow an exponential decay with a characteristic time of 43 ± 9 h, reflecting a relaxation process of chain segments within the film at room temperature, i.e., in the glassy state

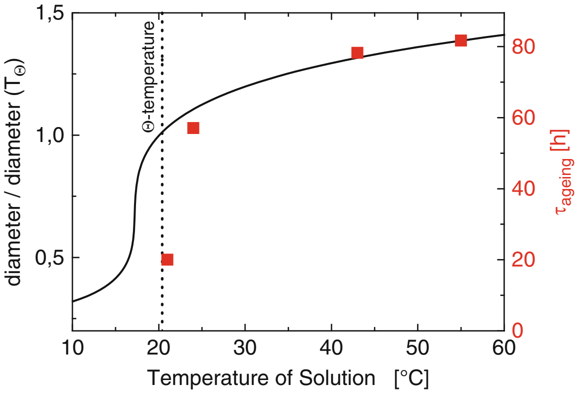

**Fig. 28** Relaxation time $\tau_{\text{ageing}}$ *(squares)* as a function of temperature of the solution from which the films were spun. The *solid line* represents the coil diameter of the individual polymer in solution, normalized by its diameter at the Θ temperature of PS in *trans*-decalin (indicated by the vertical *dotted line*)

by a factor of 4. In comparison, films cast from toluene (at room temperature) had a relaxation time of ~700 h at room temperature, in agreement with the extrapolation of Fig. 28 to the athermal limit (i.e., a relative coil diameter of 2.5).

A decrease in dewetting velocity with increased aging time is indicative of a decaying stress or an increasing modulus with aging time of the sample. Figure 28 indicates that the relaxation time determined from dewetting experiments on aged samples follows a similar trend with temperature as does the coil diameter in solution. Thus, we may tentatively conclude that more compact chains in solution at lower temperatures allow only the formation of a lower number of entanglements with other chains. Consequently, these more weakly entangled polymers yield a lower film modulus and allow a faster relaxation process in the glassy state at room temperature.

## 5 Conclusions

The examples presented here clearly demonstrate the potential of dewetting studies for the investigation of properties of thin polymer films. The main advantage of the dewetting approach is its simplicity in obtaining complementary information on the relation between the molecular scale interfacial properties and macroscopic behavior, both static and kinetic. Using a Newtonian fluid as a model system allowed us to verify that the underlying physics of the dewetting process is well understood.

Applying this approach to spin-coated glassy PS films opens up several interesting possibilities for the study of visco-elastic properties and relaxation processes in such films. In particular, significant deviations from bulk behavior could be identified for films of high molecular weight. Moreover, dewetting also indicates that the conformation of chains in the initial solution has a great impact on the behavior of resultant dry films due to the out-of-equilibrium states that are frozen-in by spin-coating. In general, dewetting experiments are able to demonstrate the role of the non-equilibrium conformation of the chains in the film. Our data on films aged at room temperature suggest a variation in quenched chain entanglements that depends on the solvent quality from which the film was cast. We see that the quality of the solvent and the history of the solution up to the point of vitrification, not just the thermal history of the film after vitrification, must be taken into account to predict the behavior of polymeric thin films.

The strong dependence of film preparation conditions on the aging behavior of thin films far below $T_g$ and the observation of significant changes even at room temperature may also be of relevance in the context of the low "softening" temperature of thin polymer films, typically interpreted as a reduced $T_g$. While the deformation of polymer coils as a whole should not modify the solidification temperature of the film, which is dominated by the segmental dynamics, our aging experiments indicate that spin-coating perturbs the polymer coils down to the segmental length scale. At present, it is not clear if and how our observations using dewetting can be reconciled with a lowered $T_g$. Thus, further experiments are needed to verify whether non-equilibrium chain conformations induced, e.g., by film preparation can explain all anomalous properties of thin polymer films, such as deviations from $T_g$ in the bulk.

**Acknowledgments** I am highly indebted to Françoise Brochard and the late Pierre-Gilles de Gennes for many invaluable discussions. I wish to thank Rajesh Khanna, Samer Al Akhrass, Pascal Damman, Mithun Chowdhury, Ulli Steiner, Adam Raegen, Thomas Vilmin, Falko Ziebert, and Elie Raphaël for the fruitful collaborations which are at the base of the results presented here. I am grateful to the Deutsche Forschungsgemeinschaft (RE2273/3-1) for funding of the most recent part of this work and partial financial support from the European Community's "Marie-Curie Actions" under contract MRTN-CT-2004-504052 [POLYFILM] for the earlier stage of the work.

## References

1. Reiter G (1993) Europhys Lett 23:579–584; (1994) Macromolecules 27:3046–3052
2. Orts WJ, van Zanten JH, Wu WL, Satija SK (1993) Phys Rev Lett 71:867–870
3. Sanyal MK, Basu JK, Datta A, Banerjee S (1996) Europhys Lett 36:265–270
4. Reiter G, de Gennes PG (2001) Eur Phys J E 6:25–28
5. Mukherjee M, Bhattacharya M, Sanyal MK, Geue T, Grenzer J, Pietsch U (2002) Phys Rev E 66:061801
6. Bhattacharya M, Sanyal MK, Geue T, Pietsch U (2005) Phys Rev E 71:041801
7. Kanaya T, Miyazaki T, Watanabe H, Nishida K, Yamana H, Tasaki S, Bucknall DB (2003) Polymer 44:3769–3773
8. Miyazaki T, Nishida K, Kanaya T (2004) Phys Rev E 69:022801
9. Richardson H, Lopez-Garcia I, Sferrazza M, Keddie JL (2004) Phys Rev E 70:051805
10. Bollinne C, Cuenot S, Nysten B, Jonas AM (2003) Eur Phys J E 12:389–395
11. Tsui OKC, Russell TP (2008) Polymer thin films. World Scientific, Singapore
12. Tsui OKC, Wang YJ, Lee FK, Lam CH, Yang Z (2008) Macromolecules 41:1465–1468
13. Dalnoki-Veress K, Nickel B, Roth C, Dutcher J (1999) Phys Rev E 59:2153–2156
14. Akabori K-I, Tanaka K, Kajiyama T, Takahara A (2003) Macromolecules 36:4937–4943
15. Kawana S, Jones RAL (2003) Eur Phys J E 10:223–230
16. Priestley RD, Broadbelt LJ, Torkelson JM (2005) Macromolecules 38:654–657
17. Reiter G, Hamieh M, Damman P, Sclavons S, Gabriele S, Vilmin T, Raphael E (2005) Nat Mater 4:754–758
18. Lee H, Paeng K, Swallen S, Ediger M (2008) J Chem Phys 128:134902
19. Fukao K, Koizumi H (2008) Phys Rev E 77:021503
20. Priestley RD (2009) Soft Matter 5:919–926
21. Pye JE, Rohald KA, Baker EA, Roth CB (2010) Macromolecules 43:8296–8303
22. Brown HR, Russell TP (1996) Macromolecules 29:798–800
23. Herminghaus S, Jacobs K, Seemann R (2001) Eur Phys J E 5:531–538
24. Efremov M et al (2003) Phys Rev Lett 91:085703
25. Fakhraai Z, Forrest JA (2005) Phys Rev Lett 95:25701
26. Fakhraai Z, Valadkhan S, Forrest JA (2005) Eur Phys J E 18:143
27. Fakhraai Z, Forrest JA (2008) Science 319:600–604
28. Rathfon JM, Cohn RW, Crosby AJ, Tew GN (2011) Macromolecules 44:134–139
29. Jones R, Kumar S, Ho D, Briber R, Russell TP (1999) Nature 400:146–149
30. Brulet A, Boue F, Menelle A, Cotton JP (2000) Macromolecules 33:997–1001
31. Kraus J, Müller-Buschbaum P, Kuhlmann T, Schubert D, Stamm M (2000) Europhys Lett 49:210–216
32. Si L, Massa MV, Dalnoki-Veress K, Brown HR, Jones RAL (2005) Phys Rev Lett 94:127801
33. Reiter G, Schultz J, Auroy P, Auvray L (1996) Europhys Lett 33:29
34. Debregeas G, de Gennes PG, Brochard-Wyart F (1998) Science 279:1704–1707
35. Reiter G (2001) Phys Rev Lett 87:186101
36. Reiter G (2002) Eur Phys J E 8:251–255

37. Damman P, Baudelet N, Reiter G (2003) Phys Rev Lett 91:216101
38. Gabriele S, Sclavons S, Reiter G, Damman P (2006) Phys Rev Lett 96:156105
39. Bodiguel H, Fretigny C (2006) Eur Phys J E 19:185–193
40. Yang MH, Hou SY, Chang YL, Yang ACM (2006) Phys Rev Lett 96:066105
41. Gabriele S, Damman P, Scalvons S, Desprez S, Coppée S, Reiter G, Hamieh M, Al-Akhrass S, Vilmin T, Raphaël E (2006) J Polym Sci B Polym Phys 44:3022
42. Vilmin T, Raphaël E (2006) Eur Phys J E 21:161
43. Damman P, Gabriele S, Coppee S, Desprez S, Villers D, Vilmin T, Raphael E, Hamieh M, Al-Akhrass S, Reiter G (2007) Phys Rev Lett 99:036101
44. Vilmin T, Raphaël E, Damman P, Sclavons S, Gabriele S, Hamieh M, Reiter G (2006) Europhys Lett 73:906
45. Reiter G, Al Akhrass S, Hamieh M, Damman P, Gabriele S, Vilmin T, Raphael E (2009) Eur Phys J ST 166:165–172
46. Ziebert F, Raphaël E (2009) Phys Rev E 79:031605
47. Ziebert F, Raphael E (2009) Europhys Lett 86:46001
48. Raegen A, Chowdhury M, Calers C, Schmatulla A, Steiner U, Reiter G (2010) Phys Rev Lett 105:227801
49. Coppée S, Gabriele S, Jonas A, Jestin J, Damman P (2011) Soft Matter 7:9951
50. Richardson H, Carelli C, Keddie J, Sferrazza M (2003) Eur Phys J E 12:437–441
51. Chung JY, Chastek TQ, Fasolka MJ, Ro HW, Stafford CM (2009) ACS Nano 3:844–852
52. Barbero DR, Steiner U (2009) Phys Rev Lett 102:248303
53. Thomas KR, Chenneviere A, Reiter G, Steiner U (2011) Phys Rev E 83:021804
54. Thomas K, Steiner U (2011) Soft Matter 7:7839
55. Keddie JL, Jones RAL, Cory RA (1994) Europhys Lett 27:59
56. Forrest JA, Dalnoki-Veress K, Stevens JR, Dutcher JR (1996) Phys Rev Lett 77:2002–2005
57. Forrest JA, Dalnoki-Veress K, Dutcher JR (1997) Phys Rev E 56:5705–5716
58. Prucker O, Christian S, Bock H, Rühe J, Frank CW, Knoll W (1998) Macromol Chem Phys 199:1435–1444
59. Forrest JA, Mattsson J (2000) Phys Rev E 61:R53–R56
60. Forrest JA, Dalnoki-Veress K (2001) Adv Coll Interf Sci 94:167
61. van der Lee A, Hamon L, Holl Y, Grohens Y (2001) Langmuir 17:7664–7669
62. Dalnoki-Veress E, Forrest JA, Murray C, Gigault C, Dutcher JR (2001) Phys Rev E 63:031801
63. Tsui OKC, Zhang HF (2001) Macromolecules 34:9139–9142
64. Reiter G, Forrest J (2002) Special issue on properties of thin polymer films. Eur Phys J E 8:101
65. Grohens Y, Hamon L, Spevacek J, Holl Y (2003) Macromol Symp 203:155–164
66. Ellison CJ, Torkelson JM (2003) Nat Mater 2:695–700
67. Soles CL, Douglas JF, Wu WL, Peng HG, Gidley DW (2004) Macromolecules 37:2890–2900
68. Soles CL, Douglas JF, Jones RL, Wu WL (2004) Macromolecules 37:2901–2908
69. Ellison CJ, Ruszkowski RL, Fredin NJ, Torkelson JM (2004) Phys Rev Lett 92:095702
70. O'Connell PA, McKenna GB (2005) Science 307:1760
71. Alcoutlabi M, McKenna GB (2005) J Phys Condens Matter 17:R461–R524
72. Priestley RD, Ellison CJ, Broadbelt LJ, Torkelson JM (2005) Science 309:456–459
73. Lupascu V, Picken SJ, Wübbenhorst M (2006) Macromolecules 39:5152–5158
74. Peter S, Meyer H, Baschnagel J (2006) J Polym Sci B Polym Phys 44:2951–2967
75. Napolitano S, Wübbenhorst M (2007) J Phys Chem B 111:5775–5780
76. Napolitano S, Wübbenhorst M (2007) J Phys Chem B 111:9197–9199
77. Napolitano S, Prevosto D, Lucchesi M, Pingue P, D'Acunto M, Rolla P (2007) Langmuir 23:2103–2109
78. Napolitano S, Lupascu V, Wübbenhorst M (2008) Macromolecules 41:1061–1063
79. Yang ZH, Wang YJ, Todorova L, Tsui OKC (2008) Macromolecules 41:8785–8788
80. Serghei A, Kremer F (2008) Macromol Chem Phys 209:810–817

81. Peter S, Napolitano S, Meyer H, Wübbenhorst M, Baschnagel J (2008) Macromolecules 41:7729–7743
82. Kim S, Hewlett SA, Roth CB, Torkelson JM (2009) Eur Phys J E 30:83–92
83. Rotella C, Napolitano S, Wübbenhorst M (2009) Macromolecules 42:1415–1417
84. Napolitano S, Pilleri A, Rolla P, Wübbenhorst M (2010) ACS Nano 4:841–848
85. Tress M, Erber M, Mapesa EU, Huth H, Müller J, Serghei A, Schick C, Eichhorn K-J, Voit B, Kremer F (2010) Macromolecules 43:9937–9944
86. Raegen A, Massa M, Forrest JA, Dalnoki-Veress K (2008) Eur Phys J E 27:375–377
87. Reiter G, Napolitano S (2010) J Polym Sci B Polym Phys 48:2544
88. McKenna GB (2010) Eur Phys J ST 189:285–302
89. Kim S, Mundra MK, Roth CB, Torkelson JM (2010) Macromolecules 43:5158–5161
90. Rowland H, King W, Pethica J, Cross G (2008) Science 322:720–724
91. Roth CB (2010) J Polym Sci B Polym Phys 48:2558–2560
92. Yang Z, Fujii Y, Lee FK, Lam C-H, Tsui OKC (2010) Science 328:1676–1679
93. Rotella C, Napolitano S, De Cremer L, Koeckelberghs G, Wübbenhorst M (2010) Macromolecules 43:8686–8691
94. Napolitano S, Wübbenhorst M (2011) Nat Commun 2:260
95. Paeng K, Swallen SF, Ediger MD (2011) J Am Chem Soc 133:8444–8447
96. Paeng K, Richert R, Ediger MD (2012) Soft Matter 8:819
97. Siretanu I, Chapel JP, Drummond C (2012) Macromolecules 45:1001–1005
98. Bornside D, Macosko C, Scriven L (1987) J Imaging Technol 13:122–128
99. Croll SG (1979) J Appl Polym Sci 23:847–858
100. Sauer BB, Walsh DJ (1994) Macromolecules 27:432–440
101. de Gennes PG (2002) Eur Phys J E 7:31–34
102. Karim A, Mansour A, Felcher GP, Russell TP (1990) Phys Rev B 42:6846
103. Stamm M, Hüttenbach S, Reiter G, Springer T (1991) Europhys Lett 14:451
104. Reiter G, Steiner U (1991) J Phys II (France) 1:659
105. Russell TP, Deline VR, Dozier WD, Felcher GP, Agrawal G, Wool RP, Mays JW (1993) Nature 365:235
106. de Gennes PG (1992) In: Sanchez IC (ed) Physics of polymer surfaces and interfaces. Butterworth-Heinemann, Boston, p 55
107. Reiter G (1992) Phys Rev Lett 68:75–78; (1993) Langmuir 9:1344–1351
108. de Gennes PG, Brochard-Wyart F, Quéré D (2004) Capillarity and wetting phenomena: drops, bubbles, pearls, waves. Springer, Heidelberg
109. Brochard-Wyart F, di Meglio JM, Quéré D, de Gennes PG (1991) Langmuir 7:335
110. Redon C, Brochard-Wyart F, Rondelez F (1991) Phys Rev Lett 66:715
111. Brochard-Wyart F, Redon C (1992) Langmuir 8:2324
112. Brochard-Wyart F, Martin P, Redon C (1993) Langmuir 9:3682
113. Brochard-Wyart F, de Gennes PG, Hervert H, Redon C (1994) Langmuir 10:1566
114. Lambooy P, Phelan KC, Haugg O, Krausch G (1996) Phys Rev Lett 76:1110
115. Krausch G (1997) J Phys Condens Matter 9:7741
116. Stange TG, Evans DF, Hendrickson WA (1997) Langmuir 13:4459
117. Pan Q, Winey KI, Hu HH, Composto RJ (1997) Langmuir 13:1758
118. Jacobs K, Herminghaus S, Mecke KR (1998) Langmuir 14:965
119. Limary R, Green PF (1999) Langmuir 15:5617
120. Seemann R, Herminghaus S, Jacobs K (2001) Phys Rev Lett 87:196101
121. Vrij A (1966) Discuss Faraday Soc 42:23
122. Brochard-Wyart F, Daillant J (1990) Can J Phys 68:1084
123. Sharma A (1993) Langmuir 9:861; 9:3580
124. Reiter G, Sharma A, Casoli A, David MO, Khanna R, Auroy P (1999) Langmuir 15:2551
125. Reiter G, Sharma A, Casoli A, David MO, Khanna R, Auroy P (1999) Europhys Lett 46:512
126. Reiter G, Khanna R, Sharma A (2000) Phys Rev Lett 85:1432
127. Xie R et al (1998) Phys Rev Lett 81:1251

128. Thiele U, Mertig M, Pompe W (1998) Phys Rev Lett 80:2869
129. Reiter G (1998) Science 282:888
130. Herminghaus S (1999) Phys Rev Lett 83:2359
131. Seemann R, Herminghaus S, Neto C, Schlagowski S, Podzimek D, Konrad R, Mantz H, Jacobs K (2005) J Phys Condens Matter 17:S267
132. De Gennes PG (1985) Rev Mod Phys 57:827
133. Young T (1805) Philos Trans R Soc Lond 95:65
134. Bonn D, Eggers J, Indekeu J, Meunier J, Rolley E (2009) Rev Mod Phys 81:739
135. Huh C, Scriven LE (1971) J Coll Interf Sci 35:85
136. Tanner LH (1979) J Phys D 2:1473
137. de Gennes PG (1979) CR Acad Sci 288B:219
138. Leger L, Joanny JF (1992) Rep Prog Phys 55:431
139. Redon C, Brzoka JB, Brochard-Wyart F (1994) Macromolecules 27:468
140. Raphaël E, de Gennes PG (1992) J Phys Chem 96:4002
141. Brown HR (1994) Science 263:1411
142. Shanahan MER, Carré A (1995) Langmuir 11:1396
143. Debrégeas G, Martin P, Brochard-Wyart F (1995) Phys Rev Lett 75:3886
144. Brochard-Wyart F, Debrégeas G, Fondecave R, Martin P (1997) Macromolecules 30:1211
145. Debrégeas G, de Gennes PG, Brochard-Wyart F (1998) Science 279:1704
146. Reiter G, Khanna R (2000) Langmuir 16:6351
147. Reiter G, Khanna R (2000) Phys Rev Lett 85:2753
148. Casoli A, Brendlé M, Schultz J, Auroy P, Reiter G (2001) Langmuir 17:388
149. Bureau L, Léger L (2004) Langmuir 20:4523
150. Masson J, Green P (2002) Phys Rev Lett 88:205504
151. Rauscher M, Münch A, Wagner B, Blossey R (2005) Eur Phys J E 17:373
152. Fetzer R, Rauscher M, Münch A, Wagner BA, Jacobs K (2006) Europhys Lett 75:638
153. Bäumchen O, Fetzer R, Jacobs K (2009) Reduced interfacial entanglement density affects the boundary conditions of polymer flow. Phys Rev Lett 103:247801
154. Neto C, Evans DR, Bonaccurso E, Butt H-J, Craig VSJ (2005) Rep Prog Phys 68:2859
155. Bäumchen O, Jacobs K (2010) Slip effects in polymer thin films. J Phys Condens Matter 22:033102
156. Leibler L, Ajdari A, Mourran A, Coulon G, Chatenay D (1994) In: Teramoto A, Kobayashi M, Norisuje T (eds) Ordering in macromolecular systems. Springer, Berlin, p 301
157. Shull K (1994) Faraday Discuss 98:203
158. Gay C (1997) Macromolecules 30:5939
159. Ferreira PG, Ajdari A, Leibler L (1998) Macromolecules 31:3994
160. Matsen MW, Gardiner JM (2001) J Chem Phys 115:2794
161. Müller M, MacDowell LG (2001) Europhys Lett 55:221
162. Roth CB, Deh B, Nickel BG, Dutcher JR (2005) Phys Rev E 72:021802
163. Plazek DJ, O'Rourke VM (1971) J Polym Sci Part A2 9:209
164. Bach A, Almdal K, Rasmussen HK, Hassager O (2003) Macromolecules 36:5174
165. Vilmin T, Raphaël E (2006) Phys Rev Lett 97:036105
166. Sun S et al (1980) J Chem Phys 73:5971

Adv Polym Sci (2013) 252: 65–106
DOI: 10.1007/12_2012_172

# Heterogeneous and Aging Dynamics in Single and Stacked Thin Polymer Films

**Koji Fukao, Takehide Terasawa, Kenji Nakamura, and Daisuke Tahara**

**Abstract** The glass transition and the α-process above the glass transition temperature, $T_g$, and the aging dynamics below $T_g$ were investigated for single and stacked thin polymer films. First, the glass transition dynamics of stacked thin films of polystyrene (PS) and poly(2-chlorostyrene) (P2CS) were measured using differential scanning calorimetry and dielectric relaxation spectroscopy. The $T_g$ for as-stacked thin PS films is much less than that of the bulk sample. However, after annealing at high temperatures above $T_g$, the stacked thin films exhibit glass transition at a temperature almost equal to the $T_g$ of the bulk system. The α-process dynamics of stacked thin films of P2CS show a very slow time evolution from single thin film-like dynamics to bulk-like dynamics during the isothermal annealing process. The temperature dependence of the relaxation time for the α-process changes from Arrhenius-like to a Vogel–Fulcher–Tammann dependence with an increase in annealing time. Secondly, the aging dynamics of P2CS ultrathin films with thicknesses less than 10 nm were investigated using dielectric relaxation spectroscopy. The imaginary part of the dielectric susceptibility, $\varepsilon''$, for P2CS ultrathin films with a thickness of 3.7 nm increases with an increase in isothermal aging time, but this is not the case for P2CS thin films thicker than 9.0 nm. This anomalous increase in $\varepsilon''$ for the ultrathin films is strongly correlated with the presence of a mobile liquid-like layer within the thin films.

**Keywords** Aging dynamics · Glass transition · Heterogeneous dynamics · Interfacial interaction · Memory and rejuvenation effects · Stacked thin polymer films

---

K. Fukao (✉), T. Terasawa, K. Nakamura, and D. Tahara
Department of Physics, Ritsumeikan University, Noji-Higashi 1-1-1, Kusatsu 525-8577, Japan
e-mail: fukao.koji@gmail.com

## Contents

1 Introduction ........ 66
  1.1 Glass Transition of Thin Polymer Films ........ 67
  1.2 Aging Phenomena of Polymer Glasses ........ 69
  1.3 Heterogeneous and Aging Dynamics in Single and Stacked Thin Polymer Films . 72
2 Experiments ........ 73
  2.1 Sample Preparation ........ 73
  2.2 Measurements for Stacked Thin Polymer Films ........ 74
  2.3 Measurements of Aging Dynamics in Thin Polymer Films ........ 75
3 Glass Transition Temperature of Thin P2CS Films ........ 76
4 Glass Transition Dynamics of Stacked Thin Polymer Films ........ 77
  4.1 Thermal Properties Determined by Differential Scanning Calorimetry ........ 77
  4.2 Evolution of Glass Transition Dynamics for Stacked Thin Films ........ 79
  4.3 Dynamics of the α-Process for Stacked P2CS Thin Films ........ 84
  4.4 Remarks on the Glass Transition Dynamics of Stacked Thin Films ........ 89
5 Aging Dynamics in Ultrathin P2CS Films ........ 90
  5.1 Segmental Dynamics in Ultrathin P2CS Films ........ 92
  5.2 Microscopic Origin of the Anomaly ........ 97
  5.3 Remarks on Anomaly Observed in Aging Dynamics in Ultrathin P2CS Films .... 101
6 Summary ........ 102
References ........ 103

# 1 Introduction

If a material in the liquid state at high temperature is cooled down in an appropriate manner, the material can often keep the liquid state even below the melting temperature; this state is called the supercooled liquid state. Further cooling of the supercooled liquid enables us to obtain a solid state with disordered molecular arrangement similar to the liquid state but without any of the mobility characteristic of the liquid state, if no crystallization occurs during further cooling [1]. This disordered solid state is the glassy state and the transition from the liquid state to the glassy state via the supercooled liquid state is known as the glass transition. The temperature at which the glass transition occurs defines the glass transition temperature $T_g$. It should be noted that the glassy state is a non-equilibrium state. The understanding of the mechanism of the glass transition remains one of the most important unsolved problems in condensed matter physics [2], although there have been many approaches not only from experimental and theoretical viewpoints but also from simulational viewpoints [3–8].

The results observed so far have revealed several anomalous dynamical behavior related to the glass transitions. First, the characteristic time $\tau_\alpha$ of the main motion excited in the liquid states, which is the α-process, becomes extraordinarily longer with decreasing temperature down to $T_g$ in a manner given by:

$$\tau_\alpha^{-1} = \tau_{\alpha,0}^{-1} \exp\left(-\frac{U}{T - T_0}\right), \tag{1}$$

where $\tau_{\alpha,0}$ is a characteristic time of an elementary process of the $\alpha$-process, $U$ is an apparent activation energy, and $T_0$ is the Vogel temperature, which is by about 50 K lower than $T_g$. This is called the Vogel–Fulcher–Tammann (VFT) law [9–11]. Hence, it is expected that the time scale of the $\alpha$-process becomes a macroscopic time scale, i.e., $10^2$–$10^3$ s at $T_g$. As a result, the molecular mobility induced by the $\alpha$-process is almost lost and the disordered structure is totally frozen in the glassy state. The relaxation function $\phi(t)$, which is obtained by relaxation measurements such as dielectric relaxation spectroscopy (DRS), viscoelastic measurements and so on, is given not by the single exponential function but by the stretched exponential function:

$$\phi(t) = \exp\left[-\left(\frac{t}{\tau_K}\right)^{\beta_K}\right], \tag{2}$$

where $\beta_K$ is the stretching parameter, $0 < \beta_K < 1$, and $\tau_K$ is a relaxation time ($\tau_K \approx \tau_\alpha$ for the $\alpha$-process) [12]. The observed relation that $0 < \beta_K < 1$ means that there are distributions of the relaxation times $\tau_\alpha$ of the $\alpha$-process in real systems; in other words, there are many motional units with different characteristic times. Recent further investigations clearly show that the motional units of the $\alpha$-process with various values of $\tau_\alpha$ move not independently but in a collective manner. This type of character of the molecular motion is usually known as dynamical heterogeneity [13, 14]. Within the system, there are several domains with slower motions or faster motions. As temperature approaches from high temperature to $T_g$, the dynamical heterogeneity grows significantly, especially in the supercooled liquid state, and this is one of the most important characteristics of the dynamical nature of the glass transition. According to this scenario, there should be a length scale that characterizes the dynamical heterogeneity in the liquid states near the glass transition. This idea is associated with a cooperative rearranging region (CRR), which was proposed by Adam and Gibbs in 1965 [15]. Therefore, the experimental approaches to such characteristic length scale of the glass transition and the $\alpha$-process have been important issues that should be clarified in order to elucidate the mechanism of the glass transition.

## *1.1 Glass Transition of Thin Polymer Films*

If there is a characteristic length scale of the glass transition and the $\alpha$-process, it can be expected that there is an appreciable change in the glass transition dynamics as the system size decreases down to the length scale. Many investigations on the glass transition on small scales or in confined systems (i.e., the glass transitions of small molecules in nanopores or thin polymer films) have been widely performed since the 1990s [16]. The investigations on confined systems have revealed that the $T_g$ of thin polymer films or small molecules in a confined geometry decreases with

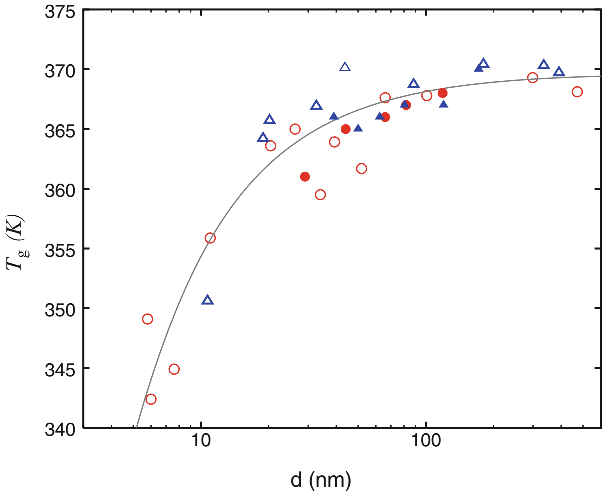

**Fig. 1** Thickness (*d*) dependence of $T_g$ of atactic PS films obtained during the heating process (*open circles* correspond to $M_w = 2.8 \times 10^5$, and *open triangles* to $M_w = 1.8 \times 10^6$). The values of $T_g$ are determined as the crossover temperature between the *straight lines* characterizing the real part of electric capacitance $C'(T)$ at 10 kHz below and above $T_g$. The *filled circles* ($M_w = 7.67 \times 10^5$) and *filled triangles* ($M_w = 2.2 \times 10^6$) represent the data obtained for uncapped supported films of atactic PS by Forrest et al. using ellipsometry for atactic PS [37]. The *solid curve* was obtained from the layer model [27]

decreasing film thickness or size of nanopores if there is no strong attractive interaction of polymers or small molecules with surrounding material, although there are some contradictory results [17–36]. As a typical example, Fig. 1 shows the $T_g$ of thin films of polystyrene (PS) supported on substrate, as measured by dielectric measurements and elipsometric measurements. In this figure, the $T_g$ of thin PS films decreases with decreasing film thickness regardless of the method of measurements. For physical origins for the depression of the $T_g$ there are several candidates such as surface or interfacial effects [38], confinement effects in thin film geometry [16], and so on. The physical origin has not yet been determined but is still in debate.

In addition to the glass transition of the single thin films, we here refer to the glass transition of stacked thin polymer films, where the stacked films consist of many ultrathin polymer layers, e.g., thin layers with thickness of about 10 nm and total thickness on the micrometer scale, that is, the thickness of bulk films. For such stacked thin films, we question whether the glass transition behavior for the stacked thin polymer films has thin-film-like properties or bulk-like properties. An answer to this question can be found in the literature. The glass transitions of stacked thin films have been investigated using differential scanning calorimetry (DSC) by Simon and coworkers [39, 40]. The glass transition temperature $T_g$ of stacked thin PS films is dependent on the thickness of the single layers of the stacked thin films, which is similar to that for single thin polymer films. Furthermore, $T_g$ is increased by annealing above $T_g$ and approaches that of the bulk system, which suggests that stacked thin films prepared by an appropriate method can maintain the thin-film properties of the glass transition dynamics. This result suggests that the existence of an interface between thin polymer layers can decrease the $T_g$ and, hence, the interfacial interaction can control the depression of $T_g$.

## 1.2 Aging Phenomena of Polymer Glasses

As mentioned in the above, the molecular mobility due to the $\alpha$-process is almost lost in the glassy state [1] because the characteristic time of the $\alpha$-process becomes macroscopic below $T_g$. In polymeric systems, segmental motion is the microscopic origin of the $\alpha$-process [41] and this motion is almost frozen in the glassy states. However, even in the glassy state there is a very slow change in the structure and dynamics when approaching an equilibrium state, and this phenomenon is known as physical aging [42]. Several interesting phenomena, including memory and rejuvenation effects, occur during physical aging [42–44]. These effects are frequently observed in many disordered systems, including polymer glasses [45–50], spin glasses [51–54] and other disordered systems [55–57].

We have previously investigated the aging dynamics in polymer glasses of poly (methyl methacrylate) (PMMA) [47–49], PS [58, 59], and poly(2-chlorostyrene) (P2CS) [60] using DRS and temperature-modulated DSC. In PMMA, the real and imaginary parts of dielectric susceptibility, $\varepsilon'$ and $\varepsilon''$, decrease with increasing aging time for isothermal aging. This result is consistent with the idea that the non-equilibrium glassy state approaches an equilibrium state. An example of the memory and rejuvenation effects of the dielectric susceptibility for the aging dynamics observed in PMMA are shown in Fig. 2.

Figure 2 shows the time evolution of dielectric susceptibility for the thermal history, which consists of the series of the three isothermal annealing processes at the temperatures $T_1$, $T_2$, and $T_1$ for times $\tau_1$, $\tau_2$, and $\tau_3$, respectively. This thermal history is called temperature cycling mode (TC mode). Here, the value of $T_2$ is set to be lower than that of $T_1$. Figure 2 shows the time dependence of $\varepsilon'' - \varepsilon''_{\mathrm{ref}}$ for PMMA thin films with the thickness $d = 26$ nm, $T_1 = 374.2$ K, $T_2 = 354.6$ K, and $\Delta T \equiv T_1 - T_2 = -19.6$ K. The origin of the time ($t_w = 0$) is defined as the time when the temperature reaches $T_1$ after cooling from 403 K (above $T_g$). The value of $\varepsilon''_{\mathrm{ref}}$ is the reference value of $\varepsilon''$ for each aging temperature ($T_1$ or $T_2$). In this case, the value of $\varepsilon''_{\mathrm{ref}}$ for $T_1$ ($T_2$) is the initial value of $\varepsilon''$ obtained at the time when the temperature reaches $T_1$ ($T_2$) directly from 403 K. As the aging time $t_w$ increases from 0, $\varepsilon'' - \varepsilon''_{\mathrm{ref}}$ decreases. This decrease in $\varepsilon''$ corresponds to aging. At $t_w = \tau_1$, the temperature is lowered from $T_1$ to $T_2$, and then $\varepsilon'' - \varepsilon''_{\mathrm{ref}}$ immediately changes to 0. This indicates that the decrease in temperature from $T_1$ to $T_2$ causes the polymer sample to rejuvenate. As the aging time elapses at $T_2$, $\varepsilon'' - \varepsilon''_{\mathrm{ref}}$ relaxes from 0, just as if a

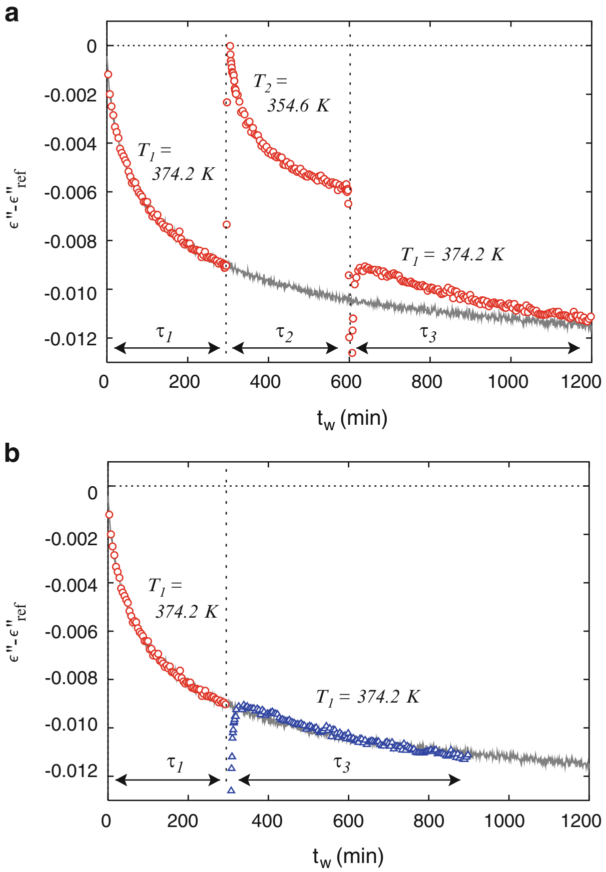

**Fig. 2** (**a**) Aging time dependence of the difference between $\varepsilon''$ and $\varepsilon''_{\text{ref}}$ observed by the TC mode with $T_1 = 374.2$ K and $T_2 = 354.6$ K ($\Delta T = -19.6$ K) for PMMA thin films with $d = 26$ nm. (**b**) The difference $\varepsilon'' - \varepsilon''_{\text{ref}}$ obtained by shifting the date points in the third stage in the negative direction of the time axis by $\tau_2$ after removing the data points in the second stage. Aging times at the first and second stages are $\tau_1 = \tau_2 = 5$ h. The *horizontal axis* of **b** is the total aging time at $T_1$. The *solid curve* is the standard relaxation curve obtained by isothermal aging at 374.2 K

new relaxation process starts at $t = \tau_1$. At $t_{\text{w}} = \tau_1 + \tau_2$, the system is heated up to $T_1$, and then the temperature of the system is kept at $T_1$. At this stage, $\varepsilon'' - \varepsilon''_{\text{ref}}$ goes back to the value that $\varepsilon'' - \varepsilon''_{\text{ref}}$ had reached at $t_{\text{w}} = \tau_1$ and then begins to decrease as if there were no temperature change during the aging process at $T_1$.

Figure 2b shows the time evolution of $\varepsilon'' - \varepsilon''_{\text{ref}}$ after removing the data between $\tau_1$ and $\tau_1 + \tau_2$ and shifting the data for $t_{\text{w}} > \tau_1 + \tau_2$ in the negative direction along the time axis by $\tau_2$. In this figure, we can see that $\varepsilon'' - \varepsilon''_{\text{ref}}$ decreases monotonically with the aging time without any discontinuous change, except for a short region just after $\tau_1$. The curve obtained in the above way agrees very well with the curve obtained by keeping the system at $T_1$ without any temperature change. This implies

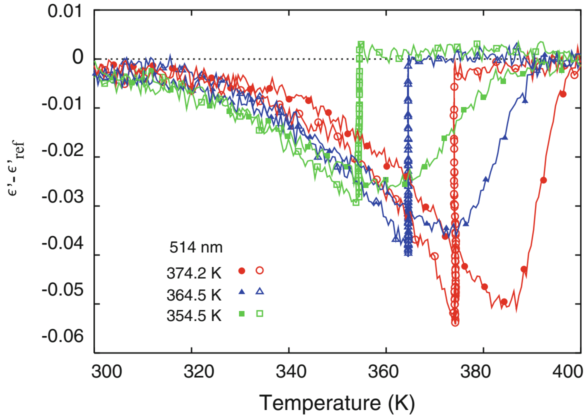

**Fig. 3** Temperature dependence of the difference between and $\varepsilon'$ and $\varepsilon'_{\mathrm{ref}}$ observed by CR mode with three different aging temperatures $T_{\mathrm{a}} = 374.2$, 364.5, and 354.5 K for PMMA films with $d = 514$ nm. The frequency of the applied electric field $f$ is 20 Hz. The heating and cooling rates were 0.5 K/min and the aging time at $T_{\mathrm{a}}$ was 10 h. *Open* and *filled symbols* display the data observed during the cooling and heating processes, respectively

that polymer glasses can remember the state at $t_{\mathrm{w}} = \tau_1$ of the relaxation towards the equilibrium state and recall the memory at $t_{\mathrm{w}} = \tau_1 + \tau_2$. In this case, we can say that there is a memory effect.

The memory and rejuvenation effects can also be observed for another thermal protocol, i.e., constant rate mode (CR mode). In the CR mode, two serial ramping processes between 273 and 403 K are carried out. The first process consists of cooling and heating processes at the rate of 0.5 K/min and this is defined as the reference process. The second process is the same to the first except for the addition of an isothermal aging process at a given temperature $T_{\mathrm{a}}$ ($T_{\mathrm{a}}$ is located below $T_{\mathrm{g}}$ of PMMA). The difference of the dielectric susceptibility between the first and second ramping process, $\varepsilon' - \varepsilon'_{\mathrm{ref}}$, is obtained as the effective contributions of isothermal aging to $\varepsilon'$. Figure 3 displays the temperature change in $\varepsilon' - \varepsilon'_{\mathrm{ref}}$ obtained by the CR mode with various aging temperatures $T_{\mathrm{a}}$ for $d = 514$ nm. In Fig. 3, it is found that, as the sample is cooled down from 403 K to $T_{\mathrm{a}}$, $\varepsilon'$ is almost equal to $\varepsilon'_{\mathrm{ref}}$ and the difference $\varepsilon' - \varepsilon'_{\mathrm{ref}}$ remains zero. The difference then begins to deviate from 0 to a negative value and the deviation becomes larger monotonically with increasing aging time during the subsequent isothermal aging at $T_{\mathrm{a}}$. This indicates that $\varepsilon'$ decreases with aging time at $T_{\mathrm{a}}$. As the temperature decreases from $T_{\mathrm{a}}$ to room temperature after the isothermal aging, the difference $\varepsilon' - \varepsilon'_{\mathrm{ref}}$ decreases with decreasing temperature and becomes almost zero at room temperature. Just after the temperature reaches 293 K, the heating process begins. As the temperature increases, the difference $\varepsilon' - \varepsilon'_{\mathrm{ref}}$ begins to deviate from 0 to a negative value almost in the same way as observed during the preceding cooling process. The difference between $\varepsilon'$ and $\varepsilon''_{\mathrm{ref}}$ exhibits a maximum at around $T_{\mathrm{a}} + 10$ K and then decreases to 0 with increasing temperature.

This behavior observed by the CR mode can be interpreted as follows: the thermal history that the sample is aged at $T_a$ for 10 h is memorized at $T_a$ during the cooling process. As the temperature decreases from $T_a$ to room temperature, the sample begins to rejuvenate and returns to almost a standard age at room temperature. During the subsequent heating process, the sample becomes older almost according to the curve along which the sample experienced rejuvenation during the preceding cooling process after a temporary stop at $T_a$. This result implies that not only the aging process at $T_a$ near $T_g$ but also the subsequent cooling process can be memorized and that the whole thermal history can be read out during the heating process.

The above two temperature protocols clearly show the existence of interesting memory and rejuvenation effects. As shown in Sect. 1.1, recent researches have shown that segmental motion, which is frozen in the glassy state, is strongly dependent on the film thickness [17, 26]. The value of $T_g$ decreases with decreasing film thickness and, accordingly, the dynamics of the $\alpha$-process, the segmental motion, become faster in thinner films [26, 27, 61, 62]. Therefore, it is very natural to expect that there should be a characteristic thickness dependence of the aging dynamics in thin polymer films. There have been several reports on the dependence of the aging dynamics on thickness [47, 63–66].

## *1.3 Heterogeneous and Aging Dynamics in Single and Stacked Thin Polymer Films*

As mentioned in Sects. 1.1 and 1.2, we developed our research on the glass transition of polymeric systems in two different ways. First, we investigated dielectric relaxation behavior of thin polymer films in order to elucidate how the glass transition dynamics change over the range from the liquid state to the supercooled liquid state near $T_g$ when the system size changes from bulk to nanometer scale in thin film geometry. Through this series of investigations, we could show the significant contributions of the surface and interfacial dynamics to the glass transition dynamics. Now, we have moved to investigation of the glass transition of stacked thin polymer films [67, 68]. Second, we investigated the aging dynamics of polymer glass below $T_g$ and showed the existence of common aging phenomena for polymer glass and spin glass. We have continued investigations into the nature of the memory and rejuvenation effects observed for the aging process and how the confinement in thin film geometry affects the aging dynamics [60, 69]. We believe that such investigations on the glass transition dynamics both from the liquid state to $T_g$ and from the glassy state to $T_g$ are important. A true understanding of the basic mechanism of the glass transition might not be obtained before the research from both the directions can be connected.

Here, we would like to show our recent results on the glass transition dynamics of stacked thin polymer films and the aging dynamics of ultrathin polymer films, as investigated by DSC and DRS. For both cases, heterogeneous dynamics such as the surface and interfacial dynamics play a crucial role in determining the characteristic features. Through the two different areas of research related to the heterogeneous dynamics, it can be expected that a clearer view of the glass transition can be obtained.

In this article, we present the experimental results on the glass transition and aging dynamics for single and stacked thin films of PS and P2CS, observed along the two different directions described above. After giving the experimental details in Sect. 2, the glass transition temperatures are given as a function of thickness for single thin films of P2CS in Sect. 3. Then, the glass transition dynamics of stacked thin films of P2CS are discussed in Sect. 4 and the aging dynamics of the ultrathin P2CS films are described in Sect. 5. Finally, a summary is given in Sect. 6.

## 2 Experiments

### 2.1 Sample Preparation

P2CS and PS used in this study were purchased from Polymer Source (Dorval, Quebec, Canada) and General Science, Co. Ltd., respectively. The weight-averaged molecular weight, $M_w$, and the molecular weight distribution ($M_w/M_n$, where $M_n$ is the number-averaged molecular weight) were $M_w = 3.3 \times 10^5$ and $M_w/M_n = 2.2$ for P2CS, and $M_w = 2.8 \times 10^5$ for PS. The structure of P2CS is similar to that of PS, except for the presence of a chlorine atom on the benzene ring. However, the polarity of P2CS is much greater than that of PS; therefore, P2CS can be regarded as an ideal system for the dielectric measurements.

Using spin-coating, we prepared single thin films of P2CS for dielectric measurements from a toluene solution on a glass substrate on which aluminum (Al) had been vacuum-deposited. The film thickness was controlled by varying the concentration of the solution. After annealing at 343 K under vacuum for 2 days to remove solvents, Al was again vacuum-deposited to serve as an upper electrode. The thickness was evaluated before measurements from the value of the electrical capacitance at 273 K for the as-prepared films in the manner previously reported [26, 27]. The absolute thickness was also obtained by direct measurement, using atomic force microscope.

Stacked thin films were prepared as described [67]. Single ultrathin films of various thickness were prepared on glass substrates by spin coating of a toluene solution. The film was floated onto the surface of water and transferred to the top of a substrate or a stack of polymer thin films on a substrate. This procedure, using ultrathin films with the same thickness, was repeated until the total number of stacked thin layers reached several hundred for the DSC measurements and ten layers for the dielectric measurements (see Tables 1 and 2). For the dielectric measurements, the first layer of P2CS was prepared directly onto an Al-deposited

**Table 1** Thickness of a single layer $d$, total weight, number of stacked layers, and $T_g$ (K) measured by DSC for stacked PS thin films prepared for the DSC measurements

| $d$ (nm) | Weight (mg) | No of layers | $T_g$ (K) |
|---|---|---|---|
| 70 | 0.623 | 73 | 369 |
| 55 | 0.528 | 100 | 364 |
| 40 | 0.611 | 130 | 361 |
| 20 | 0.786 | 224 | 353 |
| 13 | 0.899 | 400 | 350 |
| Bulk | 1.361 | 1 | 376 |

**Table 2** Thickness of a single layer $d$, number of stacked layers, isothermal annealing temperature $T_A$, and $T_g$ for stacked P2CS thin films prepared for the dielectric relaxation measurements

| $d$ (nm) | No. of layers | $T_A$ (K) | $T_g$[a] (K) |
|---|---|---|---|
| 18.5 | 10 | 425 | 381.0 |
| 15.4 | 10 | 416 | 380.1 |
| 10.0 | 10 | 412 | 378.6 |
| 9.6 | 10 | 422 | 378.5 |

[a] The value of $T_g$ is evaluated for a single thin film with thickness $d$, rather than the total stack thickness, from an approximation given by Eq. (3)

glass substrate and subsequent thin layers were prepared according to the above procedure. For the DSC measurements, a Teflon plate was used as a substrate. The stack of thin films, which consisted of several hundred thin layers, were detached from the Teflon substrate using a razor blade.

## 2.2 *Measurements for Stacked Thin Polymer Films*

DSC measurements were performed in order to determine the $T_g$ of the stacked PS thin films listed in Table 1. A commercial instrument (Q200, TA Instruments, New Castle, DE) was used for the measurements. The DSC run was firstly conducted for the heating process from 303 to 403 K at a rate of 10 K/min, and then for the cooling process down to 303 K at the same rate. The measurements were repeated three times to confirm reproducibility. The stacked samples used for the DSC measurements were then annealed at 523 K for 12 h in vacuo. Nitrogen gas was flowed at 30 mL/min during the DSC measurements.

Dielectric measurements were performed in order to investigate the dynamics of the $\alpha$-process of the stacked P2CS thin films listed in Table 2. An LCR meter (4284A, Agilent Technology, Santa Clara, CA) was used for the dielectric measurements. One measurement for the frequency $f$ range from 20 Hz to 1 MHz took approximately 50 s. Prior to the dielectric measurements, several heating and cooling processes through $T_g$ were conducted for stabilization of the measurements. Following that, the dielectric measurements were performed repeatedly for the following temperature cycles. One temperature cycle consists of two successive parts:

1. Cooling and heating processes between 433 and 273 K at a rate of 1 K/min were conducted twice.
2. After the ramping process, the temperature was changed from 433 K to $T_A$ (412–425 K) and was then kept at $T_A$ for 10 h (isothermal annealing at $T_A$).

These measurements showed that the two dielectric loss spectra observed successively in the temperature domain at a given frequency in part 1 agree with each other; therefore, the annealing effect for the ramping process 1 between 273 and 433 K was determined to be negligible compared with that for the isothermal annealing process. The annealing time $t_a$ can be well-defined by the total time for which the films remain at the annealing temperature $T_A$. Hence, $t_a$ for the $n$-th isothermal annealing cycle starts from $10 \times (n - 1)$ h.

## *2.3 Measurements of Aging Dynamics in Thin Polymer Films*

Dielectric measurements were carried out in the same experimental setup described in Sect. 2.2 for the ultrathin films of P2CS with thickness $d$ of 3.7, 5.4, 9.0, 9.5, and 22 nm, in order to investigate the aging dynamics below $T_g$. The complex dielectric constant $\varepsilon^*$ ($\equiv \varepsilon' - i\varepsilon''$) was evaluated as a function of temperature $T$, aging time $t_w$, and the frequency of applied electric field $f$. The value of $\varepsilon^*$ was obtained from the value of the complex electrical capacitance of the sample condenser $C^*$ ($\equiv C' - iC''$), on the assumption that $C^* = \varepsilon^* C_0$ is valid, where $C_0$ is the geometrical capacitance of the sample condenser.

For investigation of the aging dynamics, the following two temperature protocols were employed:

1. *Isothermal aging*: In this temperature protocol, the temperature was changed from a high temperature of 425 K (above $T_g$) to an aging temperature $T_a$ (below $T_g$), and then the temperature was maintained at $T_a$ for $t_a$ h.
2. *Constant-rate mode*: The temperature was decreased from 425 to 273 K at a constant rate of 1 K/min, and then increased from 273 to 425 K at the same rate. This is a simple constant-rate mode and we refer to this temperature change as the reference mode. In addition to the above thermal treatment, we included an intermittent stop at $T_a$ for $t_a$ h during cooling from 425 to 273 K. This temperature protocol is denoted as C($T_a$, $t_a$). According to this notation, the reference mode corresponds to the protocol C($T_a$, 0) for any value of $T_a$.

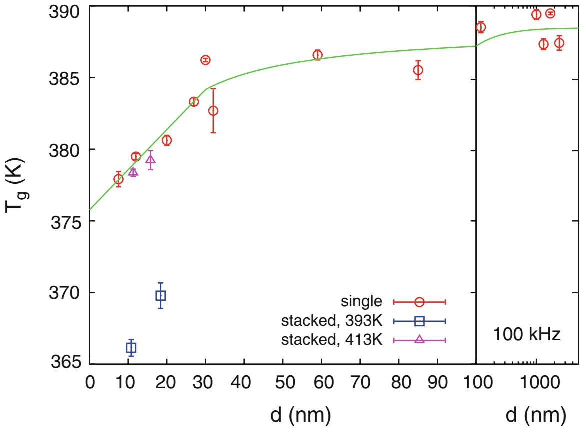

**Fig. 4** Thickness (*d*) dependence of $T_g$ for thin films of P2CS determined as a crossover temperature in the electric capacitance. *Circles* represent $T_g$ of the single thin films and the *squares and triangles* represent $T_g$ of the stacked thin films annealed at 393 and 413 K, respectively. In the latter case, *d* is the averaged thickness of each single layer within ten stacked thin films

## 3 Glass Transition Temperature of Thin P2CS Films

Before describing the results of glass transitions dynamics of stacked thin films and aging dynamics of the ultrathin P2CS films, the thickness dependence of $T_g$ of single thin films of P2CS supported on the Al-deposited glass substrate is shown in Fig. 4. The value of $T_g$ was determined from the measurements of the electric capacitance (dielectric constant) for the ramping process with a constant rate, in this case, at the rate of 1 K/min. As described previously [26, 27], the temperature coefficient of the real part of electric capacitance $C'$ observed for high frequency (i.e., 100 kHz) changes significantly through $T_g$, because the thermal expansion coefficient of the glassy state is much smaller than that of the liquid state. On the basis of this property, $T_g$ can be determined from the crossover temperature of $C'$ observed during the ramping process at a constant rate. Figure 4 clearly shows that $T_g$ of single thin P2CS films decreases with decreasing film thickness in a similar way as that observed for thin films of PS. The observed thickness dependence is given as follows [67]:

$$T_g(d) = \begin{cases} \Delta T_g(d - d_c) + T_{g,c} & : \quad d < d_c \\ T_{g,\infty} - \frac{d_c}{d}(T_{g,\infty} - T_{g,c}) & : \quad d > d_c, \end{cases} \tag{3}$$

where $\Delta T_g = 0.28 \pm 0.07$ K/nm, $d_c = 30 \pm 11$ nm, $T_{g,c} = 384.2 \pm 2.7$ K, and $T_{g,\infty} = 388.5 \pm 0.6$ K. The thickness of the as-prepared films was evaluated from electrical capacitance measured at 273 K, according to a previously reported procedure [26, 27]. It should be noted that the value of $T_g$ for bulk films is about 18 K higher for P2CS than for PS.

# 4 Glass Transition Dynamics of Stacked Thin Polymer Films

A similar measurement of $T_g$ has been performed for not only single thin films but also stacked thin films of P2CS [67]. The observed $T_g$ for stacked thin films is plotted in Fig. 4. In this figure, it is found that $T_g$ for stacked thin films of P2CS annealed at 393 K for 2 h (squares in Fig. 4) is located far below the bulk $T_g$ and at about 10 K below the $T_g$ of the single thin film with the same thickness ( circles in Fig. 4). This result suggests that the stacked thin films can keep the $T_g$ of the single thin films, even after stacking ten thin layers. In the case of PS thin films, it has been reported that the magnitude of the depression of $T_g$ of the freely standing films is larger by about 50 K than that of the supported thin films [37, 70]. If the magnitude of the depression of $T_g$ of the freely standing thin films of P2CS can obey the same law for PS, it is concluded that the $T_g$ of the stacked thin films of P2CS is located between the supported single thin films and the freely standing films. This result is consistent with the results observed for PS stacked thin films [40]. In Fig. 4, the value of $T_g$ of stacked P2CS thin films annealed at 413 K for 2 h is larger than for films annealed at 393 K and almost equal to the value of the single P2CS thin films with the corresponding thickness.

The above results can be summarized as follows: (1) the $T_g$ of single P2CS thin films was found to decrease with decreasing film thickness in a similar way to that observed for PS thin films [17, 26, 27]. The magnitude of the depression $\Delta T_g$, of $T_g$ for the stacked thin films from that for the bulk samples was larger than that for single thin films supported on a substrate. Here, the stacked thin films consist of ten layers of single thin films of 12–18 nm thickness. (2) Annealing could result in a decrease of $\Delta T_g$ for the stacked thin films.

## *4.1 Thermal Properties Determined by Differential Scanning Calorimetry*

In this section we will show the results on the DSC measurements for the stacked PS thin films. Figure 5 shows the temperature dependence of the total heat flow during the heating process at a rate of 10 K/min for stacked PS thin films with various single layer thicknesses, as listed in Table 1. Figure 5a shows an anomaly in the total heat flow around 350–380 K, which is associated with the glass transition of PS; the temperature at which the anomaly occurs can be regarded as $T_g$. Values of $T_g$, evaluated as the middle temperature of the anomalous region, are listed in Table 1. The $T_g$ for stacked PS films increases from 350 to 369 K with increasing single layer film thickness in the stacked thin films, even if the total thickness of the stacked thin polymer films is sufficiently large to nullify the dependence of $T_g$ on the thickness. The magnitude of the $T_g$ depression for the stacked thin films from

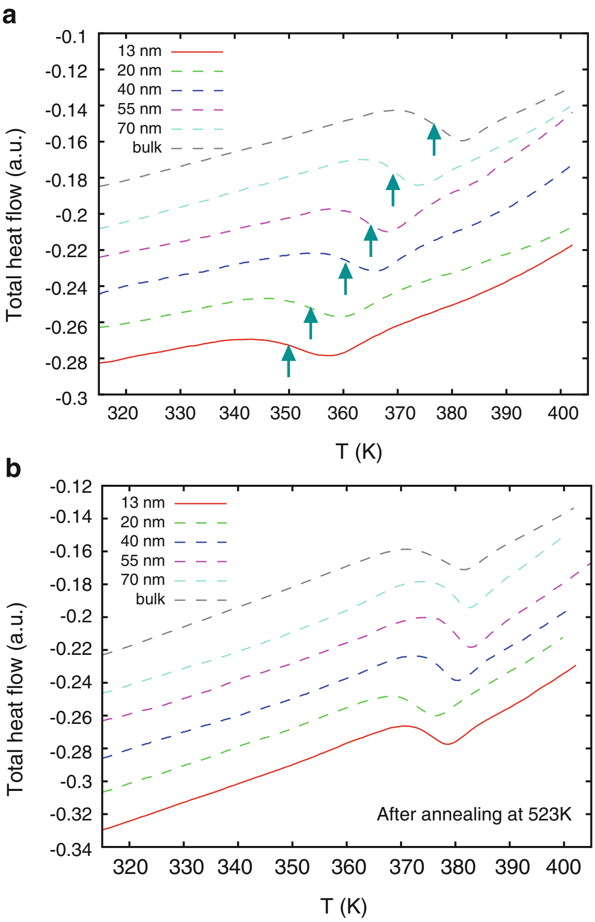

**Fig. 5** Temperature dependence of the total heat flow for stacked PS thin films with various single layer thicknesses, from 13 nm to that of the bulk value, during the heating process at a rate of 10 K/min. (**a**) As-stacked thin PS films, and (**b**) after annealing at 523 K for 12 h. Each *curve* is shifted slightly along the vertical axis for ease of comparison

that for the bulk is slightly larger than that for the single thin polymer film supported on a substrate [17, 26]. In contrast, the depression for the stacked thin films is smaller than that for the freely standing thin films [70]. This result for the $T_g$ of stacked thin films is consistent with that reported in the literature [39, 40] and with that measured by capacitance measurements for stacked P2CS thin films. as shown in Fig. 4.

Figure 5b shows the temperature dependence of the total heat flow observed after annealing at 523 K for 12 h in vacuo. The anomalous region, i.e., $T_g$, is located almost at the same position, regardless of the single layer thickness. The observed value of $T_g$ is approximately 376 K, which is almost equal to that for the bulk sample. This result suggests that $T_g$ of the stacked thin films increases and approaches the bulk $T_g$ after annealing at 523 K in vacuo. In other words, the bulk-like glass transition dynamics could be restored after annealing at high temperature for 12 h.

Annealing at high temperature diminishes the contrast at the interface between two thin layers, which suggests the possibility that the glass transition temperature could be controlled through interfacial interaction.

## *4.2 Evolution of Glass Transition Dynamics for Stacked Thin Films*

To demonstrate the effect of annealing on the glass transition dynamics of stacked P2CS thin films in more detail, in-situ dielectric measurements were performed during successive isothermal annealing processes at a given annealing temperature, $T_{\mathrm{A}}$. For these measurements several stacked thin films of P2CS were prepared, as listed in Table 2. The thickness of each single layer was between 9 and 18 nm, and the number of stacked layers for each sample for the dielectric measurements was 10. The annealing temperature ranged between 412 and 425 K.

### 4.2.1 Shift in the Dielectric Loss Peak Due to the $\alpha$-Process

Figure 6 shows the evolution of the dielectric loss spectra in the frequency domain observed for the successive isothermal annealing of stacked P2CS thin films of 18-nm thick layers. The dielectric loss $\varepsilon''$ versus frequency $f$ is plotted for various times $t_{\mathrm{a}} = 0$–173.4 h of isothermal annealing at 425 K. The dielectric loss peak due to the $\alpha$-process is located around $10^{3.6}$ Hz at $t_{\mathrm{a}} = 0$ h. The frequency at which the dielectric loss has a peak due to the $\alpha$-process is denoted by $f_{\alpha}$. The location of the peak $f_{\alpha}$ decreased down to $10^{2.3}$ Hz and the peak height increased with increasing annealing time, which suggests a slowing of the $\alpha$-process dynamics with an increase in annealing time.

As described in Sect. 2.2, two dielectric measurements in the temperature domain were conducted between two successive isothermal annealing processes for 10 h. The results suggest that there is no appreciable annealing effect of the ramping process between the repeated isothermal annealing processes for 10 h. The value of $f_{\alpha}$ for the isothermal annealing process was evaluated as a function of the annealing time $t_{\mathrm{a}}$ from the data presented in Fig. 6. Figure 7 shows the time evolution of $f_{\alpha}$ thus obtained for four different stacked thin films with varying thickness and annealing temperature.

Figure 7 shows that at the beginning of isothermal annealing, the frequencies $\log_{10} f_{\alpha}$ are located at 3.5, 3.3, 2.9, and 2.2 for $T_{\mathrm{A}} = 425$, 422, 416, and 412 K, respectively. At a given $T_{\mathrm{A}}$, the value of $f_{\alpha}$ for stacked thin films is higher than that observed for a single thin film with a thickness equal to that of a single layer in the stacked thin films. However, as the annealing time increases at a given $T_{\mathrm{A}}$, the value of $\log_{10} f_{\alpha}$ decreases monotonically down to 2.4, 1.9, 1.4, and 0.75 for $T_{\mathrm{A}} = 425$, 422, 416, and 412 K, respectively. The final values almost correspond to those

**Fig. 6** Evolution of $\varepsilon''$ spectra as a function of annealing time $t_a$ for the successive isothermal annealing of stacked P2CS thin films at 425 K. The thickness of each thin layer was 18 nm. The annealing times $t_a$ were 0, 3.4, 6.8, 10, 13.4, 16.8, 20, …, 173.4 h

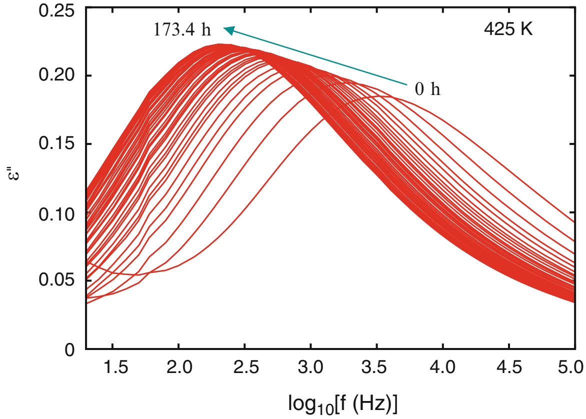

**Fig. 7** Dependence of $f_\alpha$ on the annealing time $t_a$ for successive isothermal annealing process at $T_A = 425$, 421, 416, and 412 K for stacked P2CS thin films, where the thickness of a single layer was 9–18 nm. The *solid curves* were calculated using Eq. (4)

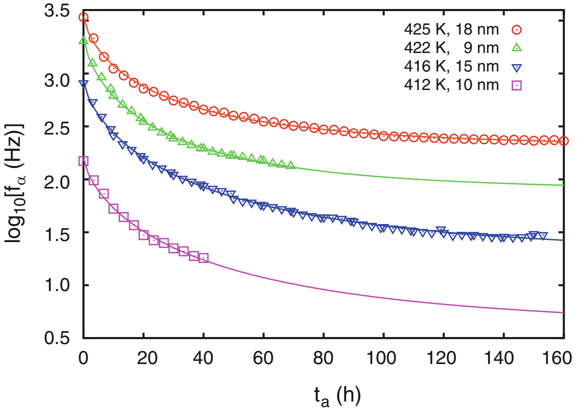

observed for single thin films with thicknesses almost equivalent to the total thickness of the stacked thin films (see Sect. 4.3.1 for the curve for single thin films with a thickness of 120 nm in Fig. 13.) This result suggests that the α-dynamics of the stacked thin films approach those of thicker films with thicknesses larger than 100 nm.

Figure 8 shows the dependence of $T_g$ on the annealing time. The $T_g$ values were determined in the temperature domain for the ramping process from measurements obtained between two successive isothermal annealing processes at $T_A = 425$ K for stacked thin films of 18-nm thick P2CS layers. The value of $T_g$ was determined in the same manner described in Sect. 3. Figure 8 shows that the $T_g$ of the stacked thin films increases with increase in the annealing time. When taking the value of $T_g$ for the heating process in Fig. 8, then at $t_a = 0$ the $T_g$ of the stacked thin films is much smaller than that for a single thin film of similar thickness ($T_g = 380.8$ K for $d = 18$ nm [67]), whereas $T_g$ at $t_a = 180$ h is almost equivalent to that for the bulk ($T_g = 387.8$ K for $d = 180$ nm [67]). Although there is a slight difference in

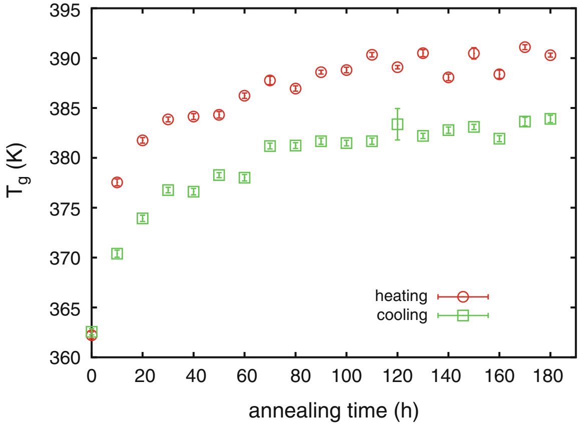

**Fig. 8** Dependence of $T_{\mathrm{g}}$ on the annealing time $t_{\mathrm{a}}$ observed for the ramping process in the temperature domain between two successive isothermal annealing processes for stacked thin films of 18-nm thick P2CS layers

$T_{\mathrm{g}}$ between the heating and cooling processes, as usually observed in other $T_{\mathrm{g}}$ measurements, the dependence of $f_\alpha$ on the annealing time for isothermal annealing is qualitatively consistent with the change in $T_{\mathrm{g}}$.

The time evolution of $f_\alpha$ and $T_{\mathrm{g}}$ in Figs. 7 and 8 suggests that there should be a change in the dynamics of the stacked thin films with a characteristic time scale of several tens of hours for isothermal annealing.

### 4.2.2 Time Evolution of $f_\alpha$

A slow change in $f_\alpha$ and $T_{\mathrm{g}}$ was observed during isothermal annealing of the stacked P2CS thin films. Here, we will investigate the dependence of $f_\alpha(t_{\mathrm{a}})$ on the annealing temperature and possibly on the thickness of the single layers of the stacked thin films. Figure 7 shows that the annealing time dependence of $f_\alpha$ observed during the isothermal annealing process can well be reproduced using the following equation:

$$\log_{10} f_\alpha(t_{\mathrm{a}}) = \log_{10} f_\alpha^\infty + (\log_{10} f_\alpha^0 - \log_{10} f_\alpha^\infty) \exp(-(t_{\mathrm{a}}/\tau)^n), \tag{4}$$

where $f_\alpha^0$ and $f_\alpha^\infty$ are the values of $f_\alpha$ at $t_{\mathrm{a}} = 0$ and $\infty$, $\tau$ is the characteristic time, and $n$ is the exponent of the stretched exponential function. The solid curves given in Fig. 7 are calculated using Eq. (4). The best fitting parameters are given in Table 3.

According to Eq. (4), the following scaling function can be obtained:

$$F_\alpha(\tilde{t}_{\mathrm{a}}) = \exp(-\tilde{t}_{\mathrm{a}}^n), \tag{5}$$

**Table 3** Values of $f_\alpha^\infty$, $f_\alpha^0$ and $\tau$ obtained by fitting the observed data using Eq. (4) for various annealing temperatures $T_A$ and the thickness of a single layer, $d$

| $T_A$ | $d$ | | | $\tau$ |
|---|---|---|---|---|
| (K) | (nm) | $\log_{10} f_\alpha^\infty$ | $\log_{10}(f_\alpha^0/f_\alpha^\infty)$ | (h) |
| 425 | 18.5 | 2.31 ± 0.01 | 1.22 ± 0.01 | 28.9 ± 0.7 |
| 422 | 9.6 | 1.90 ± 0.03 | 1.45 ± 0.02 | 28.0 ± 1.7 |
| 416 | 15.4 | 1.29 ± 0.01 | 1.65 ± 0.01 | 43.0 ± 1.2 |
| 412 | 10.0 | 0.6 ± 0.18 | 1.60 ± 0.17 | 45 ± 11 |

The exponent $n$ in Eq. (4) is fixed at 0.70

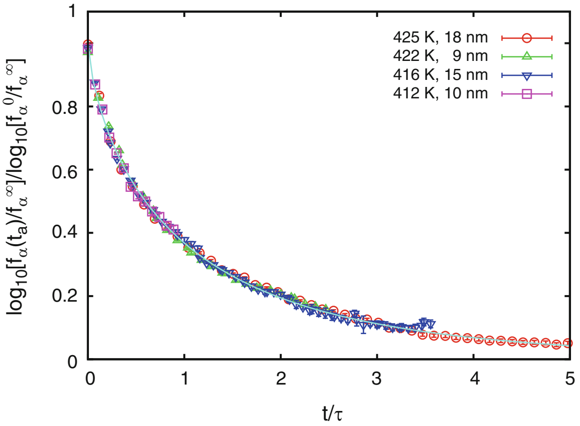

**Fig. 9** $F_\alpha(\tilde{t}_\alpha)$ vs. $\tilde{t}_a$ for stacked P2CS thin films for various values of $T_A$ and $d$. The *solid curve* is calculated using Eq. (5) with $n = 0.70 \pm 0.03$

where:

$$F_\alpha(\tilde{t}_a) \equiv \log_{10}\left(\frac{f_\alpha}{f_\alpha^\infty}\right) / \log_{10}\left(\frac{f_\alpha^0}{f_\alpha^\infty}\right), \tag{6}$$

$$\tilde{t}_a \equiv \frac{t_a}{\tau}. \tag{7}$$

In Fig. 9, all $f_\alpha(t_a)$ data are plotted after scaling via $F_\alpha(\tilde{t}_a)$ using Eqs. (6) and (7). Figure 9 shows that the time evolution of the $\alpha$-peak frequency $f_\alpha$, can well be reduced to a single master curve for various values of $T_A$ (and $d$). Therefore, we can expect that the observed time dependence of $f_\alpha$ can be controlled by a common mechanism, regardless of $T_A$ and $d$. Furthermore, the exponent of Eq. (5) is given by the following relation: $n = 0.70 \pm 0.03$. Therefore, a single exponential function could be a good approximation for this slow changing process.

Figure 10 shows the characteristic time $\tau$ for the change in the $\alpha$-peak frequency $f_\alpha$ for this process observed during isothermal annealing at $T_A$. The characteristic time $\tau$ increases with decreasing annealing temperature. It should be noted that there is an ambiguity in determining the temperature dependence of $\tau$, due to the small number of observed points. Nevertheless, if we assume that the temperature

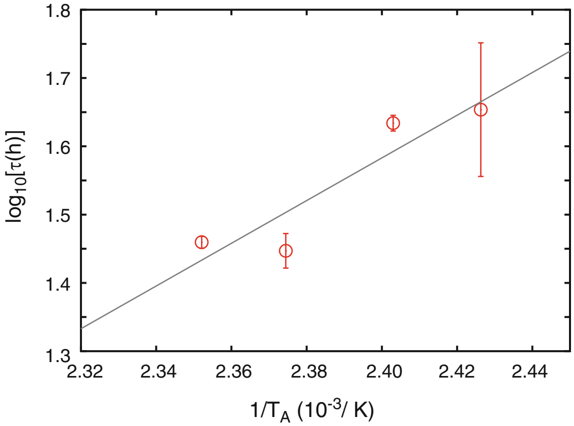

**Fig. 10** Arrhenius plot of $\tau$ as a function of $T_A$ for stacked P2CS thin films with various values of $T_A$ and single layer thicknesses $d$ of 9.6–18.5 nm

dependence of $\tau$ is given by $\tau(T_A) = \tau_0\ \exp(U/T_A)$ (where $\tau_0$ and $U$ are the constants), then a straight line can be obtained in Fig. 10 with the parameter $U = 6.2 \pm 1.9$ kcal/mol. This activation energy is much smaller than that of the common value for the $\beta$-process of PS ($U \sim 35$ kcal/mol) [71].

### 4.2.3 Diffusion of Polymer Chains

A change in the contrast at the interface between two neighboring layers is expected to occur during the isothermal annealing process. With increasing annealing time, the contrast decreases and, as a result, the morphology of the stacked thin film approaches that of the bulk film. It is clear that the diffusion of polymer chains is promoted during isothermal annealing, and the polymer chain undergoes interdiffusion between neighboring layers [72]. However, there is a question here as to whether the observed change is due solely to chain diffusion.

In order to answer this question, we estimated the chain diffusion during isothermal annealing. The temperature dependence of the diffusion constants measured using secondary ion mass spectroscopy was reported for PS by Whitlow and Wool [72]. From these measurements, we have estimated the diffusion length of P2CS for isothermal annealing at $T_A$, as shown in Table 4. The $T_g$ for the bulk is 388.5 K for P2CS [67] and 370.5 K for PS [26], so that the difference in $T_g$ is $\Delta T_g = 18.0$ K. Therefore, the temperature dependence of the self-diffusion constant of P2CS, $D_{P2CS}(T)$, was evaluated from that of PS, $D_{PS}(T)$, reported in [72] using the relation $D_{P2CS}(T) = D_{PS}(T - 18.0\ \text{K})$. The values of $D_{P2CS}$ for isothermal annealing at $T_A = 425$ and 412 K are given in Table 4. From $D_{P2CS}$, the diffusion length $\ell_{diff}$ was also evaluated for 10 h annealing at $T_A$. Table 4 shows that the diffusion length of P2CS is 57 nm for annealing at 425 K for 10 h. This length is much larger than the thickness of a single thin layer ($d = 18$ nm), even for isothermal annealing for 10 h. Therefore, it is expected that the polymer chains have

**Table 4** Diffusion constant $D_{\mathrm{P2CS}}$ and diffusion length $\ell_{\mathrm{diff}}$ at two annealing temperatures for stacked P2CS thin films

| $T_A$ | $D_{\mathrm{P2CS}}$ [a] | $\ell_{\mathrm{diff}}$ [b] |
|---|---|---|
| (K) | (cm$^2$/s) | (nm) |
| 425 | $9.0 \times 10^{-16}$ | 57 |
| 412 | $1.4 \times 10^{-16}$ | 22 |

[a] $D_{\mathrm{P2CS}}$ is evaluated from that of PS reported in [72]

[b] $\ell_{\mathrm{diff}}$ is the diffusion length for isothermal annealing at $T_A$ for 10 h

already reached from one interface to the neighboring interface, while the evolution of $T_g$ and $f_\alpha$ still continues. However, this may be an unrealistic situation.

There could be two possible reasons for this apparently contradictory situation,. First, in the above discussion, we adopted a diffusion constant that was evaluated from the diffusion constant of polymer chains at the interface between two bulk polymeric layers [72]. Recent measurements have revealed the existence of heterogeneous dynamics in confined geometries such as thin films and nanopores [73, 74]. For stacked thin films of polymers, the dynamics vary with an essential dependence on the distance of the layer of interest from the free surface or from the substrate [75]. If such dynamical heterogeneity is taken into account, the diffusion of polymer chains could be restricted by the existence of an immobile region.

Second, the interface between the two polymer layers of as-stacked thin films may not be sufficiently smooth for good contact between the two layers. In this case, the diffusion of polymer chains between the two thin layers would be limited by the quality of the contact between the surfaces of the two thin layers. It has been reported that the area of indentation increases approximately with the logarithm of time for the contact of two solid surfaces. This observation is related to the change in the quality of contact [76, 77]. As a result, the interface between two thin layers could exhibit a very slow temporal change, as shown in the present measurements.

## 4.3 Dynamics of the α-Process for Stacked P2CS Thin Films

In this section, the time evolution of dielectric loss spectra for the isothermal annealing process as a function of annealing time $t_a$ is discussed to elucidate how the dynamics of the α-process change an increase in annealing time $t_a$.

### 4.3.1 Shape of the Dielectric Spectra

Figure 11 shows the frequency dependence of the dielectric loss, normalized with respect to the peak position and height of the α-process, for four different annealing times during the isothermal annealing at $T_A = 425$ K for stacked thin films of 18-nm thick P2CS layers. The dielectric loss data in the frequency domain at

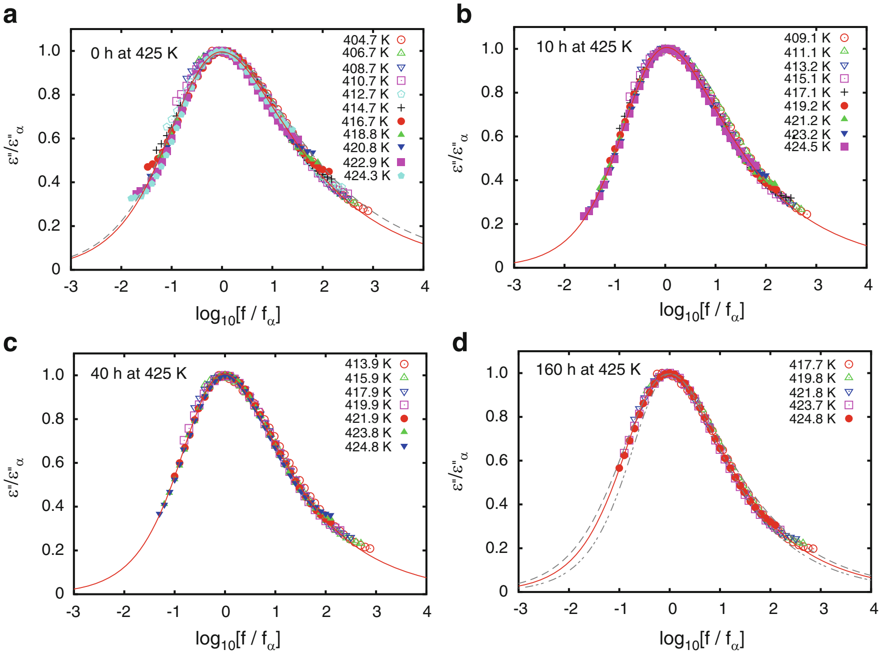

**Fig. 11** Time evolution of dielectric loss spectra normalized with respect to the position of the α-process for isothermal annealing of stacked 18-nm thick P2CS thin films at $T_A = 425$ K. The annealing times were (**a**) 0, (**b**) 10, (**c**) 40, and (**d**) 160 h. The *solid curves* were obtained by fitting the normalized data for the stacked thin films to Eq. (8). The *dashed curves* in **a** and **d** were calculated from the fitting parameters for single thin films of P2CS with thicknesses of 20 and 120 nm, respectively. The *dot-dashed curve* in **d** is that for stacked thin films with a thickness of 1,680 nm

various temperatures and at a given annealing time $t_a = 10n$ ($n$ is a positive integer) are extracted from the data measured for the heating process (1) between the ($n - 1$)-th and $n$-th isothermal annealing processes (see details in Sect. 2.2). The normalized data shows that the superposition with respect to the position of the α-process does correspond well for the temperature range 405– 425 K, so that a master curve can be obtained.

As shown in Fig. 11, a master curve for the dielectric loss spectra becomes narrower with increasing annealing time for the isothermal annealing process. For comparison, the dielectric loss spectra of single thin P2CS films with thicknesses of 20, 120, and 1,680 nm are given in Fig. 11a, d. This tendency in the stacked thin films is quite similar to that observed for the single thin P2CS films with increasing film thickness. Here, it should be noted that there is a slight deviation from the master curve at $t_a = 0$ h. The slight deviation is consistent with the existence of heterogeneity in the thin film geometry [27, 78].

**Fig. 12** Annealing time dependence of the shape parameters, $\alpha_{\mathrm{HN}}$ and $\beta_{\mathrm{HN}}$, from the HN equation, and the stretching exponent of the KWW equation, $\beta_{\mathrm{K}}$, for isothermal annealing at 425 K. The values of $\beta_{\mathrm{K}}$ are evaluated using Eq. (9). The corresponding values for single P2CS thin films with thicknesses of 20 (plotted at $t_{\mathrm{a}} = 0$), 120, and 1,680 nm (plotted at $t_{\mathrm{a}} = 180$ h) are also presented for comparison

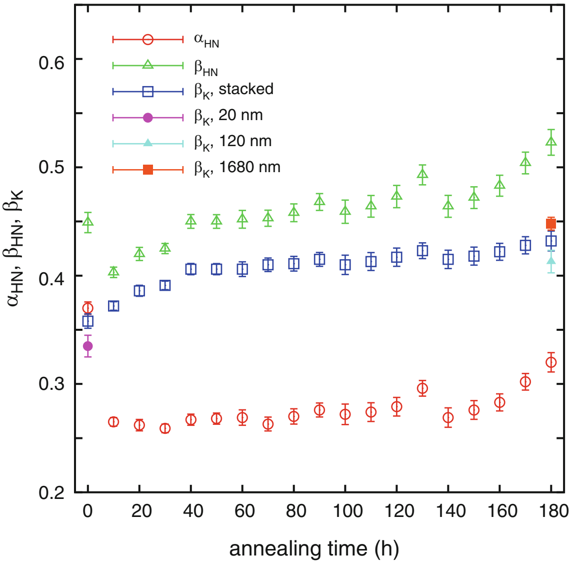

Furthermore, in order to observe this narrowing of the dielectric spectra more quantitatively, the dielectric spectra were fitted in terms of the Havriliak–Negami (HN) equation:

$$\varepsilon^*(f) = \frac{\Delta\varepsilon}{\left(1 + (i2\pi f \tau_{\mathrm{HN}})^{1-\alpha_{\mathrm{HN}}}\right)^{\beta_{\mathrm{HN}}}}, \tag{8}$$

where $\tau_{\mathrm{HN}}$ is the relaxation time, $\Delta\varepsilon$ is the relaxation strength, and $\alpha_{\mathrm{HN}}$ and $\beta_{\mathrm{HN}}$ are the shape parameters [79]. As shown by the solid curves in Fig. 11, Eq. (8) reproduces the observed master curves well at all annealing times.

Figure 12 shows the shape parameters, $\alpha_{\mathrm{HN}}$ and $\beta_{\mathrm{HN}}$, of Eq. (8) as a function of annealing time for stacked thin films of 18-nm thick P2CS layers. Both parameters increase with increasing annealing time for isothermal annealing at 425 K. Furthermore, using the $\alpha_{\mathrm{HN}}$ and $\beta_{\mathrm{HN}}$ fitting parameters, the stretching parameter $\beta_{\mathrm{K}}$ of the Kohlrausch–Williams–Watts equation (KWW) can also be evaluated as a measure of the broadening of the relaxation time distribution [12]. See the relaxation function given by Eq. (2), where $\phi(t)$ is the relaxation function of the fluctuational correlation of dipole moments in the case of dielectric relaxation. There is an empirical relation between the $\alpha_{\mathrm{HN}}$, $\beta_{\mathrm{HN}}$, and $\beta_{\mathrm{K}}$ parameters, as follows [80]:

$$\beta_{\mathrm{K}} = \left[(1 - \alpha_{\mathrm{HN}})\beta_{\mathrm{HN}}\right]^{1/1.23}. \tag{9}$$

Using Eq. (9), the $\beta_{\mathrm{K}}$ stretching parameters can be evaluated and are found to increase with increase in the annealing time, as shown by the open square symbols

**Fig. 13** Dispersion map for the α-process of both single thin films and stacked thin films of P2CS. For stacked thin films of 18-nm thick P2CS layers, the temperature dependence of $f_\alpha$ at various annealing times $t_a = 0$–160 h are plotted. The results for single thin films with thicknesses of 20 and 120 nm are also plotted

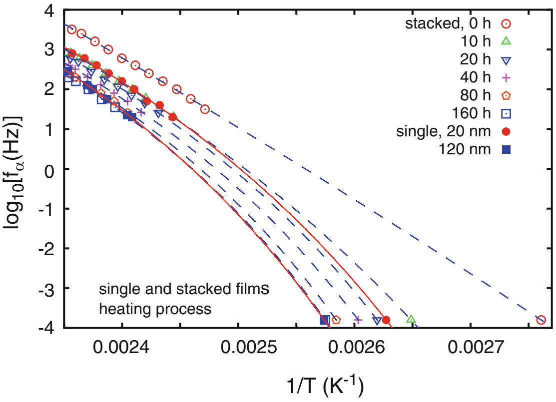

in Fig. 12. In other words, the shape of the dielectric loss spectra becomes sharper with an increase in the isothermal annealing time.

### 4.3.2 Non-Arrhenius Behavior of the α-Process

In order to interpret the present results both on $T_g$ and $f_\alpha$, a dispersion map of the α-process was constructed for stacked thin films of 18-nm thick P2CS layers. Figure 13 shows the data observed for single thin P2CS films with thicknesses of 20 and 120 nm, together with the results for stacked thin films. Here, the values of $f_\alpha$ are plotted for the temperature range of 400–425 K. Furthermore, the value of $T_g$ for a given annealing time is also plotted as the point $(1/T_g, 1/2\pi\tau_g)$, where the characteristic time of the α-process at $T_g$, $\tau_g$, is assumed to be $10^3$ s.

Comparison of the temperature and annealing time dependence of the relaxation times for the α-process of stacked thin films of P2CS with those for single thin films of P2CS shows that the relaxation rate of the α-process, $f_\alpha$, becomes smaller with increasing annealing time for the stacked thin films. Furthermore, the relaxation rate for the stacked thin films at $t_a = 0$ is larger than that for a single thin film with a thickness of 20 nm, and $f_\alpha$ approaches that for the single thin film with a thickness of 120 nm with increasing annealing time. It is also noticed that for as-stacked thin films, the temperature dependence of the relaxation rate for the α-process can be well described by an Arrhenius-type temperature dependence, whereas non-Arrhenius behavior becomes more pronounced with increasing annealing times. The curves in Fig. 13 are given by Eq. (1), where $f_\alpha = 1/2\pi\tau_\alpha$. Figure 13 shows that Eq. (1) can reproduce the observed temperature dependence of the relaxation rate of the α-process well for the isothermal annealing process. The Vogel temperature $T_0$ increases with increasing annealing time, in accordance with the increase in $T_g$ for the isothermal annealing process of stacked thin films [67, 68].

**Fig. 14** Dependence of the fragility index *m* on the annealing time for annealing at 425 K of stacked thin films of 18-nm thick P2CS layers. The fragility indices for single thin films with thicknesses of 12, 120, and 1,680 nm are also plotted

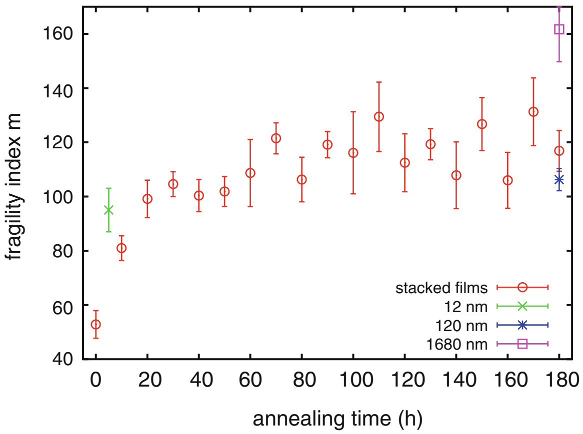

In order to evaluate the non-Arrhenius behavior in more detail, the fragility index *m* is evaluated according to the following equation for the temperature dependence of the α-relaxation times [81]:

$$m = \left[ \frac{d \log_{10} \tau_\alpha(T)}{d(T/T_g)} \right]_{T=T_g}. \tag{10}$$

Figure 14 shows that the fragility index *m* increases with increase in the annealing time at $T_A = 425$ K. The glassy dynamics of the stacked thin films change from less fragile to more fragile for the isothermal annealing process. The interlayer interaction within the stacked thin films of P2CS may influence the fragility of polymeric systems, because the contrast at the interface decreases with increasing annealing time.

On the basis of the present measurements, we can say that both *m* and $\beta_K$ increase with increasing annealing time for stacked thin films of P2CS. There should be a positive correlation between *m* and $\beta_K$, which is totally different from that observed for conventional glassy systems [82, 83]. However, a similar positive relationship between *m* and $\beta_K$ was reported for the thin film geometry of PS [61]. The origin of the dynamical heterogeneity has two parts: one is an intrinsic heterogeneity related to the α-process, even in the bulk, and the other is heterogeneity induced by the geometrical restriction in thin films. The value of $\beta_K$ is determined by both factors in the case of thin polymer films and, accordingly, this leads to a different relationship between $\beta_K$ and *m*.

Recently, the fragility index of freely standing PS films has been observed by DRS and was found to decrease with decreasing film thickness down to the monomer limit [84]. The decrease in fragility index was attributed to an increase in the fraction of free surfaces in freely standing films. Comparing the present result with that of freely standing films, it should be noted that the increase in the fragility index for isothermal annealing of stacked thin polymer films might correspond to the increase in fragility index for the increase in film thickness in freely standing films. Therefore, the interface between stacked layers can play a crucial role, similar to the free surface of freely standing films, as long as the non-Arrhenius temperature dependence of the $\alpha$-relaxation time, i.e., fragility index is concerned.

### 4.4 Remarks on the Glass Transition Dynamics of Stacked Thin Films

The glass transition behavior of stacked layers of thin films of PS and P2CS was investigated using DSC and DRS. The results obtained can be summarized as follows:

1. Stacked thin films exhibit glass transition dynamics that are similar to those observed for single thin films. The $T_g$ of as-stacked thin films is lower than that of the single thin supported films with the same thickness as that of a single layer in the stacked thin films, and is higher than that of freely standing films.
2. Isothermal annealing can change the $T_g$ and the dynamics of stacked thin films from thin film-like dynamics to bulk-like dynamics.
3. The characteristic time for evolution of the $\alpha$-dynamics for stacked thin films is very large compared with the reptation time of polymer chains.
4. The relation between non-exponentiality and fragility for stacked thin films is different from that of conventional glassy systems.

In Sect. 4.2, the shift in the peak frequency of the dielectric loss due to the $\alpha$-process was discussed. However, in Fig. 6, an increase in the relaxation strength, i.e., the area below the $\alpha$-relaxation peak can also be observed with increase in the annealing time. The peak height in $\varepsilon''$ increases by 19.5% when the annealing time changed from 0 to 173.4 h. The value of $\varepsilon''$ plotted in Fig. 6 was not corrected for any variation in film thickness due to isothermal annealing. The variation in film thickness was found to contribute to the apparent increase in $\varepsilon''$ by 6.3% from the analysis of the real part of electric capacitance at 273 K and 100 kHz for both $t_a = 0$ h and 173.4 h. Therefore, there should be an intrinsic increase in $\varepsilon''$ during the isothermal annealing process. It has been reported that the relaxation strength of the $\alpha$-process of the ultrathin films is smaller than that of the bulk [85]. A possible origin of this increase in $\varepsilon''$ observed for the annealing of the stacked thin films may be associated with the reduction in the relaxation strength of the single ultrathin polymer films. The detailed investigation of variation of the dielectric relaxation strength for P2CS and PS is now still in progress in order to elucidate the origin of the increase with annealing time.

It was discussed in Sect. 4.2 that there is a very slow change in the $\alpha$-dynamics in stacked thin films of P2CS. There may be several possibilities for this slow change. If heterogeneous diffusion in thin polymer layers is an essential process, then direct measurement of diffusion constant of a tracer polymer chain in a thin layer of the stacked thin film is required. Recently, an alternative measurement of the diffusion constant of a polymer chain has been proposed [74]. Such measurements could be applicable for the present case.

If the change in the quality of the contact surface is associated with the observed phenomena, similar measurements performed under external stress are required to elucidate the strong stress dependence of the time evolution of the $\alpha$-dynamics observed in stacked thin films.

Although there are many issues to be clarified, the present measurements provide clear evidence that a change in interfacial interaction is directly associated with the change in the glass transition dynamics for isothermal annealing processes.

## 5 Aging Dynamics in Ultrathin P2CS Films

In the previous section, we have shown the experimental results on the glass transition dynamics above $T_g$, and here we move to the aging dynamics below $T_g$. In this section, we will discuss the second main topic, i.e., the aging dynamics of the ultrathin films of P2CS. The aging time dependence of the dielectric loss $\varepsilon''$ relative to the value $\varepsilon''_{\rm ref}$ is shown, as an example, in Fig. 15 for P2CS thin films undergoing isothermal aging at $T_a = 329$ K, where $\Delta T_a \equiv T_g - T_a = 52.9$ K. The value of $\varepsilon''_{\rm ref}$ is $\varepsilon''$ at $t_w = 0$. This figure shows that $\varepsilon''$ decreases with increasing aging time, which is consistent with the results observed for PMMA thin films [45, 47]. The system approaches an equilibrium state during isothermal aging, even in the glassy state, so that the dielectric constant changes slowly with aging time. The aging time $t_w$ dependence of $\varepsilon''$ can be fitted to the equation:

$$\varepsilon''(t_w; f, T_a) = \frac{\Delta\varepsilon}{\left(1 + \frac{t_w}{t_0}\right)^n} + \varepsilon''(\infty; f, T_a), \tag{11}$$

where $\Delta\varepsilon$ is the relaxation strength towards the equilibrium value, $t_0$ is the characteristic time of the aging dynamics, and $n$ is an exponent [47]. This relation can be applied to relatively thick films. The $t_w$ dependence for thinner films is different from this and is discussed later.

Figure 16 shows the $t_w$ dependence of $\varepsilon''$ for P2CS thin films of thickness $d = 22$, 9.0, and 3.7 nm and for two different aging temperatures $T_a$ of 348 and 310 K. The frequency of the applied electric field was 200 Hz. In Fig. 16a, the value of $\varepsilon''$ decreases with increasing aging time at $T_a = 348$ K, except for the initial stage of thin films with $d = 3.7$ nm. However, the value of $\varepsilon''$ clearly increases for isothermal aging at $T_a = 310$ K in the P2CS thin films with $d = 3.7$ and 9.0 nm. These results suggest that the $t_w$ dependence of $\varepsilon''$ is strongly dependent on the

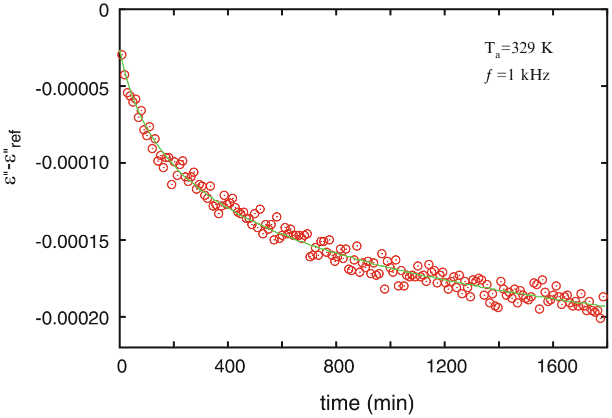

**Fig. 15** Aging time dependence of $\varepsilon'' - \varepsilon''_{\mathrm{ref}}$ for P2CS thin films with $d = 22$ nm, $f = 1$ kHz, and $T_{\mathrm{a}} = 329$ K. The *solid line* is fitted using Eq. (11), where $\Delta\varepsilon = 0.0082$, $t_0 = 62$ min, and $n = 0.07$

thickness and aging temperature. For thin films with $d = 3.7$ nm, $\varepsilon''$ monotonically increases with increasing aging time at a lower aging temperature $T_{\mathrm{a}}$ (310 K), while $\varepsilon''$ shows a maximum against the aging time for $T_{\mathrm{a}} = 348$ K. The latter result suggests that there are two competing physical origins with different time scales. Figure 16c shows how the aging time dependence of $\varepsilon'' - \varepsilon''_{\mathrm{ref}}$ at isothermal aging at $T_{\mathrm{a}} = 348$ K for $d = 3.7$ nm can be decomposed into two competing (increasing and decreasing) components. Results of the detailed analyses are shown in Sect. 5.2.

Figure 17 shows the temperature dependence of the imaginary part of the dielectric constant $\varepsilon''$ relative to the reference value $\varepsilon''_{\mathrm{ref}}$ for the cooling process, including isothermal aging for 30 h, which is observed for the CR mode denoted by the protocol C($T_{\mathrm{a}}$, $t_{\mathrm{a}} = 30$ h). Here, the values of $\varepsilon''_{\mathrm{ref}}(f, T)$ have been measured during the heating and cooling processes at a rate of 1 K/min without any isothermal aging, i.e., the protocol C($T_{\mathrm{a}}$, 0). For each temperature, the deviation $\varepsilon''(f, T) - \varepsilon''_{\mathrm{ref}}(f, T)$ was evaluated. Figure 17 shows that $\varepsilon''$ increases with increasing aging time $t_{\mathrm{w}}$ for isothermal aging at various aging temperatures, $T_{\mathrm{a}}$, which corresponds to the increase in $\varepsilon''$ observed in Fig. 16. The deviation of $\varepsilon''$ from $\varepsilon''_{\mathrm{ref}}$ induced during the isothermal aging decreases with decreasing temperature for the subsequent cooling and $\varepsilon''$ approaches $\varepsilon''_{\mathrm{ref}}$. This temperature dependence shows that there is a rejuvenation effect, as reported for the glassy state in PMMA [45, 47]. Figure 17 shows that the amount of increase in $\varepsilon''$ induced during isothermal aging for 30 h is not a monotonic function of the aging temperature $T_{\mathrm{a}}$, but has a maximum at $T_a = 320$ K. The aging temperature dependence of the amount of deviation for ultrathin P2CS films is completely different from that for PMMA [45, 47], and also for thicker films of P2CS [60]. If there is only one dynamical mode associated with the aging phenomena, then the amount of deviation should be a monotonic function of the annealing temperature. Therefore, this annealing temperature dependence also suggests that there are two competing processes that have different temperature dependencies.

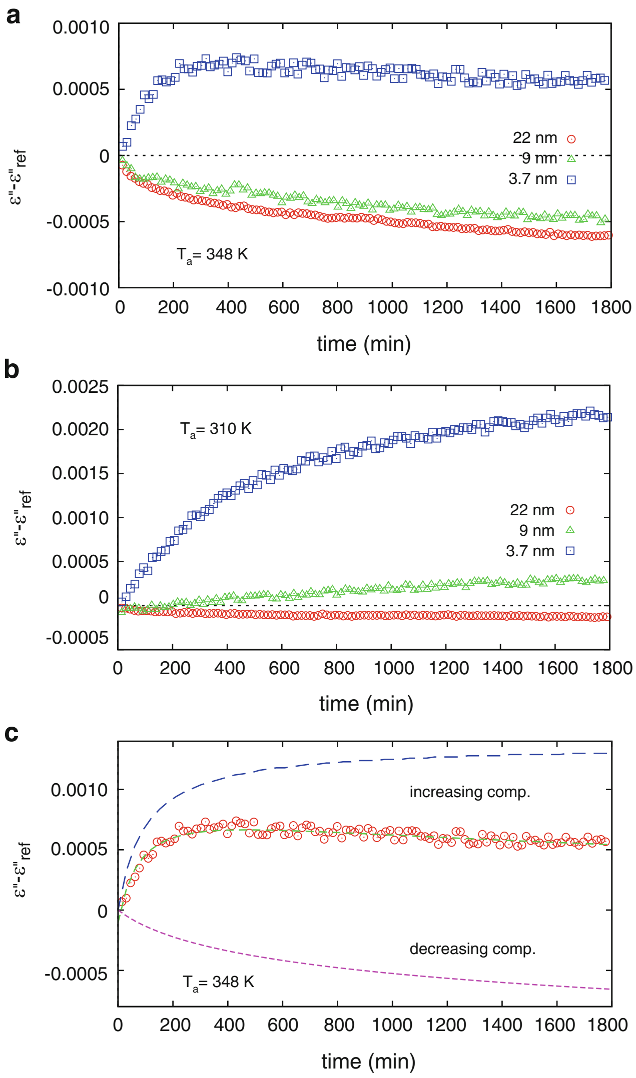

**Fig. 16** Aging time dependence of $\varepsilon'' - \varepsilon''_{\mathrm{ref}}$ for P2CS thin films with $d = 22$, 9.0 and 3.7, and $f = 200$ Hz for (**a**) $T_{\mathrm{a}} = 348$ K and (**b**) $T_{\mathrm{a}} = 310$ K. (**c**) Aging time dependence of $\varepsilon'' - \varepsilon''_{\mathrm{ref}}$ for thin films with $d = 3.7$ nm and $f = 200$ Hz, in addition to both the increasing component $\Delta\varepsilon''_{\mathrm{in}}$ (*dashed line*) and decreasing component $\Delta\varepsilon''_{\mathrm{dec}}$ (*dotted line*)

## *5.1 Segmental Dynamics in Ultrathin P2CS Films*

As discussed, the aging dynamics of ultrathin P2CS films are quite different from those of thicker films, and have an anomalous dependence on the thickness and temperature. Here, the microscopic origin for such an anomaly is discussed on the basis of segmental dynamics measurements using DRS.

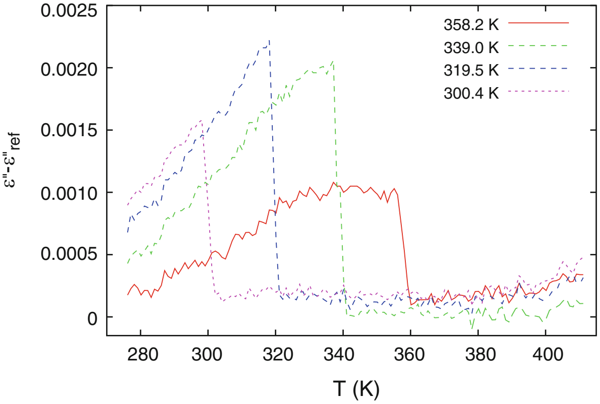

**Fig. 17** Temperature dependence of the $\varepsilon''$ deviation from the reference values for P2CS thin films with $d = 3.7$ nm observed during cooling, including isothermal aging at various $T_a$

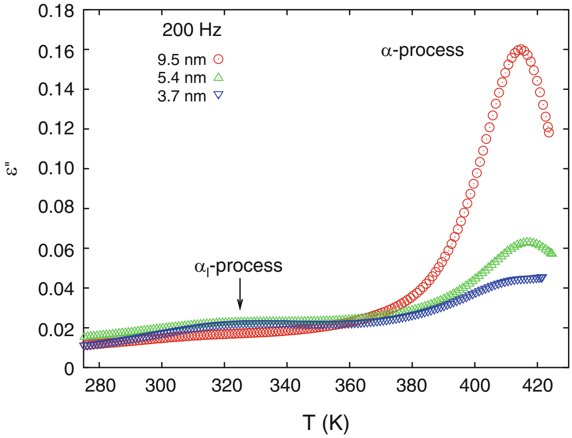

**Fig. 18** Temperature dependence of the imaginary part of the complex dielectric constant $\varepsilon''$ for $d = 9.5$ (*circles*), 5.4 (*triangles*) and 3.7 nm (*inverted triangles*). The data points in this figure were obtained for the cooling process at $f = 200$ Hz

In previous studies on PS thin films, $T_g$ decreased with decreasing film thickness, and the amount of decrease in $T_g$ was approximately 20 K when the film thickness was decreased from the bulk value to 10 nm [17]. Accordingly, the dynamics of the $\alpha$-process become faster in thinner films [26]. There are several physical reasons for the decrease in $T_g$ and the increase in the relaxation rate of the $\alpha$-process. One is the existence of a liquid-like layer with higher mobility near the free surface [38, 86]. Furthermore, the distribution of $T_g$ within thin films is also important for the overall dynamics in thin polymer films [30, 87, 88].

Figure 18 shows the temperature dependence of $\varepsilon''$ for the P2CS thin films with $d = 9.5$, 5.4, and 3.7 nm at 200 Hz. There is a loss peak due to the $\alpha$-process around

415 K and the peak height decreases with decreasing film thickness. In addition to this behavior, another process around 320 K is evident only for the $d = 3.7$ nm thin film. This peak of $\varepsilon''$ due to another process is also observed for thin films of both PS and PS labeled with the dye DR1 (disperse red one) [27, 78]. This extra loss peak was attributed to the segmental motion of a liquid-like layer near the surface or interface, which we have called the $\alpha_l$-process. The loss peak observed for ultrathin P2CS films may also be attributed to the $\alpha_l$-process. If the thickness of the liquid-like layer is independent of the overall thickness, then the contribution of the liquid-like layer becomes more appreciable as the thickness decreases. Figure 18 shows that the dielectric loss peak due to the $\alpha$-process is reduced and, accordingly, that of the $\alpha_l$-process becomes more appreciable as the film thickness is decreased to $d = 3.7$ nm.

Figure 19 shows the temperature dependence of $\varepsilon''$ for $d = 5.4$ nm obtained at three different frequencies of $f = 20$ Hz, 200 Hz, and 2 kHz. The peak due to the $\alpha_l$-process is shifted to the higher temperature side as $f$ is changed to higher frequency, which suggests that the loss peak around 300 K, the $\alpha_l$-process, has dynamical character. In order to analyze the observed dielectric loss, it is assumed that there are three contributions: the $\alpha$-process, $\alpha_l$-process, and conductivity components. Therefore, we describe the complex dielectric constant $\varepsilon^*$ as follows:

$$\varepsilon^*(f,T) = \sum_{i=\alpha,\alpha_l} \frac{\Delta\varepsilon_i}{\left(1 + (i2\pi f\tau_i)^{1-\alpha_i}\right)^{\beta_i}} + i\frac{\sigma}{\varepsilon_0(2\pi f)^{\gamma}}, \tag{12}$$

where the first terms on the right-hand side are contributions from the $\alpha$- and $\alpha_l$-processes, as described by the HN equations [79], $\Delta\varepsilon_i$ is the dielectric strength of the $i$-process, $\alpha_i$ and $\beta_i$ are the shape parameters, and $\tau_i$ is the relaxation time. $\tau_i$ can be described by the VFT law [9–11]:

$$\tau_i(T) = \tau_{0,i}\exp\left(\frac{T_{\mathrm{A},i}}{T - T_{\mathrm{V},i}}\right), \tag{13}$$

where $\tau_{0,i}$, $T_{\mathrm{A},i}$, and $T_{\mathrm{V},i}$ are constants. The second term on the right-hand side of Eq. (12) is the contribution from the conductivity component, where $\gamma$ is an exponent, $\varepsilon_0$ is the dielectric permittivity in vacuo, and $\sigma$ is the conductivity. This conductivity component becomes more important as the thickness decreases. The conductivity $\sigma$ can be described using a VFT-like equation:

$$\sigma(T) = \frac{A}{T^{0.5}}\exp\left(\frac{T_{\mathrm{A,c}}}{T - T_{\mathrm{V,c}}}\right), \tag{14}$$

where $A$, $T_{\mathrm{A,c}}$, and $T_{\mathrm{V,c}}$ are constants [89]. The temperature dependence of $\varepsilon''$ can be fitted using Eq. (12) in addition to the constant background intensity. The solid curve in Fig. 19 is the curve calculated for $\varepsilon''$ using the best-fit parameters listed in

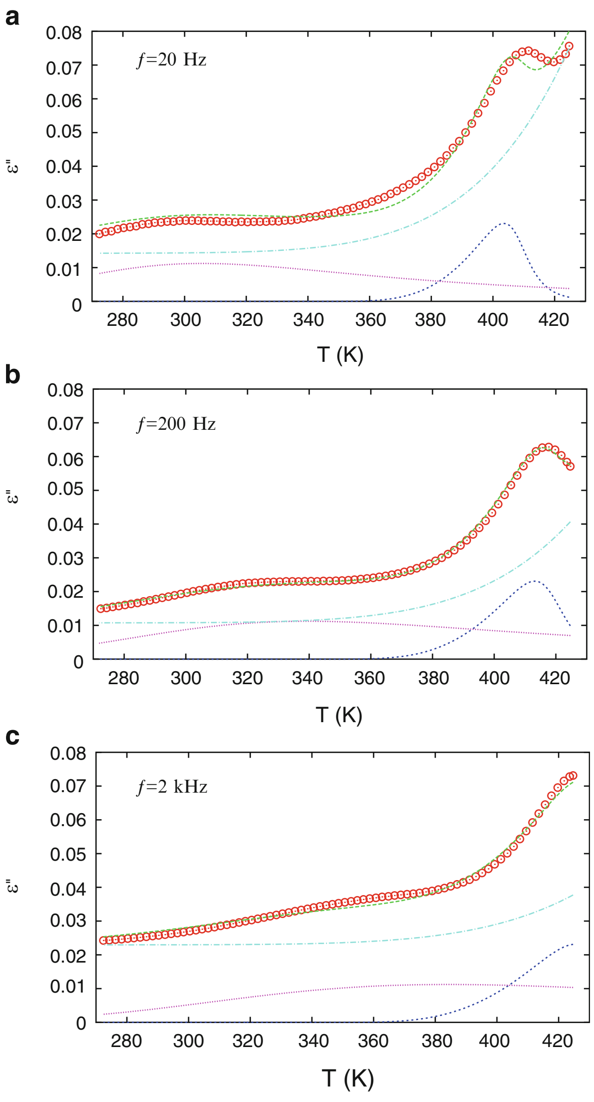

**Fig. 19** (**a**) Temperature dependence of the imaginary part of the complex dielectric constant $\varepsilon''$ for P2CS thin films with $d = 5.4$ nm obtained at $f =$ (**a**) 20 Hz, (**b**) 200 Hz, and (**c**) 2 kHz. The *dashed line through the symbols* is calculated using Eq. (12) with the best-fit parameters. The *dashed*, *dotted*, and *dash-dotted lines* correspond to the components of the α-process, the $\alpha_l$-process, and the conductivity, respectively

Table 5. Each component in Eq. (12) is also shown in Fig. 19. The fitting parameters listed in Table 5 are commonly obtained for the three different frequencies $f = 20$ Hz, 200 Hz, and 2 kHz. For the fitting procedures, the parameters of $T_{\mathrm{A},\alpha_l}$ $(T_{\mathrm{A,c}})$ and $T_{\mathrm{V},\alpha_l}(T_{\mathrm{V,c}})$ are assumed to be common for both the $\alpha_l$-process and the conductivity component.

**Table 5** Best-fit parameters for the frequency and temperature dependence of the dielectric loss $\varepsilon''$ observed for the P2CS ultrathin films of thickness $d$

| Process | $d$ (nm) | 1-$\alpha_i$ | $\beta_i$ | $\tau_{0,i}$ (s) | $T_{A,i}$ (K) | $T_{V,\ i}$ (K) | $\Delta\varepsilon_i$ |
|---|---|---|---|---|---|---|---|
| $\alpha$ | 9.5 | 0.68 ± 0.04 | 0.38 ± 0.03 | $(1.8 \pm 0.2) \times 10^{-12}$ | 1892 ± 1 | 324.6 ± 0.1 | 0.65 ± 0.03 |
| | 5.4 | 0.95 ± 0.11 | 0.22 ± 0.04 | $(5.4 \pm 1.0) \times 10^{-12}$ | 1884.4 ± 0.9 | 319.6 ± 0.1 | 0.12 ± 0.02 |
| | 3.7 | 0.65 ± 0.20 | 0.21 ± 0.11 | $(1.3 \pm 1.0) \times 10^{-11}$ | 1750.5 ± 0.8 | 317.2 ± 0.1 | 0.075 ± 0.030 |
| $\alpha_1$ | 9.5 | 0.26 | 1 | $3.5 \times 10^{-8}$ | $4.3 \times 10^{3}$ | 61 | 0.26 ± 0.13 |
| | 5.4 | 0.36 ± 0.12 | 1 | $(1.1 \pm 4.8) \times 10^{-10}$ | $(4.2 \pm 2.6) \times 10^{3}$ | 75 ± 92 | 0.078 ± 0.014 |
| | 3.7 | 0.42 ± 0.09 | 1 | $(0.87 \pm 2.6) \times 10^{-10}$ | $(4.2 \pm 1.5) \times 10^{3}$ | 72 ± 45 | 0.107 ± 0.010 |

| Process | $d$ (nm) | $A$ | $\gamma$ | $T_{A,c}$ | $T_{V,c}$ |
|---|---|---|---|---|---|
| Conductivity component | 9.5 | $2.0 \times 10^{-5}$ | 0.58 ± 0.24 | $4.3 \times 10^{3}$ | 61 |
| | 5.4 | $7.4 \times 10^{-6}$ | 0.31 ± 0.04 | $(4.2 \pm 2.6) \times 10^{3}$ | 75 ± 92 |
| | 3.7 | $(1.1 \pm 3.2) \times 10^{-5}$ | 0.34 ± 0.04 | $(4.2 \pm 1.5) \times 10^{3}$ | 72 ± 45 |

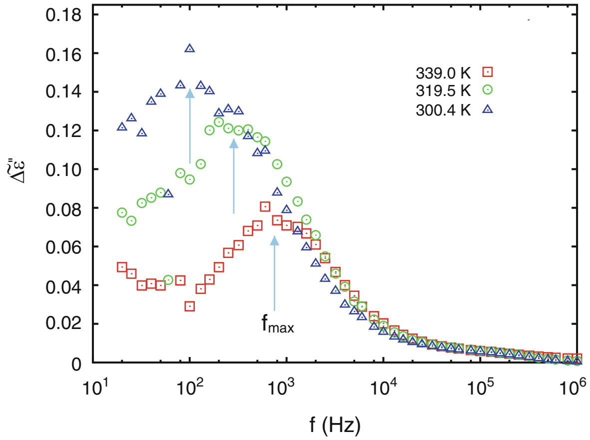

**Fig. 20** Frequency dependence of $\Delta\tilde{\varepsilon}''$ after isothermal aging at three different aging temperatures $T_a = 339.0$ (*squares*), 319.5 (*circles*), and 300.4 K (*triangles*) for 30 h with $d = 3.7$ nm

## 5.2 *Microscopic Origin of the Anomaly*

Here, we return to the aging dynamics observed for isothermal aging at $T_a$. For a given frequency $f$, we could observe the change in $\varepsilon''(t_w; f, T_a)$ from $\varepsilon''_{ref}(\equiv \varepsilon''(t_w = 0; f, T_a))$ (before isothermal aging at temperature $T_a$) to $\varepsilon''$ ($t_w$ = 30 h; $f$, $T_a$) after isothermal aging for 30 h. Here, we define the relative relaxation strength due to the isothermal aging as:

$$\Delta\tilde{\varepsilon}''(f, T_a) \equiv \frac{\varepsilon''(t_w = 30\,h; f, T_a) - \varepsilon''(t_w = 0; f, T_a)}{\varepsilon''(t_w = 0; f, T_a)}. \tag{15}$$

Figure 20 shows that the relative relaxation strength $\Delta\tilde{\varepsilon}''$ has a peak against frequency, and the peak frequency $f_{max}$ is strongly dependent on the aging temperature $T_a$. The frequency dependence of $\Delta\tilde{\varepsilon}''$ suggests that there may be a relation between the aging dynamics and a dynamical mode with a characteristic time (~$1/f_{max}$). It has been previously reported that for PMMA thin films, the relaxation strength for structural change during isothermal aging becomes larger with decreasing frequency at a given aging temperature and does not show a peak at any frequency [45, 47]. The frequency dependence of the relaxation strength due to isothermal aging for ultrathin P2CS films is completely different from that for PMMA.

A distinct peak of $\Delta\tilde{\varepsilon}''$ in the frequency domain at a given aging temperature can be seen in Fig. 20. A similar behavior related to the $\alpha_l$-process could also be observed in the temperature domain at a given frequency. As already shown in Fig. 16, there are two competing processes that have different aging time and temperature dependencies for isothermal aging at $T_a$. Here, we consider the time evolution of the dielectric loss $\varepsilon''$ for isothermal aging at $T_a$. For this process, it is assumed that there are two components; $\Delta\varepsilon''_{\mathrm{in}}$ is the component that increases with aging time and $\Delta\varepsilon''_{\mathrm{dec}}$ is the component that decreases with aging time, such that:

$$\varepsilon''(t_{\mathrm{w}};f,T_{\mathrm{a}}) - \varepsilon''_{\mathrm{ref}} = \Delta\varepsilon''_{\mathrm{in}}(t_{\mathrm{w}};f,T_{\mathrm{a}}) + \Delta\varepsilon''_{\mathrm{dec}}(t_{\mathrm{w}};f,T_{\mathrm{a}}), \tag{16}$$

where:

$$\varepsilon''_{\mathrm{ref}} \equiv \varepsilon''(t_{\mathrm{w}} = 0;f,T_{\mathrm{a}}), \tag{17}$$

$$\Delta\varepsilon''_{\mathrm{in}}(t_{\mathrm{w}};f,T_{\mathrm{a}}) \equiv \Delta\varepsilon_{\mathrm{l}}\left[1 - \left(1 + \frac{t_{\mathrm{w}}}{t_{\mathrm{l}}}\right)^{-n_{\mathrm{l}}}\right], \tag{18}$$

$$\Delta\varepsilon''_{\mathrm{dec}}(t_{\mathrm{w}};f,T_{\mathrm{a}}) \equiv \Delta\varepsilon_{\mathrm{b}}\left[\left(1 + \frac{t_{\mathrm{w}}}{t_{\mathrm{b}}}\right)^{-n_{\mathrm{b}}} - 1\right]. \tag{19}$$

The values $t_{\mathrm{l}}$ and $t_{\mathrm{b}}$ are the characteristic times, $n_{\mathrm{l}}$ and $n_{\mathrm{b}}$ are the exponents, and $\Delta\varepsilon_{\mathrm{l}}$ and $\Delta\varepsilon_{\mathrm{b}}$ are the relaxation strengths for the increasing and decreasing components, respectively. Here, we have decomposed the time evolution of $\varepsilon'' - \varepsilon''_{\mathrm{ref}}$ into two competing components, $\Delta\varepsilon''_{\mathrm{in}}$ and $\Delta\varepsilon''_{\mathrm{dec}}$, using Eqs. (18) and (19) for isothermal aging at $T_{\mathrm{a}}$ and three different frequencies for ultrathin P2CS films with $d = 3.7$ nm. The best-fit parameters for the time evolution of $\varepsilon'' - \varepsilon''_{\mathrm{ref}}$ for isothermal aging at $T_{\mathrm{a}}$ are listed in Table 6. For the fitting procedures, the parameter $n_{\mathrm{l}}$ is fixed to 1 and the parameters $t_{\mathrm{b}}$ and $n_{\mathrm{b}}$ for fitting the data for $d = 3.7$ nm are fixed to those obtained by fitting the observed data to Eq. (19) with 2 and 4 kHz for $d = 22$ nm. For the decreasing component $\Delta\varepsilon''_{\mathrm{dec}}$, only the value of $\Delta\varepsilon_{\mathrm{b}}$ is adjusted in order to reproduce the observed results for $d = 3.7$ nm at the three different frequencies. An example of the decomposition of $\varepsilon''$ into $\Delta\varepsilon''_{\mathrm{in}}$ and $\Delta\varepsilon''_{\mathrm{dec}}$ is shown in Fig. 16c.

From the decomposition procedures, we have obtained the relaxation strength $\Delta\varepsilon_{\mathrm{l}}$ of the increasing components as a function of the aging temperature $T_{\mathrm{a}}$ for given frequencies of $f = 20$ Hz, 200 Hz, and 2 kHz. (see filled symbols in Fig. 21.) In order to compare the aging dynamics with the dynamical mode of the $\alpha_{\mathrm{l}}$-process, we also plotted in Fig. 21 the component of $\varepsilon''$ only for the $\alpha_{\mathrm{l}}$-process, $\varepsilon''_{\alpha_{\mathrm{l}}}$, that has been reproduced using the HN equation with the best-fit parameters for the $\alpha_{\mathrm{l}}$-process listed in Table 5 (see the open symbols in Fig. 21). Figure 21 shows that the temperature dependence of the aging strength due to the increasing component is strongly associated with that of the dielectric loss due only to the $\alpha_{\mathrm{l}}$-process.

Figure 22 shows Arrhenius plots of the relaxation times for the $\alpha$- and $\alpha_{\mathrm{l}}$-processes obtained by the peak frequency of the dielectric loss $\varepsilon''$ for P2CS thin films with $d = 3.7$ nm. The peak frequencies $f_{\alpha}$ and $f_{\alpha_{\mathrm{l}}}$ are evaluated from the frequency dependence of the dielectric loss due only to the $\alpha$- and $\alpha_{\mathrm{l}}$-processes that are reproduced from Eq. (12) with best-fit parameters. The peak frequency of $\Delta\tilde{\varepsilon}''(f,T_{\mathrm{a}})$ after isothermal aging at a given aging temperature $T_{\mathrm{a}}$ for 30 h and with

**Table 6** Best-fit parameters for the aging time dependence of $\varepsilon'' - \varepsilon''_{\text{ref}}$ for isothermal aging at $T_{\text{a}} = 300$–$358$ K and for $f = 2$ kHz, 200 Hz, and 20 Hz

| $T_{\text{a}}$ | $f = 2$ kHz | | | $f = 200$ Hz | | | $f = 20$ Hz | | | $t_{\text{b}}$ | $n_{\text{b}}$ |
|---|---|---|---|---|---|---|---|---|---|---|---|
| (K) | $\Delta\varepsilon_{\text{l}}$ | $t_{\text{l}}$ (min) | $\Delta\varepsilon_{\text{b}}$ | $\Delta\varepsilon_{\text{l}}$ | $t_{\text{l}}$ (min) | $\Delta\varepsilon_{\text{b}}$ | $\Delta\varepsilon_{\text{l}}$ | $t_{\text{l}}$ (min) | $\Delta\varepsilon_{\text{b}}$ | (min) | |
| 358.2 | 0.00183 | 102 ± 1 | 0.00558 | 0.00085 | 61 ± 3 | 0.00349 | 0.00153 | 68 ± 2 | 0.00741 | 45 ± 1 | 0.036 ± 0.003 |
| 348.6 | 0.00247 | 165 ± 2 | 0.00603 | 0.00137 | 97 ± 3 | 0.00636 | 0.00198 | 122 ± 3 | 0.01046 | 157 ± 3 | 0.043 ± 0.005 |
| 339.2 | 0.00300 | 233 ± 2 | 0.00839 | 0.00275 | 178 ± 4 | 0.01969 | 0.00275 | 153 ± 2 | 0.02216 | 120 ± 6 | 0.026 ± 0.009 |
| 329.4 | 0.00278 | 324 ± 2 | 0.00483 | 0.00396 | 250 ± 3 | 0.03159 | 0.00402 | 199 ± 2 | 0.04524 | 76 ± 4 | 0.017 ± 0.011 |
| 319.5 | 0.00232 | 402 ± 2 | 0 | 0.00387 | 413 ± 9 | 0.02705 | 0.00491 | 391 ± 5 | 0.07393 | 317 ± 12 | 0.018 ± 0.009 |
| 310.1 | 0.00202 | 450 ± 2 | 0 | 0.00329 | 471 ± 5 | 0.01145 | 0.00533 | 418 ± 3 | 0.06581 | 113 ± 12 | 0.010 ± 0.020 |
| 300.4 | 0.00189 | 634 ± 5 | 0 | 0.00272 | 632 ± 6 | 0 | 0.00472 | 614 ± 5 | 0.05685 | 220 ± 30 | 0.010 ± 0.040 |

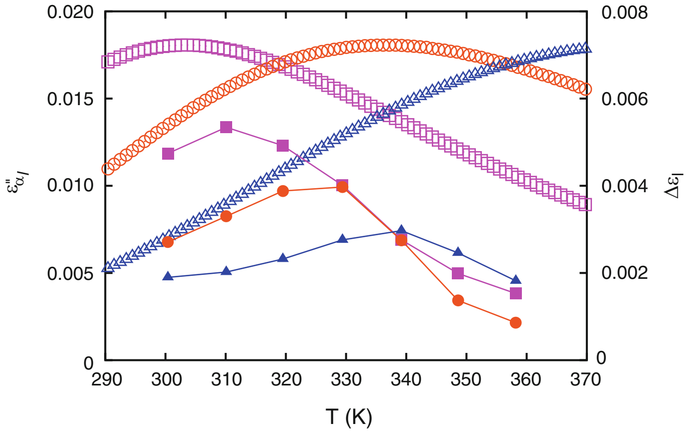

**Fig. 21** Temperature dependence of the $\alpha_l$-process component of dielectric loss, $\varepsilon''_{\alpha,l}$, at $f = 20$ Hz (*open squares*), 200 Hz (*open circles*) and 2 kHz (*open triangles*) and aging temperature dependence of the increasing $\varepsilon''$ component during isothermal aging, $\Delta\varepsilon_l$ at $f = 20$ Hz (*filled squares*), 200 Hz (*filled circles*) and 2 kHz (*filled triangles*)

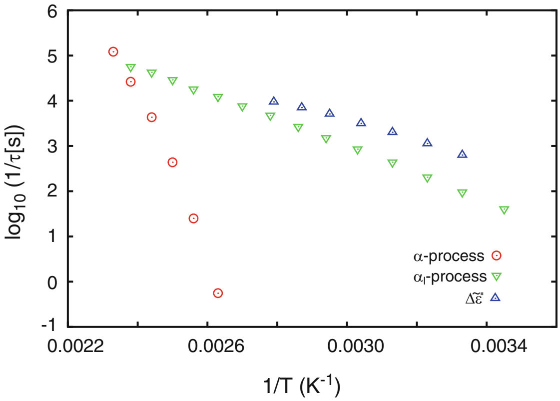

**Fig. 22** Arrhenius plots for the $\alpha$- and $\alpha_l$-processes of ultrathin P2CS films with $d = 3.7$ nm. The value of $\tau$ is evaluated from the relationship $1/2\pi\tau = f_{\max}, f_\alpha$, or $f_{\alpha_l}$. The *circles* correspond to the data obtained from the peak frequency $f_\alpha$ of the dielectric loss $\varepsilon''$ due only to the $\alpha$-process, which is evaluated by fitting the observed values of $\varepsilon''$ to Eq. (12). The *inverted triangles* correspond to the data obtained from $f_{\alpha_l}$ due only to the $\alpha_l$-process. The *triangles* correspond to the peak frequency of $\Delta\tilde{\varepsilon}''$, $f_{\max}$, in Fig. 20 at a given aging temperature $T_a$

$d = 3.7$ nm is also plotted in Fig. 22. The peak frequency is evaluated from the observed frequency dependence of $\Delta\tilde{\varepsilon}''$ in Fig. 20.

From Fig. 22, the temperature dependence of the characteristic time $\tau$ evaluated from the aging dynamics is quite similar to that evaluated from the dynamics of the $\alpha_l$-process , but is completely different from that evaluated from the dynamics of the

$\alpha$-process. Therefore, it can be concluded that the anomalous increase in dielectric susceptibility observed for isothermal aging of ultrathin P2CS films is strongly associated with the $\alpha_l$-process.

### 5.3 Remarks on Anomaly Observed in Aging Dynamics in Ultrathin P2CS Films

Occurrence of the $\alpha_l$-process may lead to the increase in the dielectric susceptibility with isothermal aging of P2CS ultrathin films. The most probable candidate for the microscopic origin of the $\alpha_l$-process is the presence of a mobile interfacial region where the polymer chains can maintain their mobility, even below the bulk $T_g$. Such mobility can destroy the "ordering" that is developed during the aging process. In other words, the mobility can rejuvenate the glassy state for ultrathin films of P2CS.

The presented measurements showed that the dielectric susceptibility increases with increasing aging time for the isothermal aging of ultrathin P2CS films. Here, we question how the mobile layer can increase the dielectric susceptibility with increasing aging time. For thin polymer films, de Gennes proposed that there is a sliding motion for the thin film geometry of polymers [90, 91]. Even in the glassy state, a polymer chain can move along its own contour if there is a interfacial mobile layer.

The occurrence of a sliding motion can cause polymer chains in the bulk region to move to the mobile region near the interface during isothermal aging. The number of polymer chains that belong to the mobile region increases, and the fraction of polymer chains that contribute to the $\alpha_l$-process increases. This phenomenon manifests as an increase in $\varepsilon''$ for isothermal aging at a given temperature and frequency. We propose this as a possible scenario for the present anomalous increase in $\varepsilon''$ for isothermal aging.

Our previous measurements of P2CS thin films with thicknesses greater than 10 nm showed that the dielectric susceptibility and volume both decrease with increase in the aging time for isothermal aging [60]. The decrease in volume causes an increase in the electric capacitance. In this case, the decrease in dielectric susceptibility competes with the decrease in volume for determination of the aging time dependence of the electric capacitance. Therefore, we consider the possibility that the volume change during isothermal aging could cause an artificial increase in the dielectric susceptibility. Table 7 shows the decrease in volume and the increase in the imaginary part of the electric capacitance $C''$ for isothermal aging at $T_a = 300$–$358$ K. The increment in $C''$ is far greater than the decrease in volume; therefore, the possibility of an artificial increase is denied.

To summarize Sect. 5, we have observed an anomalous increase in the dielectric susceptibility for the isothermal aging of ultrathin P2CS films below $T_g$, and the fraction of the interfacial mobile region where the polymer chains are mobile as observed in a liquid state can increase in accordance with the increase in dielectric susceptibility.

**Table 7** The decrease in volume and the increase in the imaginary part of the electric capacitance $C''$ for isothermal aging at $T_a = 300 - 358$ K

| $T_\mathrm{a}$ (K) | $\Delta\tilde{v}^\mathrm{a}$ | $\Delta\tilde{C}''^\mathrm{b}$ | $\Delta\tilde{C}''/\Delta\tilde{v}$ |
|---|---|---|---|
| 300 | $1.14 \times 10^{-3}$ | $8.44 \times 10^{-2}$ | 74.1 |
| 319 | $1.36 \times 10^{-3}$ | $9.93 \times 10^{-2}$ | 73.0 |
| 339 | $1.59 \times 10^{-3}$ | $7.44 \times 10^{-2}$ | 46.7 |
| 358 | $2.30 \times 10^{-3}$ | $2.90 \times 10^{-2}$ | 12.6 |

[a] $\Delta\tilde{v}$ is the relative decrease in volume for isothermal aging at $T_a$ for 30 h such that $\Delta\tilde{v} \equiv -(v(t_\mathrm{w} = 30h) - v(t_\mathrm{w} = 0))/v(t_\mathrm{w} = 0)$ where $v(t_\mathrm{w})$ is the volume at time $t_\mathrm{w}$

[b] $\Delta\tilde{C}''$ is the maximum relative deviation of $C''$ from the initial value at $t_\mathrm{w} = 0$ during isothermal aging such that $\Delta\tilde{C}'' \equiv (C''(t_\mathrm{w} = t_\mathrm{max}) - C''(t_\mathrm{w} = 0))/C''(t_\mathrm{w} = 0)$, where $C''(t_\mathrm{w})$ is the imaginary part of the complex electric capacitance at $t_\mathrm{w}$ for an applied electric field frequency of $f = 1$ kHz and $t_\mathrm{max}$ is the time at which $C''$ has a maximum during isothermal aging

# 6 Summary

In this article, we have discussed two different topics related to the glass transition of thin polymer films. As the first topic, we have shown the experimental results of the glass transition and $\alpha$-dynamics of stacked thin polymer films measured by DSC and DRS. It has been revealed that interfacial interaction can play a crucial role in determining how $T_\mathrm{g}$ deviates from the value of the bulk system if the thickness decreases from that of the bulk. Furthermore, annealing above $T_\mathrm{g}$ can induce a change in the interfacial interaction between thin layers, and this can control the fragility and the non-Arrhenius behavior.

As the second topic, we have discussed an anomalous phenomenon observed for the aging dynamics in single ultrathin polymer films. From this study, it has been elucidated that the anomalous increase in dielectric susceptibility observed for isothermal aging processes is strongly associated with the mobile region that exists at the surface and interfacial region of thin polymer films.

Research on the glass transition of thin polymer films started in 1990s for the purpose of determining the existence and the nature of the characteristic length scale of dynamics such as dynamical heterogeneity. However, as a by-product, researchers clarified that heterogeneous dynamics strongly influence the $\alpha$-process and the aging phenomena observed above and below $T_\mathrm{g}$ and, as a result, produce many fascinating phenomena. Here, the heterogeneous dynamics include the mobile regions near the surface and/or interface and heterogeneity induced by the geometrical constraint in thin films. These phenomena seem very complex, but it can be expected that they are strongly associated with each other. From the various experimental results related to the phenomena, we will be able to extract the essence of the glass transition and reach the final goal of the understanding of the mechanism of glass transition.

**Acknowledgements** This work was supported by a Grant-in-Aid for Scientific Research (B) (No. 21340121) and Exploratory Research (No. 23654154) from the Japan Society for the Promotion of Science, Scientific Research in the Priority Area "Soft Matter Physics" and "High-Tech Research Center" Project for Private Universities: matching fund subsidy from the Ministry of Education, Culture, Sports, Science and Technology of Japan.

## References

1. Ngai KL (2003) The glass transition and the glassy state. In: Mark J (ed) Physical properties of polymers, 3rd edn. Cambridge University Press, Cambridge
2. Anderson PW (1995) Through the glassy lightly. Science 267:1609–1618
3. Ngai KL, Wright GB (eds) (1991) Proceedings of the 1st international discussion meetings on relaxations in complex systems. J Non-Cryst Solids 131–133:1–1285
4. Ngai KL, Riande E, Wright GB (eds) (1994) Proceedings of the 2nd international discussion meetings on relaxations in complex systems. J Non-Cryst Solids 172–174:1–1457
5. Ngai KL (ed) (1998) Proceedings of the 3rd international discussion meetings on relaxations in complex systems. J Non-Cryst Solids 235–237:1–814
6. Ngai KL (ed) (2002) Proceedings of the 4th international discussion meetings on relaxations in complex systems. J Non-Cryst Solids 307–310:1–1080
7. Affouard F, Descamps M, Ngai KL (eds) (2006) Proceedings of the 5th international discussion meetings on relaxations in complex systems. J Non-Cryst Solids 352:4731–5250
8. Ngai KL, Ruocco G (eds) (2011) Proceedings of the 6th international discussion meetings on relaxation in complex systems. J Non-Cryst Solids 357:241–782
9. Vogel H (1921) Das Temperatur-Abhängigkeitsgesetz der Viskosität von Flüssigkeiten. Phys Z 22:645–646
10. Fulcher GS (1925) Analysis of recent measurements of the viscosity of glasses. J Am Ceram Soc 8:339–355
11. Tammann G, Hesse W (1926) Die Abhängigkeit der Viscosität von der Temperatur bei unterkühlten Flüssigkeiten. Z Anorg Allg Chem 156:245–256
12. Williams G, Watts DC (1970) Non-symmetrical dielectric relaxation behaviour arising from a simple empirical decay function. Trans Faraday Soc 66:80–85
13. Sillescu H (1999) Heterogeneity at the glass transition: a review. J Non-Cryst Solids 243:81–108
14. Berthier L, Biroli G, Bouchaud J-P, Cipelletti L, van Saarloos W (eds) (2010) Dynamical heterogeneities in glasses, colloids and granular media. Oxford University Press, New York
15. Adam G, Gibbs JH (1965) On the temperature dependence of cooperative relaxation properties in glass-forming liquids. J Chem Phys 43:139–146
16. Alcoutlabi M, McKenna GB (2005) Effects of confinement on material behavior at the nanometer size scale. J Phys Condens Matter 17:R461–R524
17. Keddie J, Jones RAL, Cory RA (1994) Size-dependent depression of the glass transition temperature in polymer films. Europhys Lett 27:59–64
18. Keddie JL, Jones RAL (1994) Interface and surface effects on the glass-transition temperature in thin polymer films. Faraday Discuss 98:219–230
19. Schüller J, Mel'nichenko YuB, Richert R, Fischer EW (1994) Dielectric studies of the glass transition in porous media. Phys Rev Lett 73:2224–2227
20. DeMaggio GB, Frieze WE, Gidley DW, Zhu M, Hristov HA, Yee AF (1997) Interface and surface effects on the glass transition in thin polystyrene Films. Phys Rev Lett 78:1524–1527
21. Wallace WE, van Zanten JH, Wu WL (1995) Influence of an impenetrable interface on a polymer glass-transition temperature. Phys Rev E 52:R3329–R3332
22. Jerome B, Commandeur J (1997) Dynamics of glasses below the glass transition. Nature 386:589–592
23. Efremov MYu, Olson EA, Zhang M, Zhang Z, Allen LH (2003) Glass transition in ultrathin polymer films: calorimetric study. Phys Rev Lett 91:085703
24. Lupascu V, Huth H, Schick C, Wübbenhorst M (2005) Specific heat and dielectric relaxations in ultra-thin polystyrene layers. Thermochim Acta 432:222–228
25. Hall DB, Hooker JC, Torkelson JM (1997) Ultrathin polymer films near the glass transition: effect on the distribution of alpha-relaxation times as measured by second harmonic generation. Macromolecules 30:667–669

26. Fukao K, Miyamoto Y (1999) Glass transition temperature and dynamics of α-process in thin polymer films. Europhys Lett 46:649–654
27. Fukao K, Miyamoto Y (2000) Glass transitions and dynamics in thin polymer films: dielectric relaxation of thin films of polystyrene. Phys Rev E 61:1743–1754
28. Grohens Y, Hamon L, Reiter G, Soldera A, Holl Y (2002) Some relevant parameters affecting the glass transition of supported ultra-thin polymer films. Eur Phys J E 8:217–224
29. Sharp JS, Forrest JA (2003) Dielectric and ellipsometric studies of the dynamics in thin films of isotactic poly(methylmethacrylate) with one free surface. Phys Rev E 67:031805
30. Ellison CJ, Torkelson JM (2003) The distribution of glass-transition temperatures in nanoscopically confined glass formers. Nat Mater 2:695–700
31. Roth CB, Dutcher JR (2003) Glass transition temperature of freely-standing films of atactic poly(methyl methacrylate). Eur Phys J E 12:S103–S107
32. Ellison CJ, Mundra MK, Torkelson JM (2005) Impacts of polystyrene molecular weight and modification to the repeat unit structure on the glass transition-nanoconfinement effect and the cooperativity length scale. Macromolecules 38:1767–1778
33. Arndt M, Stannarius R, Groothues H, Hempel E, Kremer F (1997) Length scale of cooperativity in the dynamic glass transition. Phys Rev Lett 79:2077–2080
34. Hartmann L, Gorbatschow W, Hauwende J, Kremer F (2002) Molecular dynamics in thin films of isotactic poly(methyl methacrylate). Eur Phys J E 8:145–154
35. Huth H, Minakov AA, Serghei A, Kremer F, Schick C (2007) Differential ac-chip calorimeter for glass transition measurements in ultra thin polymeric films. Euro Phys J Special Topics 141:153–160
36. Tress M, Erber M, Mapesa EU, Huth H, Mller J, Serghei A, Schick C, Eichhorn K-J, Voit B, Kremer F (2010) Glassy dynamics and glass transition in nanometric thin layers of polystyrene. Macromolecules 43:9937–9944
37. Forrest JA, Dalnoki-Veress K, Dutcher JR (1997) Interface and chain confinement effects on the glass transition temperature of thin polymer films. Phys Rev E 56:5705–5716
38. Kajiyama T, Tanaka K, Ohki I, Ge S-R, Yoon SJ, Takahara A (1994) Imaging of dynamic viscoelastic properties of a phase-separated polymer surface by forced oscillation atomic force microscopy. Macromolecules 27:7932–7934
39. Koh YP, McKenna GB, Simon SL (2006) Calorimetric glass transition temperature and absolute heat capacity of polystyrene ultrathin films. J Polym Sci, Part B: Polym Phys 44:3518–3527
40. Koh YP, Simon SL (2008) Structural relaxation of stacked ultrathin polystyrene films. J Polym Sci, Part B: Polym Phys 46:2741–2753
41. Strobl G (1996) The physics of polymers: concepts for understanding their structures and behavior. Springer, Berlin
42. Struick LC (1978) Physical aging in amorphous polymers and other materials. Elsevier, Amsterdam
43. Kovacs AJ, Aklonis JJ, Hutchinson JM, Ramos AA (1979) Isobaric volume and enthalpy recovery of glasses II. A transparent multiparameter theory. J Polym Sci: Polym Phys Ed 17:1097–1162
44. Bouchaud J-P (2000) Aging in glassy systems: experiments, models, and open questions. In: Cates ME, Evans MR (eds) Soft and fragile matter. IOP publishing, London, pp 285–304
45. Bellon L, Ciliberto S, Laroche C (2002) Advanced memory effects in the aging of a polymer glass. Eur Phys J B 25:223–231
46. Bellon L, Ciliberto S, Laroche C (1999) Temperature cycling during the aging of a polymer glass. Available at http://arxiv.org/abs/cond-mat/9905160
47. Fukao K, Sakamoto A (2005) Aging phenomena in poly(methyl methacrylate) thin films: memory and rejuvenation effects. Phys Rev E 71:041803
48. Fukao K, Sakamoto A, Kubota Y, Saruyama Y (2005) Aging phenomena in poly(methyl methacrylate) by dielectric spectroscopy and temperature modulated DSC. J Non Cryst Solids 351:2678–2684

49. Fukao K, Yamawaki S (2007) Crossover of aging dynamics in polymer glass: from cumulative aging to noncumulative aging. Phys Rev E 76:021507
50. Bodiguel H, Lequeux F, Montes H (2008) Revealing the respective effect of aging and cyclic deformation through the memory effect in glassy polymers. J Stat Mech 2008:P01020. doi:10.1088/1742-5468/2008/01/P01020
51. Lefloch F, Hammann J, Ocio M, Vincent E (1992) Can aging phenomena discriminate between the droplet model and a hierarchical description in spin glasses? Europhys Lett 18:647–652
52. Vincent E, Bouchaud J-P, Hamman J, Lefloch F (1995) Contrasting effects of field and temperature variations on ageing in spin glasses. Philos Mag B 71:489–500
53. Jonason K, Vincent E, Hammann J, Bouchaud J-P, Nordblad P (1998) Memory and chaos effects in spin glasses. Phys Rev Lett 81:3243–3246
54. Jonason K, Nordblad P, Vincent E, Hammann J, Bouchaud J-P (2000) Memory interference effects in spin glasses. Eur Phys J B 13:99–105
55. Doussineau P, de Lacerda-Aroso T, Levelut A (1999) Aging and memory effects in a disordered crystal. Europhys Lett 46:401–406
56. Leheny RL, Nagel SR (1998) Frequency-domain study of physical aging in a simple liquid. Phys Rev B 57:5154–5162
57. Kircher O, Böhmer R (2002) Probing electron–phonon coupling in high-$T_c$ superconductors by site-selective isotope substitution. Eur Phys J B 26:329–338
58. Fukao K, Koizumi H (2007) Aging phenomena in polystyrene thin films. Eur Phys J Special Topics 141:199–202
59. Fukao K, Koizumi H (2008) Glassy dynamics in thin films of polystyrene. Phys Rev E 77:021503
60. Fukao K, Tahara D (2009) Aging dynamics in the polymer glass of poly(2-chlorostyrene): dielectric susceptibility and volume. Phys Rev E 80:051802
61. Fukao K, Miyamoto Y (2001) Slow dynamics near glass transitions in thin polymer films. Phys Rev E 64:011803
62. Fukao K (2008) Dielectric behavior of glass transition and dynamics in thin polymer films. Nihon Reoroji Gakkaishi (J Soc Rheol Jpn) 36:73–80
63. Kawana S, Jones RAL (2003) Effect of physical ageing in thin glassy polymer films. Eur Phys J E 10:223–230
64. Ellison CJ, Kim SD, Hall DB, Torkelson JM (2002) Confinement and processing effects on glass transition temperature and physical aging in ultrathin polymer films: novel fluorescence measurements. Eur Phys J E 8:155–166
65. Priestley RD, Ellison CJ, Broadbelt LJ, Torkelson JM (2005) Structural relaxation of polymer glasses at surfaces, interfaces, and in between. Science 309:456–459
66. Priestley RD, Broadbelt LJ, Torkelson JM (2005) Physical aging of ultrathin polymer films above and below the bulk glass transition temperature: effects of attractive vs neutral polymersubstrate interactions measured by fluorescence. Macromolecules 38:654–657
67. Fukao K, Oda Y, Nakamura K, Tahara D (2010) Glass transition and dynamics of single and stacked thin films of poly(2-chlorostyrene). Euro Phys J Special Topics 189:165–171
68. Fukao K, Terasawa T, Oda Y, Nakamura K, Tahara D (2011) Glass transition dynamics of stacked thin polymer films. Phys Rev E 84:041808
69. Tahara D, Fukao K (2010) Anomalous increase in dielectric susceptibility during isothermal aging of ultrathin polymer films. Phys Rev E 82:051801
70. Forrest JA, Dalnoki-Veress K, Stevens JR, Dutcher JR (1996) Effect of free surfaces on the glass transition temperature of thin polymer films. Phys Rev Lett 77:2002–2005
71. McCrum NG, Read BE, Williams G (1967) Anelastic and dielectric effects in polymer solids. Wiley, London, p 414, Figure 10.35
72. Whitlow SJ, Wool RP (1991) Diffusion of polymers at interfaces: a secondary ion mass spectroscopy study. Macromolecules 24:5926–5938
73. Napolitano S, Wübbenhorst M (2011) The lifetime of the deviations from bulk behaviour in polymers confined at the nanoscale. Nat Commun 2:260

74. Napolitano S, Rotella C, Wübbenhorst M (2011) Is the reduction in tracer diffusivity under nanoscopic confinement related to a frustrated segmental mobility? Macromol Rapid Commun 32:844–848
75. Inoue R, Kawashima K, Matsui K, Kanaya T, Nishida K, Matsuba G, Hino M (2011) Distributions of glass-transition temperature and thermal expansivity in multilayered polystyrene thin films studied by neutron reflectivity. Phys Rev E 83:021801
76. Bowden FB, Tabor D (1954) The friction and lubrication of solids. Clarendon, Oxford
77. Dieterich JH, Conrad G (1984) Effect of humidity on time- and velocity-dependent friction in rocks. J Geophys Res 89:4196–4202
78. Priestley RD, Broadbelt LJ, Torkelson JM, Fukao K (2007) Glass transition and $\alpha$-relaxation dynamics of thin films of labeled polystyrene. Phys Rev E 75:061806
79. Havriliak S, Negami S (1967) A complex plane representation of dielectric and mechanical relaxation processes in some polymers. Polymer 8:161–210
80. Alvarez F, Alegria A, Colmenero J (1991) Relationship between the time-domain Kohlrausch-Williams-Watts and frequency-domain Havriliak-Negami relaxation functions. Phys Rev B Condens Matter 44:7306–7312
81. Böhmer R, Angell CA (1992) Correlations of the nonexponentiality and state dependence of mechanical relaxations with bond connectivity in Ge-As-Se supercooled liquids. Phys Rev B Condens Matter 45:10091–10094
82. Böhmer R, Ngai KL, Angell CA, Plazek DJ (1993) Nonexponential relaxations in strong and fragile glass formers. J Chem Phys 99:4201–4209
83. Debenedetti PG, Stillinger FH (2001) Supercooled liquids and the glass transition. Nature (London) 410:259–267
84. Napolitano S, Wübbenhorst M (2010) Structural relaxation and dynamic fragility of freely standing polymer films. Polymer 51:5309–5312
85. Fukao K, Uno S, Miyamoto Y, Hoshino A, Miyaji H (2001) Dynamics of $\alpha$ and $\beta$ processes in thin polymer films: poly(vinyl acetate) and poly(methyl methacrylate). Phys Rev E 64:051807
86. Akabori K, Tanaka K, Nagamura T, Takahara A, Kajiyama T (2005) Molecular motion in ultrathin polystyrene films: dynamic mechanical analysis of surface and interfacial effects. Macromolecules 38:9735–9741
87. Kanaya T, Inoue R, Kawashima K, Miyazaki T, Tsukushi I, Shibata T, Matsuba G, Nishida K, Hino M (2009) Glassy dynamics and heterogeneity of polymer thin films. J Phys Soc Jpn 78:041004
88. Kawashima K, Inoue R, Kanaya T, Matsuba G, Nishida K, Hino M (2009) Distribution of glass transition temperature $T_g$ in a polymer thin film by neutron reflectivity. J Phys Conf Ser 184:012004
89. Jeevanandam P, Vasudevan S (1998) Conductivity of a confined polymer electrolyte: lithium-polypropylene glycol intercalated in layered $CdPS_3$. J Phys Chem B 102:4753–4758
90. de Gennes PG (2000) Glass transitions in thin polymer films. Eur Phys J E 2:201–205
91. de Gennes PG (2000) Glass transitions of freely suspended polymer films. C R Acad Sci IV-Phys 1:1179–1186

Adv Polym Sci (2013) 252: 107–140
DOI: 10.1007/12_2012_173

# Heterogeneous Dynamics of Polymer Thin Films as Studied by Neutron Scattering

**Rintaro Inoue and Toshiji Kanaya**

**Abstract** This review covers recent progress in studies on the dynamics of polymer thin films in the glassy state and near the glass transition temperature, as revealed by neutron scattering. First, the glassy dynamics including low energy excitation (Boson peak) and the fast localized process of polymer thin films at the picosecond timescale was studied to reveal the effect of film thickness. The dynamic heterogeneity of polymer thin films in the glassy state was also evaluated in terms of non-Gaussian parameters. Second, the glass transition temperature of polymer thin films was investigated using inelastic neutron scattering with high-energy resolution to clarify the mechanism of its dependence on film thickness. Finally, neutron reflectivity was used to study the distribution of glass transition temperature in a multilayered thin film consisting of deuterated polymer and hydrogenated polymer.

**Keywords** Dynamic heterogeneity · Inelastic and quasielastic neutron scattering · Polymer thin film

## Contents

1 Introduction .......... 108
2 Physical Properties of Polymer Thin Films .......... 109
3 Basic Principles of Inelastic and Quasielastic Neutron Scattering .......... 110
4 Glassy Dynamics of Polymer Thin Films in the Picosecond Region .......... 113
5 Glass Transition of Polymer Thin Films in the Nanosecond Region .......... 128
6 Distribution of Glass Transition Temperature in Thin Films .......... 134
7 Concluding Remarks .......... 137
References .......... 138

---

R. Inoue and T. Kanaya (✉)
Institute for Chemical Research, Kyoto University, Uji, Kyoto-fu 611-0011, Japan
e-mail: kanaya@scl.kyoto-u.ac.jp

# 1 Introduction

Polymer thin films are utilized in the field of industrial applications such as lithography, coating, lubrication and so on and extensive studies have revealed that the thermal and mechanical properties of polymer thin films are quite different to those of bulk polymer [1, 2]. The thickness dependence of the glass transition temperature ($T_g$) [3–13], the thermal expansivity [7, 14], the ultra-slow expansion and contraction process [15], and the dewetting at temperatures lower than $T_g$ of the bulk polymer [16, 17] are some of the representative examples of the anomalous properties of polymer thin films. At present, it is believed that most of singular physical properties of polymer thin films are related to the anomalous physical properties of the surface or interfacial region, hence we have to take into consideration the heterogeneous structure of polymer thin films to understand the singularity of polymer thin films.

For evaluation of the dynamic heterogeneity, there exist some experimental methods like nuclear magnetic resonance (NMR) [18], photo probe [19], and inelastic neutron scattering (INS) [20]. The advantage of INS is the direct probe of time ($t$) and space ($Q$) simultaneously; hence, we can discuss the heterogeneity of polymer thin films from both the static and dynamic point of view. Another advantage of INS is the relatively broad experimentally accessible temperature range, covering from far below bulk $T_g$ to above bulk $T_g$. Hence, we can study the dynamics of polymer thin films in both glassy and molten state using INS. So far, few experimental approaches have been developed for studying the glassy state of polymer thin films even though some researchers have discussed the correlation between glassy dynamics and dynamics near $T_g$ for bulk systems [21, 22]. We believe that glassy dynamics cannot be overlooked in the investigation of glass transition or related properties of polymer thin films, therefore measurements covering a broad temperature range are necessary.

In this review, we investigate the dynamic heterogeneity or anomalous dynamics of polymer thin films at temperatures from far below bulk $T_g$ to above bulk $T_g$ by neutron scattering. We also discuss the effect of dynamic heterogeneity on the resulting glassy and molten dynamics of polymer thin films.

The arrangement of this article is as follows: In Sect. 2, we briefly survey previous works on glass transition and related works on polymer thin films. Section 3 briefly describes the basic principles of inelastic and quasielastic neutron scattering for the reader's convenience. Section 4 discusses the thickness dependence of mean squared displacement $\langle u^2 \rangle$, as evaluated from $Q^2$ dependence of the elastic scattering intensity at the picosecond time scale. The physical origin for the change in $\langle u^2 \rangle$ with thickness is discussed from the point of view of molecular weight, Boson peak, and local relaxation (the so-called fast process). Afterwards, we discuss the dynamic heterogeneity of polymer thin films in terms of non-Gaussian parameters evaluated from the $Q^2$ dependence of elastic scattering intensity, taking advantage of the high $Q$ accessible spectrometer. Section 5 is dedicated to the thickness dependence of $T_g$, as evaluated using ellipsometry and INS with different energy resolutions.

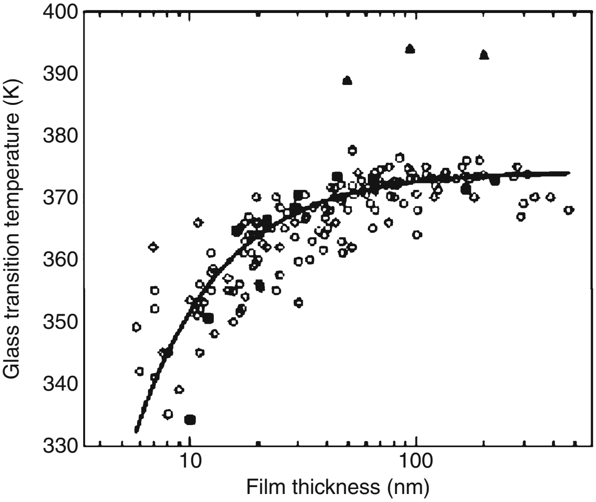

**Fig. 1** Dependence of glass transition temperature on thickness of PS thin film supported on Si substrate Symbols other than *solid squares* were cited from formerly reported results and *solid squares* were from [5]. Solid line is the empirical fitting function to the observed data. For further detail please refer to [5]

The results are discussed with relation to the relaxation time map. The distribution of $T_g$ in a thin film is discussed in Sect. 6 for multilayered thin films utilizing isotope labeling by neutron reflectivity. Concluding remarks are given in Sect. 7.

## 2 Physical Properties of Polymer Thin Films

In this section, we review recent investigations into the physical properties of polymer thin films. After the pioneering works by Keddie et al. [3], the thickness dependence of $T_g$ was systematically studied by various methods including ellipsometry [3–5], X-ray/neutron reflectivity [6–8], dielectric relaxation [9, 10], local thermal analysis [11], and differential scanning calorimetry (DSC) [12, 13]. For example, the reduction in $T_g$ with thickness was observed for polystyrene (PS) thin films supported on Si substrate, as shown in Fig. 1 [5]. The existence of a mobile surface layer with lower $T_g$ than that of bulk polymer was directly confirmed by scanning probe microscopy (SPM) [23, 24]; hence, a two-layer model consisting of a mobile surface layer and internal bulk-like layer is often used to describe the thickness dependence of PS thin films. In the case of freely standing PS thin films, which have two air–polymer interfaces, a much more drastic reduction in $T_g$ was reported by Forrest and coworkers [25, 26]. The reduction in $T_g$ with decreasing film thickness was thought to be a universal feature of polymer thin films; however, this is not so. An increase in $T_g$ with decreasing film thickness was observed for poly(methyl methacrylate) (PMMA) thin films supported on Si substrate with native oxide [3] due to strong interfacial interaction between the PMMA thin film and the Si substrate.

Singular physical properties of the surface or interfacial region of polymer thin films are not only observable from the thickness dependence of $T_g$ but also from the other thermal properties of polymer thin films. A reduction in thermal expansivity with thickness reported by Miyazaki et al. [7] and DeMaggio et al. [14] is also related to the anomalous surface or interfacial properties of polymer thin films. In fact, DeMaggio et al. [14] used a three-layer model consisting of surface, bulk-like layer, and interfacial layer to describe the thickness dependence of thermal expansivity in the molten state, implying that both surface and interfacial effects cannot be ignored in describing the resulting physical properties of polymer thin films. Considering the so far reported results, a homogenous structure is no longer appropriate for the description of the physical properties of polymer thin films but instead a heterogeneous structure considering the singularity of surface or interfacial effects is necessary. If a heterogeneous structure were the real nature of polymer thin films, a distribution of physical properties including $T_g$ in thin films would be expected, as pointed out by de Gennes [27] and Jones [28]. Experimentally, Torkelson et al. [29] first succeeded in evaluating the distribution of $T_g$ in polymer thin films by fluorescence and multilayer methods and confirmed the existence of a distribution of $T_g$ or a multilayered structure of $T_g$ in thin films. Their results further reinforce the necessity to investigate the heterogeneous structure of polymer thin films.

Heterogeneity of polymer thin films was confirmed not only by static measurements but also from dynamic measurements. Fukao and Miyamoto [9] reported that the dielectric loss spectrum near $T_g$ became broader with decreasing film thickness by dielectric relaxation. Kajiyama and coworkers [23, 24] used SPM to show that the apparent activation energy for the $\alpha_a$-relaxation process at the surface region was smaller than that of bulk polymer near bulk $T_g$, implying a higher mobility at the surface region. Kim et al. [30] studied the surface dynamics near $T_g$ by X-ray photon correlation spectroscopy (XPCS) and found that the acceleration of dynamics at the surface region was similar to that of bulk. These studies directly revealed the dynamic heterogeneity of polymer thin films; however, adequate experimental approaches are still lacking due to experimental difficulties. Further detailed and fruitful analyses from the perspective of the dynamic heterogeneity of polymer thin films are strongly desired and such approaches would offer better opportunities for understanding the unresolved problems of polymer thin films.

## 3 Basic Principles of Inelastic and Quasielastic Neutron Scattering

For better understanding of the present review, we include a brief account of the basic principles of inelastic and quasielastic scattering. For more detailed information and equations, the reader is referred to other books [31, 32].

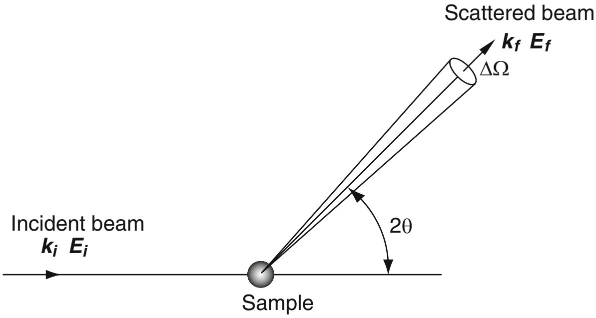

**Fig. 2** Schematic view of the neutron scattering process. See text for details

In the case of inelastic or quasielastic scattering, the observable parameter is the double differential scattering cross-section $\mathrm{d}^2\sigma/\mathrm{d}\Omega\mathrm{d}E$, which is the probability that an incident neutron with wave vector $k_\mathrm{i}$ and energy $E_\mathrm{i}$ is scattered by $2\theta$ into a solid angle $\mathrm{d}\Omega$ and with neutron energy in the range $\mathrm{d}E$, as indicated in Fig. 2. The double differential scattering cross-section is related to the dynamic scattering:

$$\frac{\partial^2\sigma}{\partial\Omega\,\partial E} = \frac{1}{4\pi}\frac{k_\mathrm{f}}{k_\mathrm{i}}N[\sigma_\mathrm{inc}S_\mathrm{inc}(\boldsymbol{Q},\omega) + \sigma_\mathrm{coh}S_\mathrm{coh}(\boldsymbol{Q},\omega)], \tag{1}$$

where $\boldsymbol{Q}$ is the scattering vector, $\omega$ the neutron frequency, $S_\mathrm{inc}(\boldsymbol{Q}, \omega)$ and $S_\mathrm{coh}(\boldsymbol{Q}, \omega)$ are the incoherent and coherent scattering laws, $\sigma_\mathrm{inc}$ and $\sigma_\mathrm{coh}$ are the incoherent and coherent scattering cross-sections, and $N$ is the number of atoms. The incoherent and coherent dynamic scattering laws are related to incoherent and coherent intermediate scattering functions $I_\mathrm{s}(\boldsymbol{Q}, t)$ and $I(\boldsymbol{Q}, t)$, respectively, through the Fourier transformation:

$$S_\mathrm{inc}(\boldsymbol{Q},\omega) = \frac{1}{2\pi}\int_{-\infty}^{\infty} I_\mathrm{s}(\boldsymbol{Q},t)\,\exp(-\mathrm{i}\omega t)\,\mathrm{d}t, \tag{2}$$

$$S_\mathrm{coh}(\boldsymbol{Q},\omega) = \frac{1}{2\pi}\int_{-\infty}^{\infty} I(\boldsymbol{Q},t)\,\exp(-\mathrm{i}\omega t)\,\mathrm{d}t. \tag{3}$$

$I_\mathrm{s}(\boldsymbol{Q}, t)$ and $I(\boldsymbol{Q}, t)$ are defined by following equations:

$$I_\mathrm{s}(\boldsymbol{Q},t) = \frac{1}{N}\sum_k \langle \exp\{-\mathrm{i}\boldsymbol{Q}\boldsymbol{r}_k(0)\}\exp\{\mathrm{i}\boldsymbol{Q}\boldsymbol{r}_k(t)\}\rangle, \tag{4}$$

$$I(\boldsymbol{Q},t) = \frac{1}{N}\sum_k\sum_l \langle \exp\{-\mathrm{i}\boldsymbol{Q}\boldsymbol{r}_k(0)\}\exp\{\mathrm{i}\boldsymbol{Q}\boldsymbol{r}_l(t)\}\rangle. \tag{5}$$

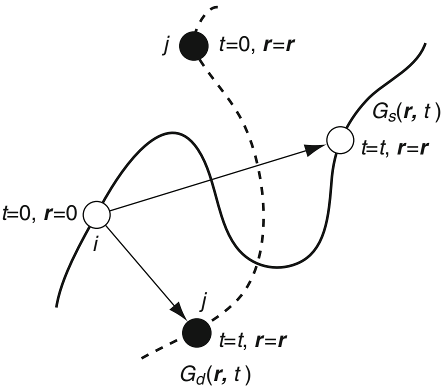

**Fig. 3** Schematic view of Van Hove correlation functions. See text for details

Furthermore, incoherent and coherent dynamic scattering laws $S_{\mathrm{inc}}(\boldsymbol{Q}, \omega)$ and $S_{\mathrm{coh}}(\boldsymbol{Q}, \omega)$ are described by the time–space Fourier transformations of the time–space self- and pair-correlation functions $G_{\mathrm{s}}(\boldsymbol{r}, t)$ and $G(\boldsymbol{r}, t)$:

$$S_{\mathrm{inc}}(\mathbf{Q},\omega) = \frac{1}{2\pi}\int_{-\infty}^{\infty}\int_{0}^{\infty} \mathrm{d}\boldsymbol{r}\,\mathrm{d}t\, G_{\mathrm{s}}(\boldsymbol{r},t)\, \exp[\mathrm{i}(\boldsymbol{Q}\boldsymbol{r}-\omega t)], \tag{6}$$

$$S_{\mathrm{coh}}(\boldsymbol{Q},\omega) = \frac{1}{2\pi}\int_{-\infty}^{\infty}\int_{0}^{\infty} \mathrm{d}\boldsymbol{r}\,\mathrm{d}t\, G(\boldsymbol{r},t)\, \exp[\mathrm{i}(\boldsymbol{Q}\boldsymbol{r}-\omega t)]. \tag{7}$$

We also need to remark that the Van Hove correlation function $G_{\mathrm{d}}(\boldsymbol{r}, t)$ is used in the analysis of inelastic neutron scattering from liquids and is defined by:

$$G(\boldsymbol{r},t) = G_{\mathrm{s}}(\boldsymbol{r},t) + G_{\mathrm{d}}(\boldsymbol{r},t) \tag{8}$$

and is called the distinct correlation function. Assuming that a particle exists at position $\boldsymbol{r} = 0$ at time $t = 0$, then $G_{\mathrm{s}}(\boldsymbol{r}, t)$ gives the probability of finding the same particle in an interval $\mathrm{d}\boldsymbol{r}$ at $\boldsymbol{r}$ and at $t = t$. $G_{\mathrm{d}}(\boldsymbol{r}, t)$ is the probability of finding another particle in an interval $\mathrm{d}\boldsymbol{r}$ at $\boldsymbol{r}$ and at $t = t$. The physical meaning of $G_{\mathrm{d}}(\boldsymbol{r}, t)$ and $G_{\mathrm{s}}(\boldsymbol{r}, t)$ is schematically depicted in Fig. 3.

If the distribution of particle displacements $[r_k(t) - r_k(0)$ or $r_k(t) - r_l(0)]$ are described by a Gaussian distribution, then the incoherent and coherent intermediate scattering functions can be written, respectively, in terms of $Q^2$ only as:

$$I_{\mathrm{s}}(\boldsymbol{Q},t) = \frac{1}{N}\sum_{k}\exp\left\{-\frac{Q^2}{6}\left\langle ((r_k(t)-r_k(0))^2\right\rangle\right\}, \tag{9}$$

$$I(\boldsymbol{Q},t) = \frac{1}{N}\sum_{k}\sum_{l}\exp\left\{-\frac{Q^2}{6}\left\langle ((r_k(t)-r_l(0))^2\right\rangle\right\}. \tag{10}$$

The time-dependent mean square displacement can be obtained from the incoherent scattering measurements. It is also pointed out that the frequency-dependent mean square displacement can be obtained from the incoherent dynamic scattering law within the Gaussian approximation.

## 4 Glassy Dynamics of Polymer Thin Films in the Picosecond Region

In this section, we focus on glassy dynamics in the millielectronvolt (meV) or picosecond region including low energy excitation, which is responsible for the excess heat capacity of amorphous solids at 10–30 K [33–35], and the picosecond localized relaxation process, the "fast process" [36–38], in polymer thin films. Inelastic and quasielastic neutron scattering were used in order to understand the effect of heterogeneous structure on these localized glassy dynamics. The dynamic heterogeneity of polymer thin films in terms of non-Gaussian parameters [20, 39] was also studied utilizing a high $Q$ accessible chopper spectrometer.

Before discusssing the details of dynamics from inelastic and quasielastic neutron scattering from polymer thin films, examples are given of the observed dynamic scattering law $S(Q, \omega)$ of PS thin films with thicknesses of 1,000 and 400 Å at temperatures from 11 to 408 K (Fig. 4a, b). A broad inelastic peak, the low energy excitation or so-called Boson peak, which is characteristic of amorphous systems, was observed at around 1.5 meV at temperatures lower than 200 K. With increasing temperature, the shape of the spectrum changed from inealstic-like to quasielastic-like, implying the onset of a relaxation process or anharmonic motion.

First we analyzed the elastic scattering intensity $I_{\mathrm{el}}(Q)$ to evaluate the mean square displacement $\langle u^2 \rangle$. $\langle u^2 \rangle$ can be evaluated from the $Q^2$ dependence of incoherent elastic scattering intensity through $I_{\mathrm{el}}(Q) = \exp[-\langle u^2 \rangle Q^2]$. The temperature dependence of evaluated $\langle u^2 \rangle$ is shown in Fig. 5 for the bulk polymer and for thin films with a thickness of 1,000 and 400 Å. $\langle u^2 \rangle$ is almost proportional to temperature $T$ in the temperature range below 200 K, implying that the dynamics are mainly dominated by harmonic motion. With increasing temperature, $\langle u^2 \rangle$ began to deviate from a linear relationship and showed an extra anharmonic contribution. The examined temperature range covered the bulk $T_{\mathrm{g}}$, but we could not detect the corresponding anharmonic contribution or excess increase at around bulk $T_{\mathrm{g}}$, even for bulk sample. This implies that the energy resolution used ($\delta E \sim 0.20$ meV) was not enough to detect glass transition or $\alpha$ process [40]. The results from high-energy resolution measurements will be given in Sect. 5. The most important point from Fig. 5 is that $\langle u^2 \rangle$ decreased with the film thickness within the temperature range examined, indicating that the molecular mobility decreased with thickness.

Two possible reasons for the decrease in $\langle u^2 \rangle$ with thickness were considered. The first reason is the hardening due to polymer chain confinement in a thin film.

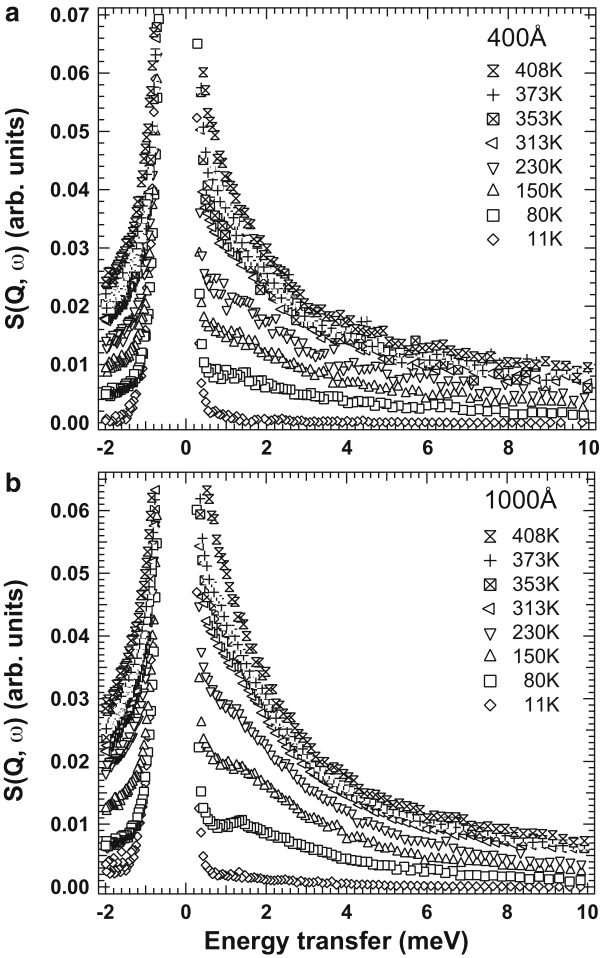

**Fig. 4** Dynamic scattering law $S(Q, \omega)$ of PS thin films of thickness (**a**) 400 Å and (**b**) 1,000 Å at various temperatures, as indicated

In a thin film below polymer coil size, which can be represented by twice the radius of gyration ($2R_g$) [41], the polymer chains cannot sustain the normal coil form and deformation of the coil would occur as shown in Fig. 6a. Small angle neutron scattering (SANS) studies revealed that polymer chain conformation in thin films was different to that in bulk states [42, 43]. Such deformed polymer chains would have higher restoring force than that of a normal coil, resulting in the decrease in chain mobility with thickness. A second reason for the decrease in $\langle u^2 \rangle$ with thickness is the existence of a hard layer or low mobility layer [14], which would exist at the interface between the polymer thin film and the substrate (Fig. 6b). With decreasing film thickness, the fraction of such hard layer becomes large, under the assumption that the thickness of the hard layer is independent of the total film thickness.Which is the main reason for the decrease in $\langle u^2 \rangle$ with decreasing film thickness? In order to answer this problem, PS thin films with the same film

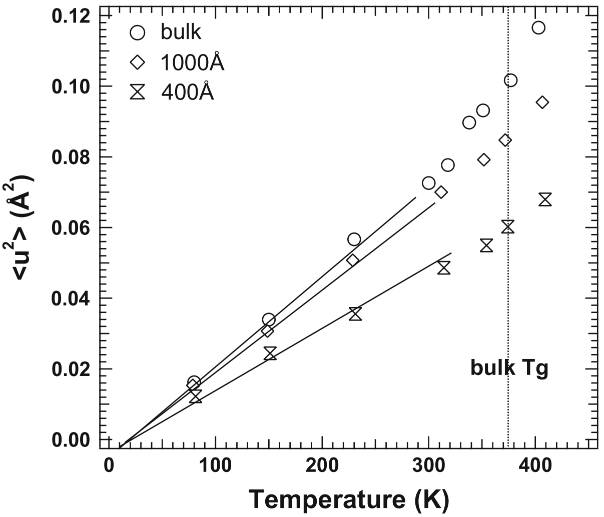

**Fig. 5** Temperature dependence of mean square displacement $\langle u^2 \rangle$ for bulk PS and thin films of 1,000 and 400 Å

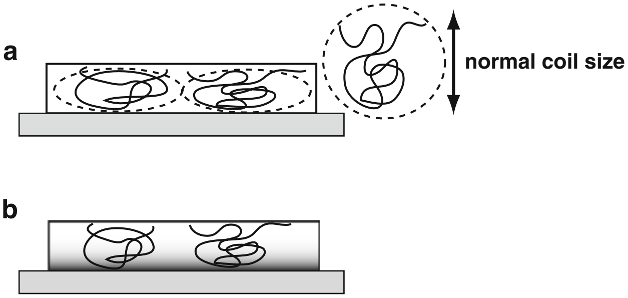

**Fig. 6** Molecular pictures illustrating the reduction in mobility with thickness: (**a**) deformation of polymer chain and (**b**) hard layer at the interface

thickness for different molecular weight ($M_w$) were prepared, giving different ratios of the film thickness ($d$) to $2R_g$. If the confinement effect were dominant, a decrease in $\langle u^2 \rangle$ would be expected with the decrease in $d/2R_g$ because changing the ratio $d/2R_g$ means the changing of degree of confinement. If the interfacial effect were dominant, $\langle u^2 \rangle$ would be constant regardless of the ratio $d/2R_g$ (within experimental error) because the ratio of the interfacial layer to total film thickness is constant. Investigating the dependence of $\langle u^2 \rangle$ on $M_w$ would offer a direct clue as to whether a homogenous structure (confinement effect) or a heterogeneous structure (interfacial effect) was reasonable. The temperature dependence of evaluated $\langle u^2 \rangle$ for different $M_w$ is shown in Fig. 7. Evaluated values of $\langle u^2 \rangle$ for different $M_w$ lie on a straight line

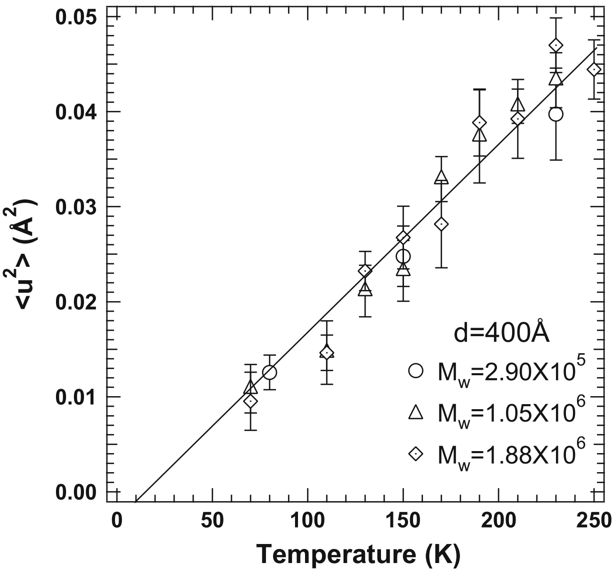

**Fig. 7** Temperature dependence of mean square displacement $\langle u^2\rangle$ for 400 Å films of PS of different molecular weights

within experimental error, implying that $\langle u^2\rangle$ for a thin film of 400 Å thickness is independent of $M_w$ in the temperature range examined. In order to check the validity of our assumption, $\langle u^2\rangle$ was measured as a function of $d/2R_g$ and thickness $d$ (Fig. 8). It was found that $\langle u^2\rangle$ is only scaled by $d$, not $d/2R_g$, within the accuracy in the measurements. The procedure directly confirms that change of $\langle u^2\rangle$ with thickness is not dominated by deformation of the polymer coil but by an interfacial hard or low mobility layer. Hence, a heterogeneous structure seems to be suitable for explaining the dynamics of polymer thin films as revealed by INS.

The hard interfacial layer seems to be the physical reason for the decrease in $\langle u^2\rangle$ with decreasing thickness, as evaluated from elastic scattering. However, we do not know the effect of the hard interfacial layer or heterogeneous structure on the resulting inelastic and quasielastic neutron scattering. As a next step, inelastic and quasielastic neutron scattering from polymer thin films was studied to understand the physical origin of the decrease in $\langle u^2\rangle$ with thickness. The observed $S(Q, \omega)$ was converted to the density of phonon states $G(\omega)$ [44] and the evaluated $G(\omega)/\omega^2$ values are shown in Fig. 9 for bulk polymer and thin films. A reduction in $G(\omega)$ with thickness was observed in the energy region 1–10 meV, suggesting that a decrease in $\langle u^2\rangle$ with thickness was responsible for the decrease in $G(\omega)$ because $\langle u^2\rangle$ is related to $G(\omega)$ through the relation [44]:

$$\langle u^2\rangle = \frac{3\hbar}{2M}\int_0^\infty \frac{1}{\omega}\coth\left[\frac{\hbar\omega}{2k_B T}\right]G(\omega)\,d\omega. \tag{11}$$

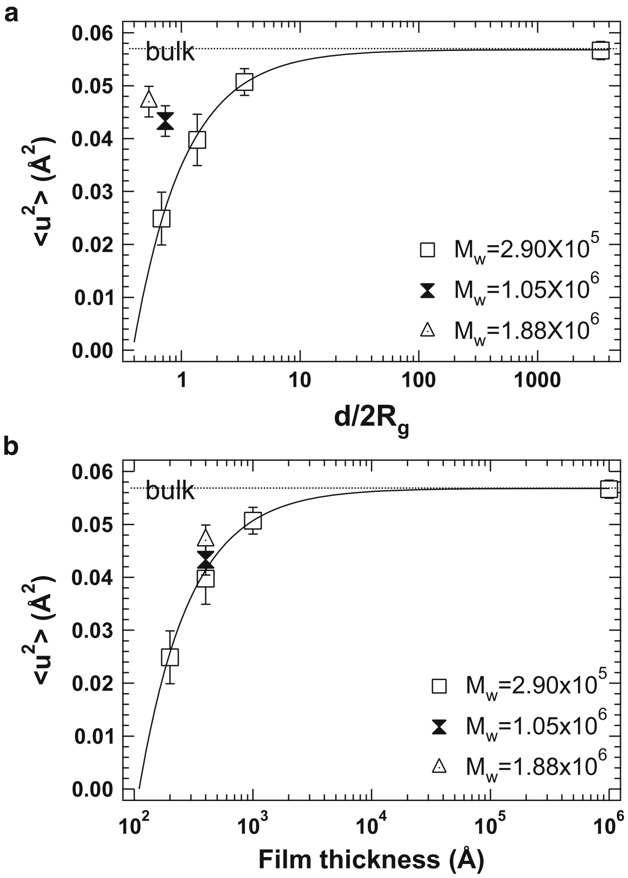

**Fig. 8** (**a**) $\langle u^2 \rangle$ as a function of the ratio of film thickness to twice the radius of gyration ($d/2R_g$) for PS of different molecular weights. (**b**) $\langle u^2 \rangle$ as a function of film thickness ($d$) for PS of different molecular weights

The thickness dependence of the calculated $\langle u^2 \rangle$ from $G(\omega)$ and the elastic scattering are also plotted in Fig. 10. A consistency was found between $\langle u^2 \rangle$ from elastic scattering and that from inelastic scattering, supporting the proper background correction for the observed inelastic scattering from polymer thin films.

In the energy region examined, there exist at least two modes. One is a localized mode (Boson peak mode) and the other is an extended mode (Debye mode). The decoupling of both modes is needed to understand which mode contributes to the decrease in $G(\omega)$ with thickness in the energy region below 10 meV. The contribution of the Debye mode in $G(\omega)$ was evaluated from the Debye frequency $\omega_D$ and the contribution from the Boson peak mode was obtained by subtracting the Debye contribution from the total $G(\omega)$ [45]. For the thin films, the Debye contributions were estimated assuming that the amplitude of Debye mode and Boson peak mode are independent of film thickness. The Debye contribution from bulk and thin films

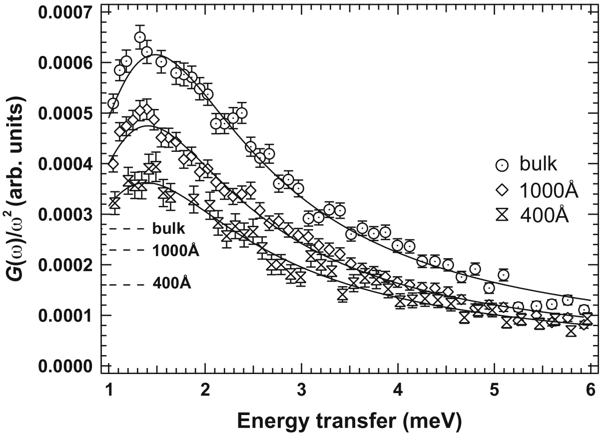

**Fig. 9** Density of phonon states $G(\omega)$ divided by $\omega^2$ for bulk PS and thin films of 1,000 and 400 Å; *dotted lines* show the Debye contribution

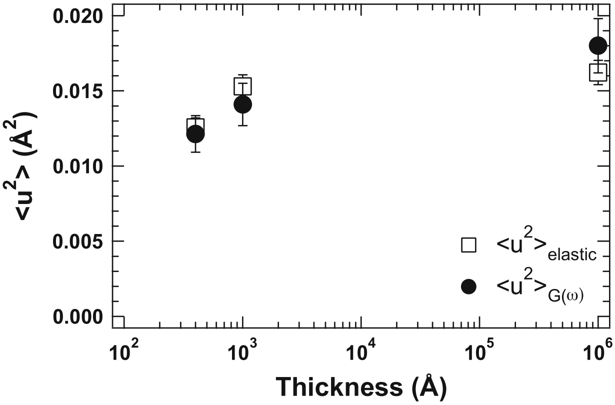

**Fig. 10** Thickness dependence of $\langle u^2 \rangle$ as evaluated from $Q^2$ dependence of the elastic scattering intensity (*squares*) and $\langle u^2 \rangle$ as calculated from $G(\omega)$ at 80 K (*circles*)

are included in Fig. 9 as dashed lines, showing the significant depression of intensity in both Debye mode $G_D(\omega)$ and Boson peak mode $G_b(\omega)$. It implies that the decrease in $\langle u^2 \rangle$ with thickness could be attributed to the decrease in both the Debye mode and the Boson peak mode. As for the Boson peak, the peak position is independent of film thickness within experimental error. If we assume that peak energy is given by $\omega = \sqrt{f/m}$, where $f$ is the harmonic force constant and $m$ the effective mass, the present result implies that $f$ is constant regardless of film thickness. That is to say, the effect of hardening on the Boson peak mode seems to be quite small. The physical origin of the decrease in intensity of both modes with decreasing film thickness must be considered independently.

The density of phonon states of Debye mode $G_D(\omega)$ is related to the average sound velocity $v$ through the relation $G_D(\omega) = \frac{4\pi V \omega^2}{v^3}$, where $V$ is the average atomic volume [46]. The reduction in $G_D(\omega)$ is the increase in sound velocity ($v$) due to the densification with decreasing film thickness. It was reported that polymer chains tend to form an ordered structure, exhibiting layering near the interface between thin film and the substrate [47, 48]. Gautam et al. [48] investigated the molecular structure of PS at the interface between polymer thin film and the substrate using IR–visible sum-frequency (SFG) spectroscopy and observed a preferred perpendicular orientation of the phenyl group with respect to the surface normal, indicating the in-plane orientation of the main chain at the interface between polymer thin film and substrate. The density of the layer at the interface must become larger due to such an ordered structure, resulting in an increase in $v$ with decreasing film thickness. The ordered layer acts as a hard layer and results in a decrease in the Debye contribution $G_D(\omega)$.

As for Boson peak mode, earlier experimental results for bulk glass-formers offer useful information for the interpretation of our results. Inamura et al. [49] investigated the densification effect on Boson peak with $SiO_2$ glass and found that the intensity of the Boson peak decreased drastically just through the densification, as shown in Fig. 11a. For the polymer system, we [50] studied the effect of annealing on the Boson peak using PMMA bulk samples (Fig. 11b) and observed that Boson peak intensity decreased after annealing at 20 K below bulk $T_g$, without affecting the position of the Boson peak. Densification or annealing is a kind of structural change from the disordered state to the ordered state; hence, the physical origin of the Boson peak seems to be related to defects or voids or to structural disorder [51–53]. If there existed an ordered structure or hard interfacial layer at the interface between polymer thin film and substrate, it would result in a decrease in $G_b(\omega)$ with decreasing film thickness due to the high contribution from such an ordered layer. This situation results in a decrease in sites or voids for the Boson peak mode only, hence no shift of the Boson peak would be observed regardless of film thickness. The hard interfacial layer also seems to explain the decrease in both the Debye mode and the Boson peak mode and the idea of the existence of a hard layer is also applicable for the explanation of the thickness dependence of inelastic scattering behavior.

The observed dynamic scattering law $S(Q, \omega)$ was scaled by the Bose population factor after the correction for the Debye–Waller factor. The scaled spectra are shown in Fig. 12a for thin films with a thickness of 1,000 Å. The spectra were well scaled in the energy range at around 1.5 meV; on the other hand, excess scattering was observed below 1.5 meV with increasing temperature above about 200 K, suggesting the onset of the so-called fast process. The integrated scaled spectrum in the quasielastic region (0.70–1.5 meV) are plotted against temperature in Fig. 12b for the bulk polymer and for thin films of 1,000 and 400 Å. The temperature dependence of the integrated intensity for the 400 Å thin film is almost flat compared to those for the other film thicknesses in a low temperature region below ~230 K. The results suggest that the quasielastic scattering becomes more difficult in the thinner films. In order to study the characteristic features of the fast process in more detail, the model fit to the observed dynamic scattering law $S(Q, \omega)$ was performed and the following model function was employed for fitting [54]:

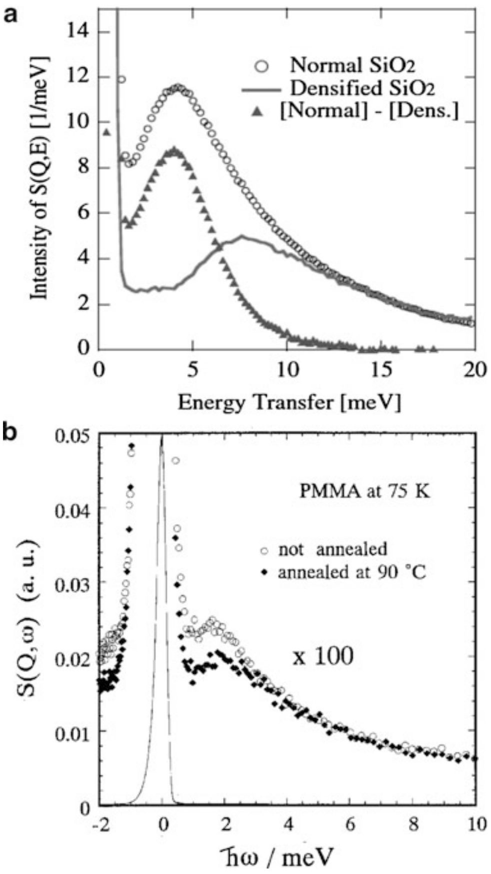

**Fig. 11** (**a**) Dynamic scattering law $S(Q, \omega)$ of normal $SiO_2$ (*circles*) and densified $SiO_2$ (*solid line*) [49]. (**b**) Dynamic scattering law $S(Q, \omega)$ of PMMA, not annealed and annealed at 363 K [50]. The solid line corresponds to the observed full spectra and the solid symbols in (b) correspond to magnified sepctra with the scale factor of 100 (×100). PMMA at 75 K means $S(Q, \omega)$ of PMMA measured at 75 K

$$S(Q, \omega) = C(Q)[\{1 - A_{\text{fast}}(Q)\}\delta(\omega) + A_{\text{fast}}(Q)L(\Gamma, \omega)] + B(Q), \tag{12}$$

where $A_{\text{fast}}(Q)$ is a fraction of the fast process, and $\delta(\omega)$ and $L(\Gamma, \omega)$ are a $\delta$-function and a Lorentzian with half-width at half-maximum (HWHM) $\Gamma$, respectively. $C(Q)$ and $B(Q)$ are constants representing the Debye–Waller factor and inelastic flat background, respectively. The results of the fits for the 1,000 and 400 Å films at 408 K are shown in Fig. 13 and the observed spectra were well fitted with Eq. (12). The logarithms of the relaxation rate $\Gamma$ and the fraction $A_{\text{fast}}(Q)$ are plotted against inverse of $T$ in Fig. 14 for the bulk polymer and the 1,000 and 400 Å films. We found that $\Gamma$ was more or less independent of film thickness, indicating that dynamics were not affected by film thickness. The most important point in Fig. 14 is that the fraction $A_{\text{fast}}(Q)$ decreased with the film thickness, and a similar decrease in intensity with the decrease in film thickness was also observed for the Boson peak. Comparing the thickness dependence of intensity or other properties like relaxation time, Boson peak intensity and the fast process is a fascinating approach for understanding the correlation between the fast process and Boson peak

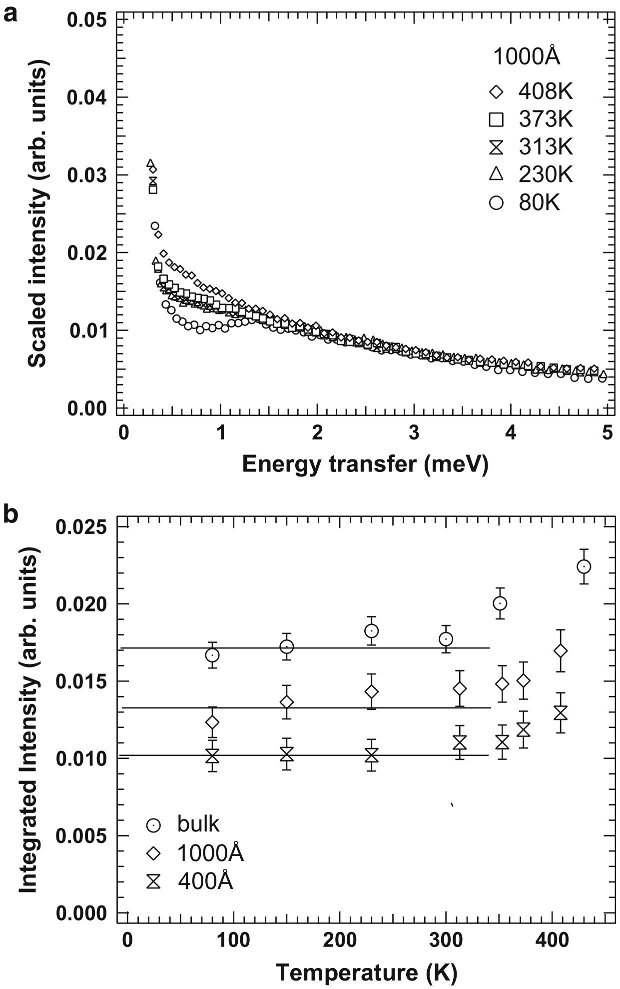

**Fig. 12** (**a**) Bose-scaled inelastic scattering intensity at different temperatures after correcting for the Debye–Waller factor for PS thin films with a thickness of 1,000 Å. (**b**) Temperature dependence of integrated intensity of the Bose-scaled spectra in the energy range of 0.70–1.5 meV for bulk PS and thin films of 1,000 and 400 Å

in thin films. The thickness dependence of $G_b(\omega)$ and $A_{fast}(Q)$, which were normalized by those for bulk sample, and the thickness dependence of $\Gamma$ and peak position of the Boson peak are plotted in Fig. 15. The thickness dependence of $G_b(\omega)$ and $A_{fast}(Q)$ are quite similar. Both the relaxation rate $\Gamma$ of the fast process and the characteristic energy of the Boson peak are close to each other and are independent of the film thickness, indicating that the physical origin of the Boson peak and fast process are the same. From the thickness dependence of the Boson

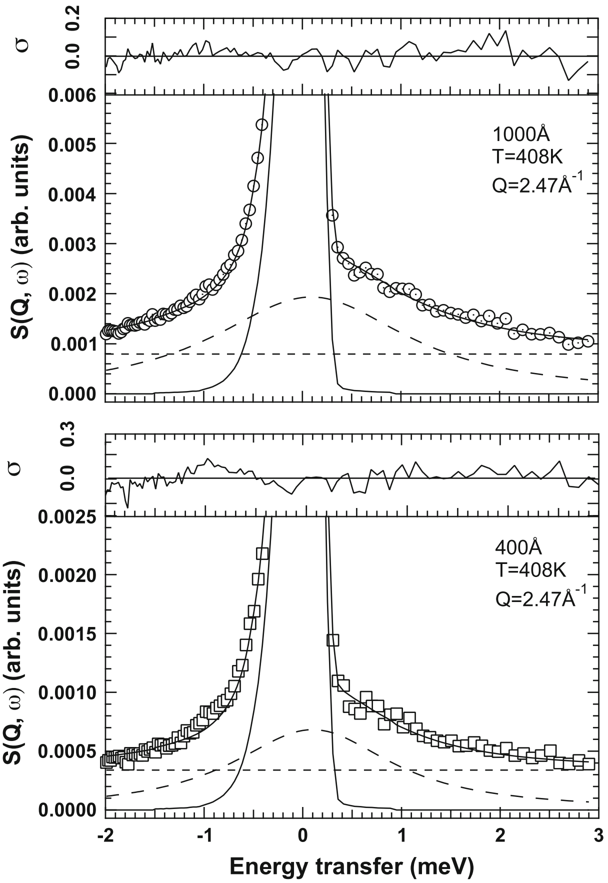

**Fig. 13** Results of curve fit with Eq. (12) to the spectra of (**a**) 1,000 Å and (**b**) 400 Å thin PS films measured at a temperature of 408 K. The solid lines, which are overlapped the solid symbols are the results of curve fit with (12) and the other solids line corresponds to resolution function. (------) and (- - - - - ) corresponds to flat background and lorentzian, respectively

peak mode, we suggest that the decrease in $G_b(\omega)$ is caused by the existence of hard interfacial layer; hence, a reduction in the fraction of fast process can also be attributed to an oriented interfacial layer.

Through the thickness dependence of elastic, inelastic, and quasielastic scattering in the millielectronvolt (or picosecond) region, it was found that the fast picosecond dynamics of polymer thin films was not described by homogenous dynamics but by heterogeneous dynamics, which were attributed to the orientation of molecular chains at the interface between polymer thin film and substrate.

We found that the existence of a hard interfacial layer was indispensable for the description of decreased mobility of polymer thin films with film thickness, implying that the heterogeneous structure was more enhanced with decreasing film thickness. Elucidating the heterogeneous structure of polymer thin films quantitatively is

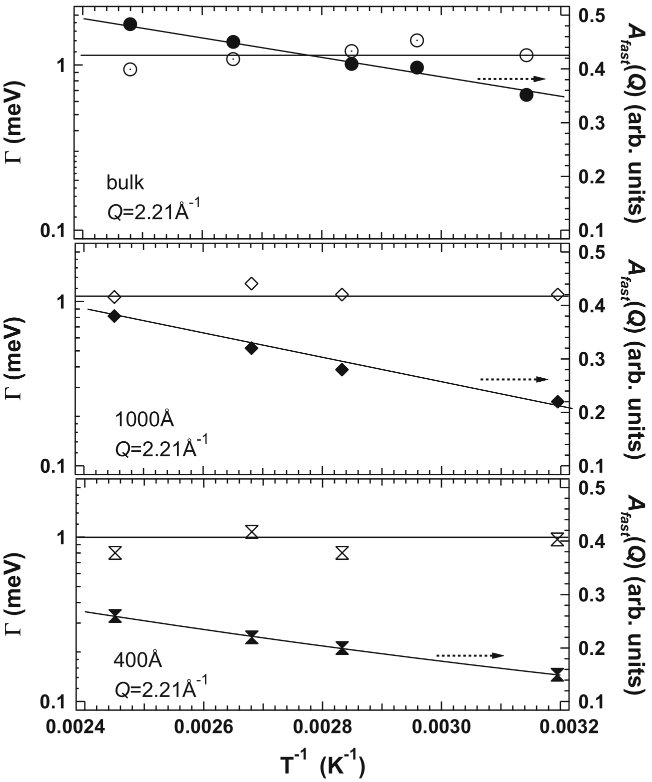

**Fig. 14** Temperature dependence of relaxation rate $\Gamma$ (*open symbols*) and fraction $A_{\text{fast}}(Q)$ of the fast process (*solid symbols*) for bulk PS and thin films of 1,000 and 400 Å

the target for understanding the unusual properties of thin films. The dynamic heterogeneity of polymer thin films in terms of the non-Gaussian parameter $A_0$ was then studied. In addition to the investigation on dynamic heterogeneity in thin films, we also studied the dynamic anisotropy; therefore, two scattering geometries (transmission and reflection geometries) were used, as shown in Fig. 16. In the transmission geometries the scattering vector $Q$ is almost parallel and in reflection geometries it is perpendicular to the film surface; hence, the molecular motion parallel and perpendicular to the surface direction was studied. For the evaluation of dynamic anisotropy and heterogeneity, the $Q$ dependence of $I_{\text{el}}(Q)$ must be evaluated.

Figure 17 indicates the $Q^2$ dependence of $I_{\text{el}}(Q)$ for the 1,000 and 200 Å films in the transmission and reflection geometries at 230 K, which were divided by $I_{\text{el}}(Q)$ at the lowest temperature. As seen in Fig. 17, $I_{\text{el}}(Q)$ cannot be described within the Gaussian approximation $I_{\text{el}}(Q) = \exp[-\langle u^2 \rangle Q^2]$, deviating in a high $Q$ region above about 2.5 Å$^{-1}$ due to higher order terms of $Q$. In order to describe the $Q$ dependence of $I_{\text{el}}(Q)$ properly, higher order terms of $Q$ must be taken into consideration. The non-Gaussian parameter was first introduced by Rhaman et al. [55]. According to

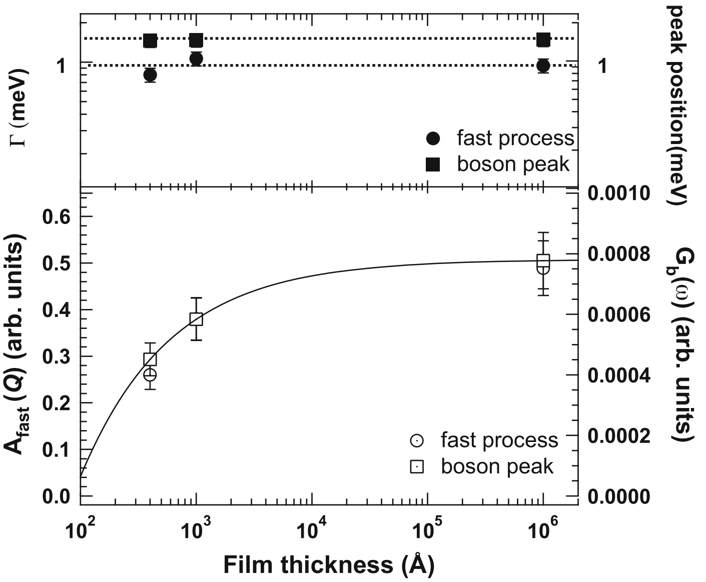

**Fig. 15** Thickness dependence of the fraction of fast process $A_{\text{fast}}(Q)$ (*open circles*), relaxation rate $\Gamma$ of fast process (*solid circles*), peak position of Boson peak (*solid squares*), and $G_{\text{b}}(\omega)$ (*open squares*)

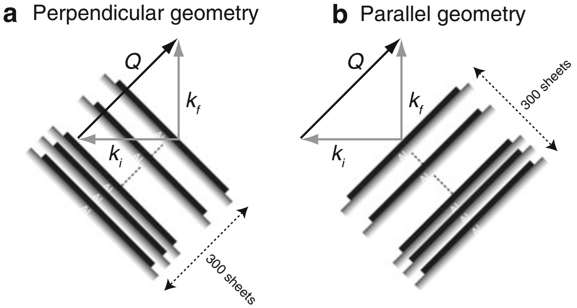

**Fig. 16** Sample geometry for dynamic anisotropy measurements: (**a**) perpendicular (reflection) geometry and (**b**) parallel (transmission) geometry

them, the incoherent intermediate scattering function $I(Q, t)$ is obtained from the cumulant expansion up to the order of $Q^4$ as follows:

$$I(Q,t) = \exp\left(-\langle u^2\rangle(t)Q^2 + \frac{1}{2}A_0(t)[\langle u^2\rangle(t)]^2Q^4\right). \tag{13}$$

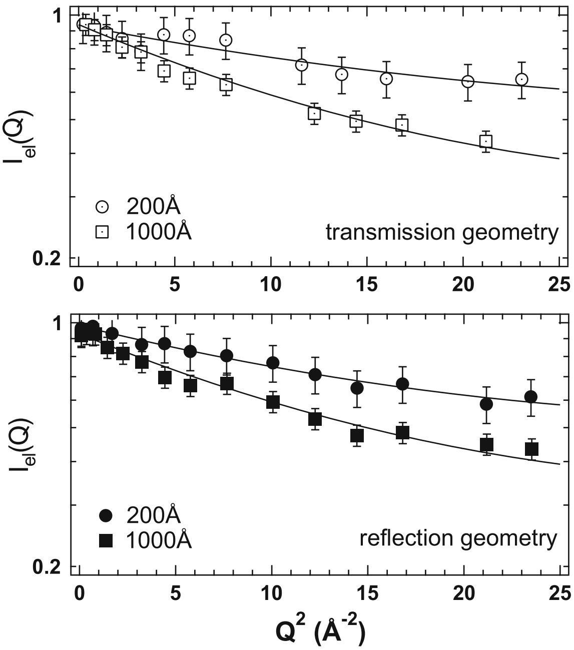

**Fig. 17** Dependence of the elastic scattering intensity ($I_{el}$) on $Q^2$ for 1,000 and 200 Å thin PS films in transmission and reflection geometries at 230 K. The *solid lines* are results of fit with Eq. (19)

In this expression, the integrals of the velocity correlation functions, denoted by $\gamma_1(t)$ and $\gamma_2(t)$ [55], have been expressed in terms of the mean square displacement $\langle u^2 \rangle$. The non-Gaussian parameter $A_0(t)$ is given by the expression:

$$A_0(t) = \frac{3\langle u^4 \rangle(t)}{5[\langle u^2 \rangle(t)]^2} - 1. \tag{14}$$

It has been shown by Zorn [39] that the non-Gaussian parameter could be due to different phenomena such as dynamic heterogeneity, anharmonicity, and dynamic anisotropy. From the studies on several polymeric glass-formers, the most plausible origin of non-Gaussian parameter $A_0$ of the glass-forming materials was attributed to dynamic heterogeneity due to the difference in local environments [20, 39]. The dynamic heterogeneity must be a leading term in the non-Gaussian parameter for polymer thin films in the glassy state.

If the motion in the individual environment is Gaussian, the intermediate scattering function $I(Q, t)$ is given by:

$$I(Q,t) = \exp(-\langle u^2 \rangle Q^2). \tag{15}$$

It is further assumed that the mean square displacement has a distribution $g(\langle u^2 \rangle)$. For simplicity of calculation, Gaussian distribution was assumed as follows:

$$g(\langle u^2\rangle) = \frac{1}{\sqrt{2\pi\sigma^2}} \exp\left(-\frac{\left(\langle u^2\rangle - \overline{\langle u^2\rangle}\right)^2}{2\sigma^2}\right), \tag{16}$$

where $\sigma^2 = \overline{\left(\Delta\langle u^2\rangle\right)^2} = \overline{\left(\langle u^2\rangle - \overline{\langle u^2\rangle}\right)^2}$. The incoherent intermediate scattering function $I(Q, t)$ up to the order of $Q^4$ is obtained by averaging over the distribution:

$$I(Q,t) = \exp\left(-\overline{\langle u^2\rangle} Q^2 + \frac{A_0 \overline{\langle u^2\rangle}^2}{2} Q^4\right), \tag{17}$$

where the non-Gaussian parameter $A_0$ is given by:

$$A_0 = \frac{\overline{\langle u^2\rangle^2} - \overline{\langle u^2\rangle}^2}{\overline{\langle u^2\rangle}^2}. \tag{18}$$

In this experiment, we observed dynamics in the frequency region; hence, the incoherent elastic scattering intensity of dynamic scattering law $S(Q, \omega = 0)$ is given by:

$$S(Q,\omega = 0) = \exp\left(-\overline{\langle u^2\rangle} Q^2 + \frac{1}{2} A_0 \overline{\langle u^2\rangle}^2 Q^4\right), \tag{19}$$

where $\langle u^2\rangle$ is the mean square displacement in the frequency region. Equation (19) was applied to fit to the observed data in Fig. 17 and the results are shown by solid curves, giving good agreements. From the fits by Eq. (19), the mean square displacement $\overline{\langle u^2\rangle}$ and the non-Gaussian parameter $A_0$ were evaluated. The temperature dependence of $\overline{\langle u^2\rangle}$ and $A_0$ are summarized in Fig. 18. As the film thickness decreases, $\overline{\langle u^2\rangle}$ decreases, which is consistent with Figs. 5, 8, and 10. The non-Gaussian parameter $A_0$ increases with decreasing temperature and film thickness, showing that the dynamic heterogeneity increases with decreasing temperature and film thickness. By comparing the results from transmission and reflection geometries we can also discuss the dynamic anisotropy for thin films. No dynamic anisotropy was observed for 1,000 Å thin film; however, a slight difference in $\overline{\langle u^2\rangle}$ value was observed for the 200 Å thin film. The $A_0$ value in the transmission geometry is slightly larger than that in the reflection geometry for the 200 Å film, which must come from the anisotropic motion. As mentioned above, the dynamic anisotropy also contributes to the increase in $A_0$; however, the observed dynamic anisotropy only contributes to an increase in $A_0$, of ~0.05, implying that the contribution of dynamic anisotropy to $A_0$ is more or less negligible in the present study.

To observe the film thickness dependence of $\overline{\langle u^2\rangle}$ and $A_0$ quantitatively, $\overline{\langle u^2\rangle}$ and $A_0$ at 230 K were plotted as a function of film thickness (Fig. 19). As the film thickness decreases, the non-Gaussian parameter increases, implying that the dynamic heterogeneity increases with a reduction in film thickness. Our studies

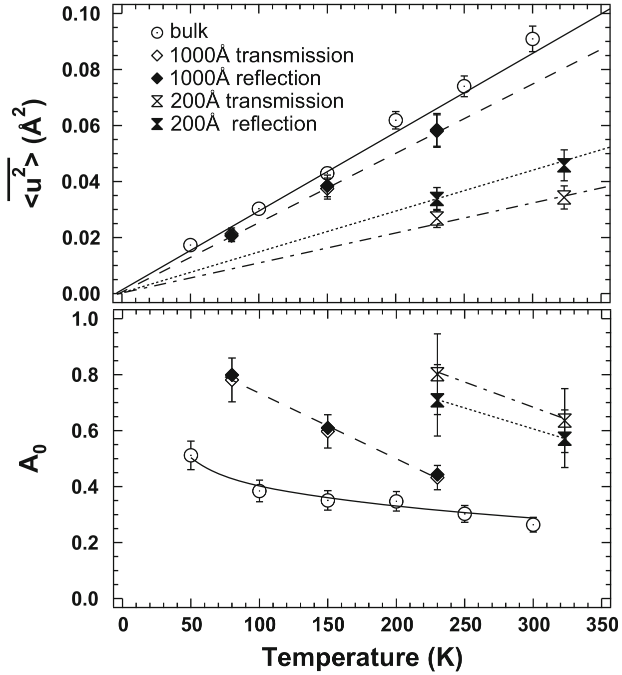

**Fig. 18** Temperature dependence of mean square displacement $\langle u^2 \rangle$ and non-Gaussian parameter $A_0$ for bulk PS and thin films of 1,000 and 200 Å in transmission and reflection geometries

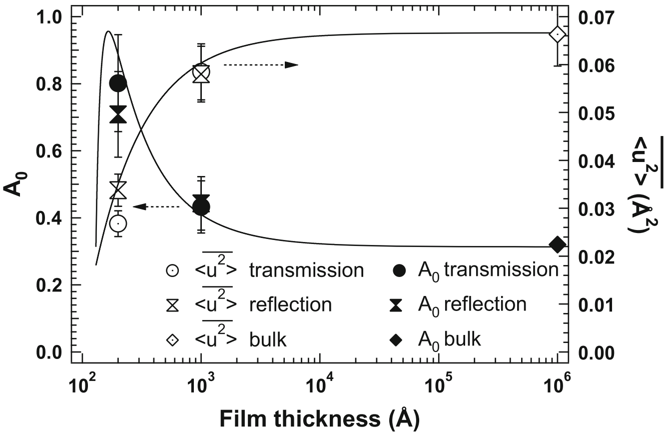

**Fig. 19** Film thickness dependence of mean square displacement $\langle u^2 \rangle$ (*open symbols*) and non-Gaussian parameter $A_0$ (*solid symbols*) for bulk PS and thin films of 1,000 and 200 Å at 230 K

on the $M_w$ dependence of $\langle u^2 \rangle$ have already shown that the interfacial layer is responsible for the decrease in $\langle u^2 \rangle$, therefore the increase in $A_0$ with decreasing film thickness reflects the multilayer structure of thin films or the existence of a hard interfacial layer. We tried to calculate $A_0$ as a function of film thickness based on a bilayer model, assuming that the thin film consists of a bulk-like layer and an interface hard layer. Under this assumption, $\overline{\langle u^2 \rangle}$ and $\overline{\langle u^2 \rangle}^2$ were calculated using Eqs. (20) and (21):

$$\overline{\langle u^2 \rangle} = \left(1 - \frac{\delta}{d}\right) \int \langle u^2 \rangle g(\langle u^2 \rangle)_{\text{bulk}}\, \mathrm{d}\langle u^2 \rangle + \frac{\delta}{d} \int \langle u^2 \rangle g(\langle u^2 \rangle)_{\text{dead}}\, \mathrm{d}\langle u^2 \rangle, \tag{20}$$

$$\overline{\langle u^2 \rangle}^2 = \left(1 - \frac{\delta}{d}\right) \int \langle u^2 \rangle^2 g(\langle u^2 \rangle)_{\text{bulk}}\, \mathrm{d}\langle u^2 \rangle + \frac{\delta}{d} \int \langle u^2 \rangle^2 g(\langle u^2 \rangle)_{\text{dead}}\, \mathrm{d}\langle u^2 \rangle, \tag{21}$$

where $d, \delta, g(\langle u^2 \rangle)_{\text{bulk}}$ and $g(\langle u^2 \rangle)_{\text{dead}}$ are the total thickness, the hard layer thickness, and distribution functions of $\langle u^2 \rangle$ in the bulk-like layer and in interfacial layer, respectively. The results of fit with a bilayer model are shown in Fig. 19 by solid curves, indicating that the bilayer model can describe the thickness dependence of observed $A_0$ and $\overline{\langle u^2 \rangle}$. In this calculation it was found that the thickness of the hard layer was ~130 Å and that $\overline{\langle u^2 \rangle}$ was ~0.018 Å$^2$ at 230 K. The value of $\overline{\langle u^2 \rangle}$ in the hard layer (~0.018 Å$^2$) at 230 K is very small compared with the bulk value (~0.066 Å$^2$).

The dynamic heterogeneity originating from a multilayer structure was evaluated based on the concept of non-Gaussian parameters. It was again confirmed that a heterogeneous dynamic structure was appropriate for the description of the dynamics of polymer thin films.

## 5 Glass Transition of Polymer Thin Films in the Nanosecond Region

In the previous section, the focus was on the glassy dynamics of polymer thin films and only the picosecond fast process was observed, even at temperatures above bulk $T_g$. The failure to detect the α process is due to a lack of energy resolution. We have studied the temperature dependence of $\langle u^2 \rangle$ with different energy resolutions, as shown in Fig. 20 [54]. In order to detect α processes properly, it seems that an energy resolution higher than about ~20 μeV is needed and such a high-energy resolution is possible with neutron backscattering [56] or neutron spin echo (NSE) [40]. In this section, we describe studies on the glass transition of polymer thin films using high-energy resolution spectrometry and ellipsometry.

The evaluated temperature dependence of $\langle u^2 \rangle$ with energy resolutions of 25 and 0.80 μeV for bulk PS and thin films with thicknesses of 1,000, 400 and 200 Å are shown in Fig. 21. $\langle u^2 \rangle$ decreased with decreasing film thickness in the temperature range examined and this tendency is consistent with the results from millelectronvolt

**Fig. 20** Temperature dependence of $\langle u^2 \rangle$ of bulk PS for various energy resolutions [54]

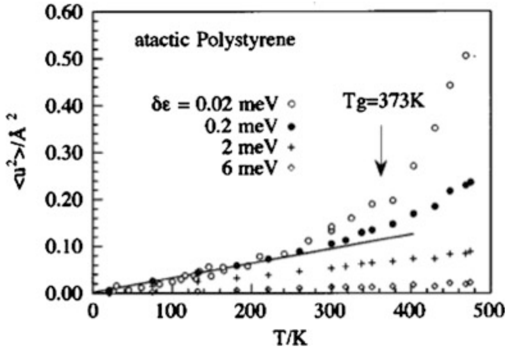

(or picosecond) dynamics. In addition to the steep increase in $\langle u^2 \rangle$ due to the onset of the fast process at around 200 K, a drastic increase in $\langle u^2 \rangle$ was observed at around 370 K, which corresponds to the glass transition temperature in bulk ($T_g = 373$ K), suggesting detection of the $\alpha$ process [40, 56, 57]. This onset temperature of the $\alpha$ process was used as a determination of $T_g$ by INS. The onset temperature of the $\alpha$ process shifted to higher temperature with decreasing film thickness, regardless of energy resolution. Ellipsometry measurements on PS thin films supported on Al-deposited Si substrates was also performed to realize similar substrate conditions as those used for INS measurements. The evaluated thickness dependence of $T_g$ from ellipsometry and INS measurements are summarized in Fig. 22. It is evident that the thickness dependencies of $T_g$ as measured by the two methods are completely contradictory. Similar contradiction in the thickness dependence of $T_g$ has already been reported by Soles et al. [58, 59]. The authors observed a decrease in $T_g$ with decreasing thickness for polycarbonate thin films from specular X-ray reflectivity (SXR) and positron annihilation lifetime spectroscopy (PALS) studies [58]. On the other hand, an increase in $T_g$ with decreasing film thickness was observed from INS studies, as shown in Fig. 23. Furthermore, Soles et al. also studied the dynamics of several amorphous polymer thin films by INS and found that $\langle u^2 \rangle$ decreased and $T_g$ increased with thickness for all the polymers investigated, regardless of the strength of interaction with substrates [59]. It seems that these anomalous phenomenon detected by INS might be related to certain aspects of polymer thin films.

Polymer thin film is a two-dimensionally confined system; hence, we would like to consider confined systems to find a plausible clue to the anomalous behavior. Schönhals et al. [60] studied the dynamics of glass-forming poly(methyl phenyl siloxane) (PMPS), which was confined to porous glass with a diameter in the nanometer range, using a combination of INS, dielectric relaxation, and temperature-modulated DSC to observe the anomalous dynamics compared to that of bulk polymer. The obtained relaxation time map for bulk PMPS and PMPS confined to nanoporous glass is shown in Fig. 24. For bulk PMPS, the temperature dependence of relaxation time was well described by the Vogel–Fulcher–Tammann (VFT) equation. On the other hand, the temperature dependence of relaxation time changed from a VFT equation to Arrhenius equation with a decrease in the diameter of the nanoporous

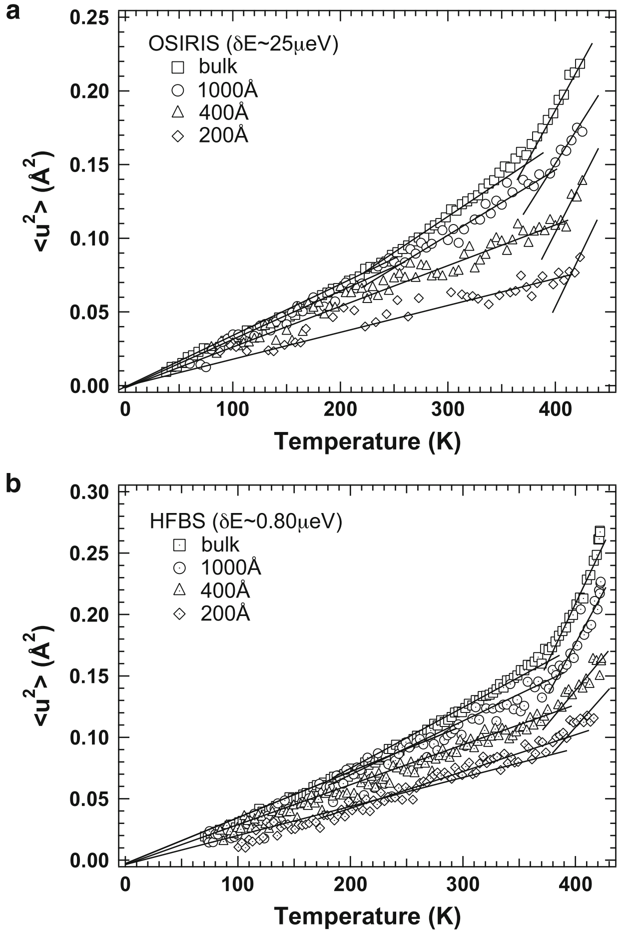

**Fig. 21** Temperature dependence of $\langle u^2 \rangle$ of bulk PS and thin films of 1,000, 400, and 200 Å for $\delta E$ of approximately (**a**) 25 μeV and (**b**) 0.80 μeV

glass, implying a decrease in activation energy with a reduction in pore size. Another interesting finding is that the relaxation times for bulk PMPS and other confined PMPS intersected at a certain temperature or frequency, which is here referred to as the "crossing point". Due to the existence of a crossing point in the relaxation time map, both acceleration and deceleration of dynamics were observable for PMPS confined to nanoporous glass compared to the bulk system. This implies that the contradiction dynamics was also possible for a confined PMPS system. Schönhals et al. discussed whether this change of dynamics by spatial confinement was attributed to the effect on a cooperatively rearranging region (CRR) [61]. For bulk glass-former, the size of CRR can extend adequately without any other spatial hindrance and the temperature dependence of relaxation time was described by a Vogel–Fulcher-type equation. With decreasing pore size, the glass-former cannot extend the CRR to the entire

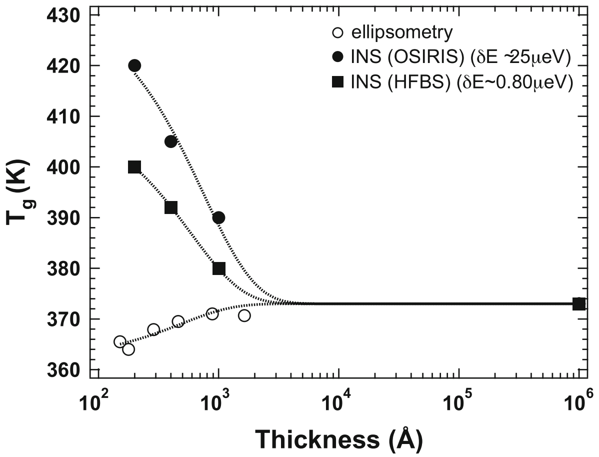

**Fig. 22** Thickness dependence of $T_g$ evaluated from INS with two different energy resolutions and by ellipsometry

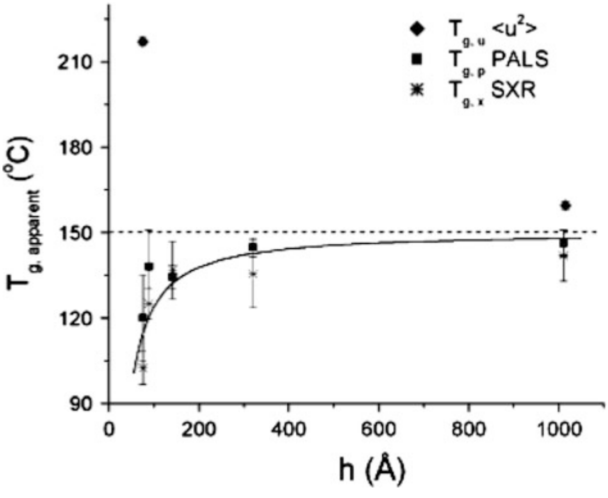

**Fig. 23** Thickness ($h$) dependence of $T_g$ evaluated from INS, PALS, and SXR of polycarbonate thin films [58]

system due to the limited pore diameter, resulting in the decrease in cooperativity or the onset of self-motion. The decrease in cooperativity means a decrease in activation energy; hence, a decrease in activation energy was observed with decreasing pore size. The above explanation is schematically summarized in Fig. 25.

Is the decrease in activation energy sufficient to realize the existence of a crossing point in the relaxation time map? If only the change of activation energy occurred, the crossing point in relaxation time map would be realized at extremely high temperature

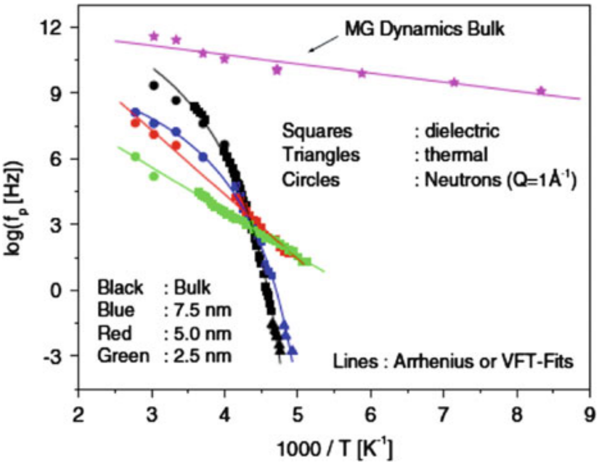

**Fig. 24** Relaxation time map of bulk PMPS and PMPS films of different thicknesses confined to nanoporous glass, as observed with dielectric spectroscopy, thermal analysis, and INS [60]

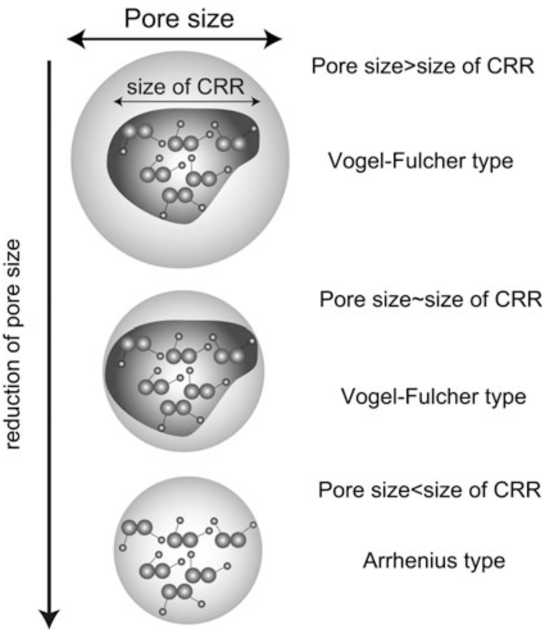

**Fig. 25** Effect of spatial confinement on the cooperatively rearranging region (CRR)

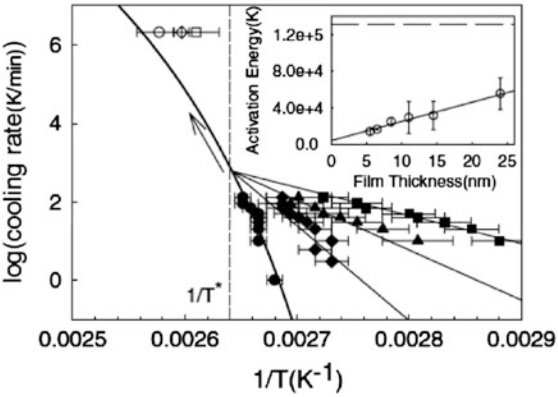

**Fig. 26** The log(cooling rate) versus 1/*T* for PS thin films supported on Si substrate. *Inset* indicates the thickness dependence of activation energy [63]. Solid symbols represent PS thin films with different film thicknesses

or high frequency regions, which are not experimentally accessible. It is considered that the existence of an impenetrable wall would affect the resulting dynamics and, in fact, the dynamics of confined PMPS at a high frequency region was drastically slower than that of bulk polymer. These results imply that the segmental motion is strongly hindered by an effect of the wall surface, meaning a reduction in motional freedom. Both reduction in activation energy with decreasing pore size and a wall effect [62] are necessary to realize the anomalous dynamics observed for spatially confined glass-former.

Considering the analogy between the results of Schönhals et al. [60] and our results, the relaxation time map can serve as a supporting material for understanding our results. Hence, we tried to prepare a schematic relaxation time map for polymer thin films. As for the activation energy of thin films, Fakhraai and Forrest [63] investigated the thickness dependence of activation using ellipsometry with different cooling rates, as shown in Fig. 26, and found that the activation energy of the $\alpha$ process decreased at thicknesses below 61 nm. Interestingly, the temperature dependence of the relaxation rate was not described by a Vogel–Fulcher-type equation but by an Arrhenius type for the thinnest film investigated. Compared to the reported size of CRR for PS (~3 nm) [64, 65], the onset film thickness for the observation of a decrease in activation energy is quite large. The authors supposed that the rearrangement of cooperative dynamics at the free surface might be involved in the change in temperature dependence of relaxation time observed for a relatively thick PS thin film (~61 nm); however, more detailed experimental evidence is still needed to verify this idea.

The relaxation time map, which reflects the decrease in activation energy with thickness, and the crossing point are shown in Fig. 27. Utilizing the constructed relaxation time map, the contradictory results observed for the thickness dependence of $T_g$ using two different methods can be explained. Assuming that the ellipsometry measurement detects $T_g$ when relaxation time crosses a certain slow characteristic time (Fig. 27, line A), $T_g$ must decrease with the film thickness. INS detects $T_g$ at a relatively high frequency region compared to other methods and it is assumed that INS detects $T_g$ at a frequency above the crossing point (Fig. 27, line B or line C). Under such conditions, $T_g$ would increase with decreasing film thickness . As a result, both

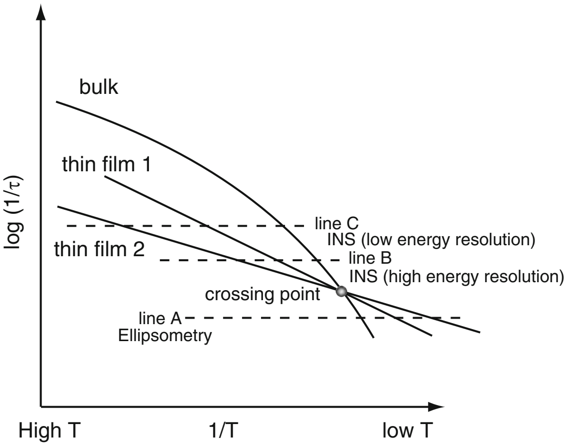

**Fig. 27** Relaxation time map for PS thin films, used to explain the film thickness dependence of $T_g$. Thin film 2 is thinner than thin film 1. See text for full description

INS results and ellipsometry results seem to be explained using the schematic sketch of the relaxation time map. INS measurements with different energy resolutions can serve as a self-check for the relaxation time map, and an increase in $T_g$ would be expected with lowering the energy resolution for same sample. Returning to Fig. 22, it was confirmed that $T_g$ increased with lowering energy resolution; hence, the schematically prepared relaxation time map is consistent with our results.

In order to construct a more reliable relaxation time map quantitatively, complementary use of other methods like dielectric relaxation measurements and INS measurements with different energy resolutions are still needed.

## 6 Distribution of Glass Transition Temperature in Thin Films

In the previous section, it was supposed that the anomalous cooperative dynamics in thin films compared to that of bulk polymer is related to the singular glass transition behavior in thin films. In order to clarify the above idea, it is better to investigate the cooperative dynamics or CRR in thin films directly; however, concrete theoretical and experimental approaches have not been presented up to now. Evaluation of the distribution of $T_g$ in thin films would be a good starting point for accomplishing such a difficult task.

One advantage of neutron scattering is that it can discern hydrogenated and deuterated molecules because of the difference in scattering length density, and this difference can serve as a kind of labeling. In this section, we describe the distribution of $T_g$ in thin films using multilayered PS thin films consisting of deuterated polystyrene (d-PS) and hydrogenated polystyrene (h-PS) using neutron reflectivity.

The obtained neutron reflectivity profiles from d-PS/h-PS/d-PS three-layered thin films at several temperatures are shown in Fig. 28 and the reflectivity profiles were analyzed with the formula derived by Parratt [66]. The solid lines in Fig. 28

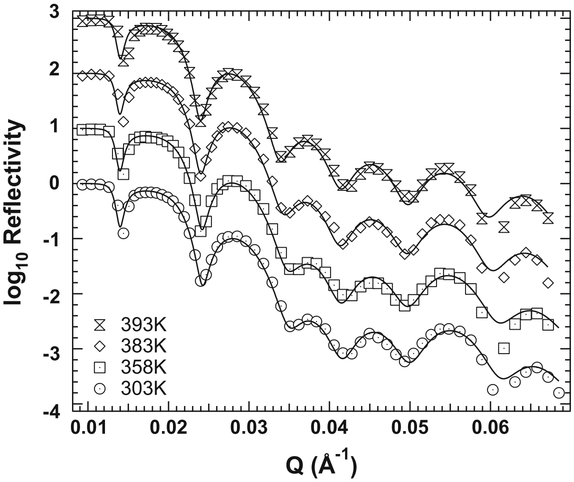

**Fig. 28** Neutron reflectivity profiles from d-PS/h-PS/d-PS three-layered thin films at various temperatures. *Solid lines* correspond to the results of fit with a three-layered model

are the results of fits with the three-layer model. The agreements of fit were very good for the temperatures investigated, indicating that a three-layer model is appropriate for the description of our results at temperatures both above and below bulk $T_g$. The thermal expansivity and $T_g$ of total film thickness was investigated as an initial step, and the temperature dependence of the total film thickness is given in Fig. 29. The evaluated $T_g$ of the total thickness was 374 K and this value was almost the same as the bulk $T_g$ (376 K) within experimental error. Furthermore, the thermal expansivity in the glassy and molten states were $9.4 \times 10^{-5}$ and $4.9 \times 10^{-4}$ K$^{-1}$, respectively, and these values were almost the same as the bulk thermal expansivity ($1.1 \times 10^{-4}$ and $5.1 \times 10^{-4}$ K$^{-1}$). It was found that the total film thickness (~640 Å) exhibited bulk-like behavior and these results were consistent with those of Miyazaki and coworkers [7].

As a next step, the temperature dependence of the three different component layers was studied. The layers were named first layer, second layer, and third layer from the top to bottom, as shown in Fig. 29. Evaluated $T_g$ of the first layer was 358 K, of the second layer 374 K, and was not detectable for the third layer within the experimental temperature range. The evaluated $T_g$ from the first and second layers were consistent with the works by Ellison and Torkelson [29]. As for the interpretation of $T_g$ near the interface between polymer thin film and substrate, the works by Tanaka et al. [67] are quite helpful. They authors observed about 20 K increase in $T_g$ compared with that of bulk at a distance ~200 Å from the substrate for PS thin films supported on $SiO_x$ substrate. The thickness of the bottom layer was ~150 Å; hence, at least a 20 K increase in $T_g$ at the bottom layer would be expected. Considering the zero thermal expansivity of the bottom layer, the $T_g$ of the interfacial layer had a high $T_g$ and possibly shifted out of the experimentally accessible temperature range (above 403 K). Although the total film thickness exhibited a bulk-like behavior, each component layer showed different $T_g$, supporting the idea of dynamic heterogeneity in thin films as well as glassy dynamics.

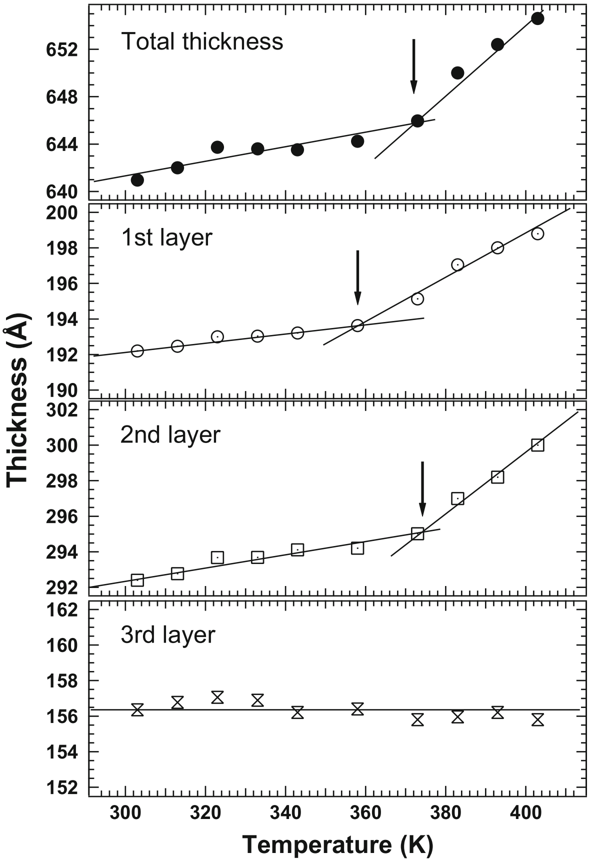

**Fig. 29** Temperature dependence of the total film thickness and thickness of first, second and third layers for a three-layered thin film. The *arrows* indicate the evaluated $T_g$

Utilizing the results from multilayered thin film studies, we would like to understand one aspect of the singular physical properties of “single” PS thin films. Miyazaki et al. [7] reported a decrease in both $T_g$ and thermal expansivity with decreasing PS film thickness using X-ray reflectivity. From the thickness dependence of $T_g$ we get an impression of softening or enhancement of mobility with decreasing film thickness. On the other hand, from the thickness dependence of thermal expansivity we get an impression of hardening or decrease in mobility with decreasing film thickness. Seemingly, the thickness dependence of $T_g$ is inconsistent with a thickness dependence of thermal expansivity despite being measured in the same PS thin films; however, we must try to understand Miyazaki’s results. We have found that polymer thin films consist of a mobile surface layer, middle bulk-like layer, and interfacial layer. We have shown that $T_g$ of the interfacial layer was too high to be detected in the present experimental range. As a result, only the $T_g$ of the surface layer and bulk-like layer in polymer thin films can be detected in the experimental temperature range and the interfacial contribution can be neglected. This is the main reason why the two-layer model works for the description of the thickness dependence of $T_g$ of PS thin films, in spite of the existence of an interfacial layer [7]. That is to say, a decrease in $T_g$ with decreasing film thickness is mainly responsible for the contribution of the surface layer or "surface effect."

How can we interpret the thickness dependence of thermal expansivity? In principle, the thermal expansivity of "total" thin film is given by the average of thermal expansivity of the surface layer, bulk-like layer, and interfacial layer:

$$\alpha = \frac{1}{D} \sum_{i=\mathrm{surf,bl,int}} \alpha_i d_i, \quad D = \sum_{i=\mathrm{surf,bl,int}} d_i, \tag{22}$$

where $\alpha$, $\alpha_{\mathrm{surf}}$, $\alpha_{\mathrm{bl}}$, $\alpha_{\mathrm{int}}$ are the thermal expansivity of total film thickness, surface layer, bulk-like layer and interfacial layer, respectively and $D$, $d_{\mathrm{surf}}$, $d_{\mathrm{bl}}$, $d_{\mathrm{in}}$ are the thickness of total film thickness, surface layer, bulk-like layer, and interfacial layer, respectively. From multilayered thin film studies we could not find a clear change in thermal expansivity of the surface layer ($\alpha_{\mathrm{surf}}$) and bulk-like layer ($\alpha_{\mathrm{bl}}$) compared with that of bulk ($\alpha_{\mathrm{bulk}}$); therefore, it is easily supposed that the surface effect alone is inadequate to understand the thickness dependence of thermal expansivity of polymer thin films. As for the thermal expansivity of the bottom or interfacial layer in a multilayered thin film, we observed zero or quite small thermal expansivity (see third layer in Fig. 29). With decreasing film thickness, the decrease in $\alpha$ might be due to a high contribution from the interfacial layer. Assuming the extreme case that a polymer thin film consists of surface layer and interfacial layer only, then the thermal expansivity would be given by $\alpha_{\mathrm{surf}} d_{\mathrm{surf}}/D$, resulting in the decrease in thermal expansivity with decreasing thickness. The "interfacial effect" is indispensable for the explanation of the thickness dependence of thermal expansivity of PS thin films.

Taking into consideration of both surface effect and interfacial effect we can understand the decrease in thermal expansivity and $T_g$ with decreasing thickness observed simultaneously for the same PS thin film without inconsistency.

Through the multilayer thin film studies we could also clarify that the resulting physical properties of polymer thin films are directly determined by the balance or competition between the surface effect and interfacial effect.

## 7 Concluding Remarks

We have reviewed recent studies on the dynamics of polymer thin films using neutron scattering at temperatures ranging from far below bulk $T_g$ to above bulk $T_g$ and found that heterogeneity is the essential notion for understanding the physical properties of polymer thin films from the perspective of dynamics. If we want to grasp the essence of polymer thin films, we have to aim at investigating the dynamics at a selective position in a thin film (not in entire films), that is to say the distribution of dynamics in a thin film. Such an experimental approach is quite new at present; however, some researchers have started investigations.

Kim et al. studied only the surface region of a polymer thin film by changing the incident angle of X-rays using XPCS [30]. Multilayer methods are also useful and Torkeloson and coworkers used fluorescence to study the aging dynamics (glassy dynamics) of multilayered labeled PMMA thin films [68]. Thanks to the sophistication of neutron source devices, isotope labeling of multilayered thin films might be a reliable method for studying the distribution of dynamics in thin films by INS directly. Is there an alternative method for evaluating heterogeneous dynamics without resorting to labeling or multilayered methods? Pratt et al. [69] studied the dynamics of polymer thin films at different positions in a polymer thin film using slow muons with different incident energies. The advantage of their method is that the dynamics at the desired position in a thin film can be probed just by changing the incident muon energy, which corresponds to changing the interpenetration depth in the thin film. At present, the energy resolution or the width of interpenetration depth is very broad; hence, analyses such as the distribution of relaxation time along the depth direction are not yet practical. However, the refinement of instrumentation would offer better opportunities to study the distribution of dynamics at a given position in polymer thin films.

If we can succeed in evaluating the distribution of dynamics near $T_g$ in thin films qualitatively, we have a chance to evaluate the distribution of CRR in thin films and can discuss the origin of anomalous dynamics in polymer thin films directly. For this purpose, new experimental methods and further theoretical approaches are indispensable.

## References

1. Jones RL, Richards RW (1999) Polymers at surface and interfaces. Cambridge University Press, Cambridge
2. Karim A, Kumar S (eds) (2000) Polymers surfaces, interfaces and thin films. World Scientific, Singapore
3. Keddie JL, Jones RAL, Cory RA (1994) Faraday Discuss 98:219
4. Keddie JL, Jones RAL, Cory RA (1994) Europhys Lett 27:59
5. Kawana S, Jones RAL (2001) Phys Rev E 63:21501
6. Kanaya T, Miyazaki T, Watanabe H, Nishida K, Yamano H, Tasaki S, Bucknall DB (2003) Polymer 44:3769
7. Miyazaki T, Nishida K, Kanaya T (2004) Phys Rev E 69:061803
8. Orts WJ, van Zanten JH, Wu WL, Satija SK (1993) Phys Rev Lett 71:867
9. Fukao K, Miyamoto Y (2000) Phys Rev E 61:1743
10. Tress M, Erber M, Mapresa EU, Huth H, Müller J, Serghei A, Schick C, Eichhorn K-J, Voit B, Kremer F (2010) Macromolecules 43:9937
11. Fryer DS, Nealey PF, de Pablo JJ (2000) Macromolecules 33:6439
12. Efremov MY, Olson EA, Zhang M, Zhang Z, Allen LH (2004) Macromolecules 37:4607
13. Efremov MY, Olson EA, Zhang M, Zhang Z, Allen LH (2003) Phys Rev Lett 91:085703
14. DeMaggio DB, Frieze WE, Gidley DW, Zhu M, Hristov HA, Yee AF (1997) Phys Rev Lett 78:1524
15. Miyazaki T, Nishida K, Kanaya T (2004) Phys Rev E 69:022801
16. Reiter G (1993) Europhys Lett 23:579

17. Reiter G (1994) Macromolecules 27:4607
18. Schmit-Roht K, Spiess HW (1991) Phys Rev Lett 66:3020
19. Cicerone MT, Blackburn FR, Ediger MD (1995) J Chem Phys 102:471
20. Kanaya T, Tsukushi I, Kaji K (1997) Prog Theo Phys Suppl 126:133
21. Buchenau U, Zorn R (1992) Europhys Lett 18:523
22. Sokolov AP, Rossler E, Kisliuk A, Quitmann D (1993) Phys Rev Lett 71:2062
23. Kajiyama T, Tanaka K, Takahara A (1998) Polymer 39:4665
24. Tanaka K, Takahara A, Kajiyama T (2000) Macromolecules 33:7588
25. Forrest JA, Dalnoki-Veress K, Stevens JR, Duchter JR (1996) Phys Rev Lett 77:2002
26. Dalnoki-Veress K, Forrest JA, Murray C, Gigault C, Duchter JR (1996) Phys Rev E 63:31801
27. de Gennes PG (2000) Eur Phys J E 2:201
28. Jones RAL (2000) Eur Phys J E 2:205
29. Ellison CJ, Torkelson JM (2003) Nat Mater 2:695
30. Kim H, Rühm A, Lurio LB, Basu JK, Lal J, Lumma D, Mochrie SGJ, Shinha SK (2003) Phys Rev Lett 90:068302
31. Bée M (1988) Quasielastic neutron scattering, principles and applications in solid state chemistry, biology and materials science. Taylor & Francis, Bristol
32. Imae T, Kanaya T, Furusaka M, Torikai N (eds) (2011) Neutrons in soft matter. Wiley, Hoboken
33. Philips WA (ed) (1981) Amorphous solids – low temperature properties. Springer, Berlin
34. Buchenau U, Nücker N, Dianoux AJ (1984) Phys Rev Lett 53:2316
35. Frick B, Richter D (1993) Phys Rev B 47:795
36. Buchenau U, Schönfeld C, Richter D, Kanaya T, Kaji K, Wehrmann R (1994) Phys Rev Lett 73:2344
37. Fujara F, Petry W (1987) Europhys Lett 4:921
38. Kanaya T, Kawaguchi T, Kaji K (1993) J Chem Phys 98:8262
39. Zorn R (1997) Phys Rev B 61:6249
40. Richter D, Monkenbusch M, Arbe A, Colmenero J (2005) Adv Polym Sci 174:1
41. Brandrup J, Immergut EH, Grulke EA (eds) (1999) Polymer handbook, 4th edn. Wiley, New York
42. Kraus J, Müller-Buschbaum P, Kuhlmann T, Schubert DW, Stamm M (2000) Europhys Lett 49:210
43. Brulet A, Boue F, Menelle A, Cotton JP (2002) Macromolecules 35:8878
44. Marshall W, Lovesey SW (1971) Theory of thermal neutron scattering. Clarendon, Oxford
45. Inoue R, Kanaya T, Nishida K, Tsukushi I, Shibata K (2006) Phys Rev B 74:021801
46. Inoue K, Kanaya T, Ikeda S, Kaji K, Shibata K, Misawa M, Kiyanagi Y (1991) J Chem Phys 95:5333
47. Zhang JM, Zhang DH, Shen DY (2002) Macromolecules 35:5140
48. Gautam KS, Schwab AD, Dhinojwala A, Zhang D, Dougal SM, Yeganeh MS (2000) Phys Rev Lett 85:3854
49. Inamura Y, Arai M, Nakamura T, Otmo T, Kitamura N, Bennington SM, Hanon AC, Buchenau U (2001) J Non-Cryst Solids 293:389
50. Kanaya T, Kaji K (2001) Adv Polym Sci 154:87
51. Nakayama T (1998) Phys Rev Lett 80:1244
52. Das SP (1999) Phys Rev E 59:3870
53. Granato AV (1996) Physica B 220:270
54. Kanaya T, Kawaguchi T, Kaji K (1996) J Chem Phys 104:3841
55. Rahman A, Singwi KS, Sjölander A (1962) Phys Rev 126:986
56. Frick B, Buchenau U, Richter D (1995) Colloid Polym Sci 273:413
57. Arbe A, Colmenero J, Alvarez F, Monkenbusch M, Richter D, Farago B, Frick B (2003) Phys Rev E 67:051802
58. Soles CL, Douglas JF, Wu W, Peng H, Gidley DW (2004) Macromolecules 37:2890
59. Soles CL, Douglas JF, Wu W, Peng H, Gidley DW (2003) Macromolecules 36:373
60. Schönhals A, Goering H, Schick C, Frick B, Mayorova M, Zorn R (2007) Eur Phys J ST 141:255

61. Donth E (1982) J Non-Cryst Solids 53:325
62. Scheidler P, Kob W, Binder K (2000) J Phys IV 10:33
63. Fakhraai Z, Forrest JA (2005) Phys Rev Lett 95:025701
64. Cicerone MT, Blackburn FR, Ediger MD (1995) Macromolecules 28:8224
65. Kanaya T, Tsukushi I, Kaji K, Bartos J, Kristiak J (2000) J Phys IV France 10:Pr7–Pr317
66. Paratt LG (1954) Phys Rev 95:359
67. Tanaka K, Tateishi Y, Okada Y, Nagamura T, Doi M, Morita H (2009) J Phys Chem B 113:4571
68. Priestley RD, Ellison CJ, Broadbelt LJ, Torkelson JM (2005) Science 309:456
69. Pratt FL, Lancater T, Brooks ML, Blundell SJ, Prokscha T, Morenzoni E, Suter A, Luetkens H, Khasanov R, Scheuermann, Zimmermann U, Shinotsuka K, Assender HE (2005) Phys Rev B 72:121401(R)

# Index

**A**
Aging, 29, 53, 69
  dynamics, 65
  isothermal, 75, 97
  physical, 32, 54, 69
Anisotropy, 123–126
Arrhenius equation, 1
Atomic force microscopy (AFM), 39

**B**
Boson peak, 107, 117
Bulk glass-formers, 119, 130

**C**
Chain diffusion, 31, 83
Chain mobility, 9, 114
Coarse-grained molecular dynamics simulation, 1
Coils, 31, 55, 59, 114–116
Constant-rate mode, 75
Cooperatively rearranging region (CRR), 67, 130

**D**
Debye mode, 117
Debye–Waller factor, 119
Dewetting, 29, 108
  Newtonian fluid, 38
  visco-elastic fluid, 43
Dielectric relaxation spectroscopy, 2, 67
Dielectric susceptibility, 101
Differential scanning calorimetry (DSC), 4, 68, 74, 109
Distinct correlation function, 112
Dynamic heterogeneity, 67, 107
Dynamic mechanical analysis (DMA), 21
Dynamic secondary ion mass spectroscopy (DSIMS), 9

**E**
Ellipsometry, 4, 39, 44, 68, 109, 128

**F**
Film preparation, 29
Fluorescence intensity, 16

**G**
Gaussian polymer coils, 31
Glass–rubber transition, 7
Glass transition, 5, 29, 65, 66
Glass transition temperature ($T$g), 1ff
  distribution, 134
  thickness dependence, 108

**H**
Havriliak–Negami (HN) equation, 86
Heterogeneous dynamics, 65, 110, 128

**I**
Inelastic neutron scattering, 107, 108
Interchain overlap, 31
Interfaces, 1ff
  interaction, 65

**K**

Kohlrausch–Williams–Watts equation (KWW), 86

**L**

Lateral force microscopy (LFM), 5
Low energy excitation, 113
Lubrication approximation, 34

**M**

Mean square displacement, 116
Memory effect, 65, 70
Mobility gradient, substrate interface, 17
  surface, 9
Modulus mapping, two-dimensional, 4
Molecular dynamics simulation, 11

**N**

Nanosecond, 128
Neutron scattering, 111, 128
Neutron spin echo (NSE), 128
6-[*N*-(7-Nitrobenz-2-oxa-1,3-diazol-4-yl) amino]hexanoic acid (NBD), 15
No-slip, dewetting 33
Nuclear magnetic resonance (NMR), 108

**P**

Photo probe, 108
Physical aging, 32, 54, 69
Picosecond, 113
Poly(2-chlorostyrene) (P2CS), 65, 69, 73, 76
Polydimethylsiloxane (PDMS), 38
Polymer diffusion, 31
Polymer glasses, aging, 69
Poly(methyl methacrylate) (PMMA), 69, 91, 109
Poly(methyl phenyl siloxane) (PMPS), 129
Polystyrene (PS) films, 1, 68
  deuterated (dPS), 9, 134
  hydrogenated (hPS), 10, 134
  monodisperse, 1, 6
Positron annihilation lifetime spectroscopy (PALS), 129
Probing, 29

**Q**

Quasielastic neutron scattering, 110

**R**

Radius of gyration, 10, 20, 31, 56, 114
Rejuvenation effects, 65, 72
Relaxation times, 24, 29
  map, 133
Residual stress, 29
Retraction, 32
Rim formation, 34
Roughening, 31

**S**

Scanning force microscopy (SFM), 1
Scanning probe microscopy (SPM), 109
Scanning viscoelasticity microscopy (SVM), 4
Silicon oxide, 1
Sliding, 101
Slippage, 33, 38, 41
Small angle neutron scattering (SANS), 114
Space-and time-resolved fluorescence spectroscopy, 19
Spatial confinement, 132
Specular X-ray reflectivity (SXR), 129
Spin-coating, 31
Substrate interface, glass transition, 15
  mobility gradient, 17
  molecular dynamics simulation, 19
Sum-frequency (SFG) spectroscopy, 118
Supercooled liquid state, 66
Surface effect, 3, 137
Surface mobile layer molecular weight dependence, 11
Surfaces, 1
  mobility gradient, 9
  scratched, 5

**T**

Thermal expansivity, 108, 135–137
Thermal molecular motion, 1
Thickness dependence, 108
Thin films, 1ff
  aging dynamics, 5
  glass transition, 67
    temperature, 134
  sandwiched, 23
  stacked, 65, 72, 74, 77
  supported, 21
Time-and space-resolved fluorescence spectroscopy, 1
Time–temperature superposition, 6

**U**
Ultrathin films, 2, 21, 65, 72, 89
  aging dynamics, 90

**V**
Van Hove correlation functions, 112
Vogel–Fulcher–Tamman equation, 1, 65, 67, 129
Vogel temperature, 24, 67, 87

**X**
X-ray photon correlation spectroscopy (XPCS), 110